Oil & Natural Gas Technology

Phase 2 Report
Type: Other
(Period ending 1/14/2016)

CONTROLS ON METHANE EXPULSION DURING MELTING OF NATURAL GAS HYDRATE SYSTEMS: TOPIC AREA 2
Project Period (10/1/2012 to 1/14/2016)

Submitted by:
Peter B. Flemings
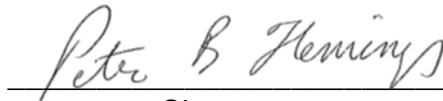
_____
Signature

The University of Texas at Austin
101 East 27th Street, Suite 4.300
Austin, TX 78712-1500
e-mail: pflemings@jsg.utexas.edu
Phone number: 512-475-9520

Office of Fossil Energy

1

CONTROLS ON METHANE EXPULSION DURING MELTING OF NATURAL GAS HYDRATE SYSTEMS: TOPIC AREA 2
PHASE 2 REPORT

Contents

1. Executive Summary

1.1. Project Goal

The project goal is to predict, given characteristic climate-induced temperature change scenarios, the conditions under which gas will be expelled from existing accumulations of gas hydrate into the shallow ocean or directly to the atmosphere. When those conditions are met, the fraction of the gas accumulation that escapes and the rate of escape shall be quantified. The predictions shall be applicable in Arctic regions and in gas hydrate systems at the up dip limit of the stability zone on continental margins. The behavior shall be explored in response to two warming scenarios: longer term change due to sea level rise (e.g. 20 thousand years) and shorter term due to atmospheric warming by anthropogenic forcing (decadal time scale).

1.2. Project Objectives

During the first budget period, the objectives are to review and categorize the stability state of existing well-studied hydrate reservoirs, develop conceptual and numerical models of the melting process, and to design and conduct laboratory experiments that dissociate methane hydrate in a model sediment column by systematically controlling the temperature profile along the column. The final objective of the first budget period shall be to validate the models against the experiments.

In the second budget period, the objectives are to develop a model of gas flow into sediment in which hydrate is thermodynamically stable, and conduct laboratory experiments of this process to validate the model. The developed models shall be used to quantify the rate and volume of gas that escapes from dissociating hydrate accumulations. In addition, specific scaled simulations characteristic of Arctic regions and regions near the stability limit at continental margins shall be performed.

1.3. Project Background and Rationale

The central hypothesis proposed is that hydrate melting (dissociation) due to climate change generates free gas that can, under certain conditions, propagate through the gas hydrate stability zone and vent at the seafloor. Gas venting through the regional hydrate stability zone is accomplished by alteration of the regional equilibrium conditions (creation of three phase conditions) by increased salinity and heat due to hydrate formation, due to gas fracturing, or a combination of both. This research will explore the controls on whether methane reaches the seafloor (or atmosphere) as the original hydrate deposit dissociates and what the magnitude of these fluxes are. This hypothesis has significant implications for the forcings and feedbacks associated with climate change. It is described below the observations and models that have led to formulating this hypothesis.

2. Summary of Phase 2 Research

2.1. Task 1: Project Management and Planning

A. Goal:

The Recipient shall execute the project in accordance with the approved Project Management Plan covering the entire project period. The Recipient shall manage and control project activities in accordance with their established processes and procedures to ensure subtasks and tasks are completed within schedule and budget constraints defined by the Project Management Plan. This includes tracking and reporting progress and project risks to DOE and other stakeholders.

B. Activities Phase 2:

1. Coordinated the overall scientific progress, administration and finances of the project
2. Communicated with project team and sponsors
    a. Organized regular team meetings
    b. Actively monitored project risks and as needed reported to project team and stakeholders.
    c. Managed SharePoint site to facilitate online communication and collaboration
    d. Managed email list serves for key project teams
    e. Completed Reports:
        i. Quarterly Research Performance Progress Reports
        ii. Monthly Cost Accrual Reports
        iii. Monthly SF-425 Federal Financial Reports

2.2. Task 5: Gas Expulsion Modeling (Complete)
Milestone 2.A 1-D simulation of gas expulsion into hydrate stability zone.

Milestone 2.B Determination of conditions for which gas expulsion into hydrate-stability zone is self-limiting.

A. Goal:

The Recipient shall use the validated model of dynamics within a dissociating hydrate from Task 2 to drive a model of the transport of gas expelled upward from the hydrate‐bearing sediment. The Recipient shall focus on a situation which is inevitable in several combinations of initial and boundary conditions: the gas rises into water‐saturated sediment which is in the hydrate stability zone. The effect of latent heat of formation and of salinity shall be included in this model. The Recipient shall validate the models against laboratory experiments on methane migration at three phase stability, hydrate formation and hydrate dissociation.

The Recipient shall explore both the role of capillarity and the role of sediment fracturing in driving this migration. For example, under certain conditions the gas pressure shall exceed the least principle stress in the rock matrix and the flow will be driven along fractures. The Recipient shall explore the role of

both these processes with a goal to bring all these considerations to bear on the question of gas migration during hydrate dissociation and gas migration.

B. Activities Phase 2:

B1. Subtask 5.1: Develop 1D model of gas expulsion into water-saturated hydrate-stability zone (Complete)

B1.1. Goal:

Based on results from Task 3.0, it is expected that under certain scenarios, gas pressures will elevate sufficiently enough to result in overcoming the capillary barrier of the overburden or to overcome the least principal stress and migrate by fractures. Therefore, the Recipient shall extend existing models of hydrate formation and gas propagation to account for the coupling between heat transport, salinity transport and gas phase pressure and shall include a mechanism to describe whether flow is through the matrix or via fractures. The extended model shall be applied to determine the conditions for which the gas expulsion is self-limiting, i.e. when growth of hydrate effectively creates a seal in the overlying sediment. The Recipient shall compute the conditions for which self-limiting gas expulsion is permanent, i.e. the temperature perturbation is insufficient to move the gas contained in the original accumulation all the way to seafloor or land surface. For other conditions, the delay in arrival of methane at the seafloor/atmosphere for conditions shall be computed.

B1.2. Activities Phase 2:

B.1.2.1 1D Numerical Expulsion Model

We have fully developed a 1D numerical model. We add a new phase, ice, into the model, which allows us to simulate the permafrost associated hydrate dynamics. To include the ice phase, we have to introduce a new model for the hydrate phase boundary, which is described as below.

The phase boundary for methane hydrate depends on water pressure (P_w), temperature (T) and salinity (X_l^s).In salt-free systems (Figure 1), it is described as (Moridis, 2008)

$$\ln(P_w) = a_1 + a_2 T + a_3 T^2 + a_4 T^3 + a_5 T^4 + a_6 T^5,$$
Eq 1

when temperature is greater than pure water freezing temperature (273.2 K or 0 °C). a_1, a_2, a_3, a_4, a_5 and a_6 are constants listed in Table 1. On this phase boundary, methane hydrate coexists with liquid water and methane gas (Figure 1). When temperature is lower than water freezing temperature, it is described as (Moridis, 2008)

$$\ln(P_w) = b_1 + b_2 T + b_3 T^2 + b_4 T^3 + b_5 T^4 + b_6 T^5.$$
Eq 2

b_1, b_2, b_3, b_4, b_5 and b_6 are constants listed in Table 1. On this phase boundary, methane hydrate coexists with ice and methane gas (Figure 1).

The phase boundary for water and ice depends on salinity (X^s_l) and temperature (*T*). The pressure effect is negligible under typical hydrate conditions (Sloan and Koh, 2007; Sun and Mohanty, 2006). In salt-free systems, the water freezing temperature or ice melting temperature is 273.2 K or 0 °C. Salinity shifts this

phase boundary toward lower temperature (Figure 2). The water freezing temperature (T_w) in presence of sodium chloride (NaCl) is obtained from Lide (2004) as (Sun and Mohanty, 2006)

$$T_w = T_{w0} - X_l^s \left(164.49 X_l^s + 49.462\right),$$

Eq 3

T_{w0} is the pure water freezing temperature (273.2 K or 0 °C). X_l^s is the mass fraction of NaCl in liquid water phase. Eq. (3) is valid in the salinity range of 0 and 0.22 (mass fraction) (Sun and Mohanty, 2006).

Salinity also shifts the phase boundary of methane hydrate toward lower temperature (Figure 2). The depression of the hydration temperature (ΔT_h, °C) in presence of salt is described as (Sloan and Koh, 2007; Sun and Mohanty, 2006)

$$\frac{\Delta T_h}{T_{h0}\left(T_{h0} - \Delta T_h\right)} = 0.6723 \frac{\Delta T_w}{T_{w0}\left(T_{w0} - \Delta T_w\right)},$$

Eq 4

where T_{h0} is the hydration temperature in salt-free systems (°C) described in Eqs. (5) and (6). ΔT_w is the depression of water freezing temperature (°C) in presence of sodium chloride (NaCl), and (Sun and Mohanty, 2006)

$$\Delta T_w = X_l^s \left(164.49 X_l^s + 49.462\right).$$

Eq 5

In this model, we consider 11 equilibrium thermodynamic status in total (Table 2). If the sediment is initially filled with brine, the system thermodynamic status can never go to the left side of the ice-water phase boundary (dashed lines in Figures 1 and 2). It is a reasonable assumption for typical permafrost and methane hydrate system, because solubility of NaCl is about 22 wt.% (Sun and Mohanty, 2006), which can shift the water freezing point to as low as -18.8 °C. If the sediment is initially filled with pure water or ice, the system can shift among the 11 thermodynamic status listed in Table 2 (Figure 1). Four independent primary variables are required for this three-component system (Liu and Flemings, 2007). Primary viables are switched according to the different thermodynamic status (Table 2).

Our work has led us to explore two additional models arguments: 1) An analytical approach to the 1D modeling and 2) A numerical approach to look at hydrate in fractures.
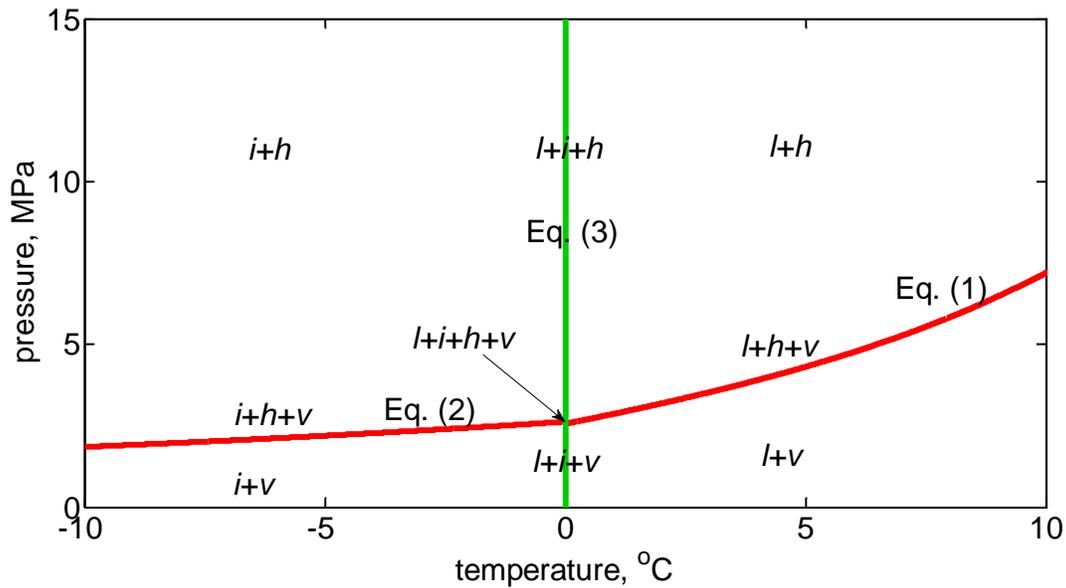
Figure 1: The pressure-temperature phase diagram of methane hydrate for salt-free systems. The red line is the phase boundary for methane hydrate and methane gas phases. The green line is the phase boundary for ice and liquid water phases. Three phases coexist on these phase boundaries. At the quadruple point, liquid water, ice, hydrate and gas phases coexist. h, i, l and v means hydrate, ice, liquid water and gas phases, respectively.
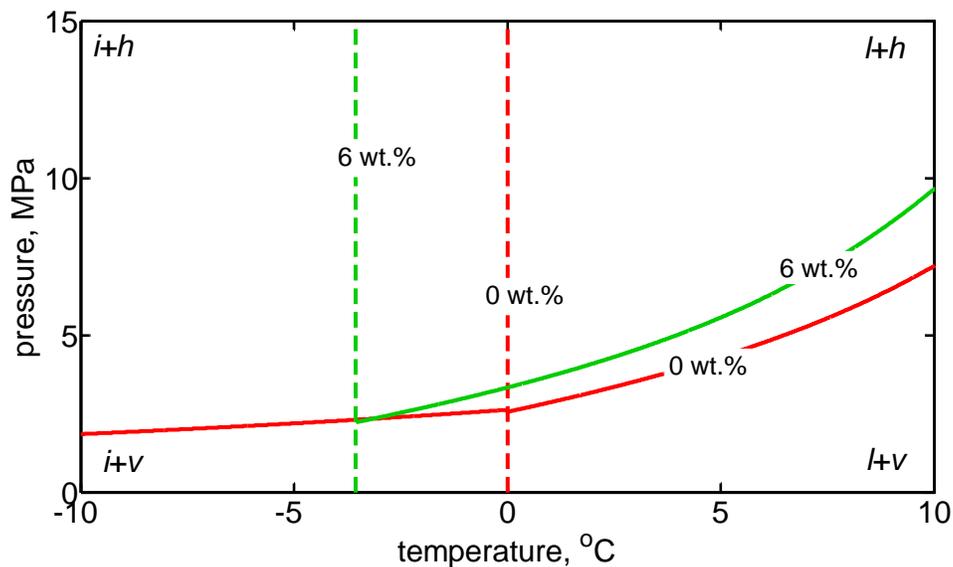

Figure 2: Shifts of phase boundaries with salinity. The solid lines are the phase boundaries for methane hydrate and methane gas phases. The dashed lines are the phase boundaries for ice and liquid water phases. The ice-hydrate-gas curve does not change with salinity.

Table 1: Constants used in Eqs. (1) and (2) [Moridis et al., 2008].

Constants	Values
a_1	-1.94138504464560e5
a_2	3.31018213397926e3
a_3	-2.25540264493806e1
a_4	7.67559117787059e-2
a_5	-1.30465829788791e-4
a_6	8.86065316687571e-8
b_1	-4.38921173434628e
b_2	7.76302133739303e-1
b_3	-7.27291427030502e-3
b_4	3.85413985900724e-5
b_5	-1.03669656828834e-7
b_6	1.09882180475307e-10

Table 2: Phase states, corresponding primary variables and additional constrains.

Phase state	Phase present	Primary variables	Supplementary constrains
1	l	$P_w,\ X_l^s,\ X_l^m, T$	$S_l=1,\ S_i=S_v=S_h=0$
2	$l+v$	$P_w,\ X_l^s, S_l, T$	$S_v=1-S_l, S_i=S_h=0,\ X_l^m=X_{l+v}^m$
3	$l+h$	$P_w,\ X_l^s, S_l, T$	$S_h=1-S_l, S_i=S_v=0,\ X_l^m=X_{l+h}^m$
4	$i+v$	$P_w,\ X_l^s, S_i, T$	$S_v=1-S_i, S_l=S_h=0,\ X_l^m=0$
5	$i+h$	$P_w,\ X_l^s, S_i, T$	$S_h=1-S_i, S_l=S_v=0,\ X_l^m=0$
6	$l+i$	$P_w,\ X_l^m, S_l, T$	$S_i=1-S_l, S_h=S_v=0,\ X_l^s=X_{l+i}^s$
7	$l+h+v$	P_w, S_h, S_l, T	$S_v=1-S_l-S_h, S_i=0,\ X_l^m=X_{l+h+v}^m,\ X_l^s=X_{l+h+v}^s$
8	$i+h+v$	P_w, S_h, S_i, T	$S_v=1-S_i-S_h, S_l=0,\ X_l^m=0,\ X_l^s=0$
9	$l+i+h$	P_w, S_h, S_l, T	$S_i=1-S_l-S_h, S_v=0,\ X_l^m=X_{l+h}^m,\ X_l^s=X_{l+i}^s$
10	$l+i+v$	P_w, S_i, S_l, T	$S_v=1-S_l-S_i, S_h=0,\ X_l^m=X_{l+v}^m,\ X_l^s=X_{l+i}^s$

| 11 | $l + i + h + v$ | S_i, S_h, S_l, T | $S_v = 1 - S_l - S_i - S_h$, $X_l^m = X_{l+v+h}^m$, $X_l^s = X_{l+i}^s$, $P_w = P_e$ |

Note: in Table 2, $X_{\sum \beta}^{\kappa}$ is the mass fraction (or solubility) of component κ in liquid phase when phases $\sum \beta$ are in equilibrium (dimensionless). P_e is the quadruple point pressure (Pa).

B.1.2.2 1D Analytical Methods of Characteristics Expulsion Model

B.1.2.2a Mathematical models

We develop an analytical model using method of characteristics to describe the one-dimensional hydrate system development in this section. Figure 3 is a schematic diagram of the model. The sediment is initially fully saturated with brine of salinity cl_0. The sediment has a uniform temperature T_0 and a small pressure gradient with an average pressure of P_0. The initial system is in hydrate stability zone.

Methane gas is injected with a fixed rate of q_{gi} and density of ρ_{gi} from the left end. Methane hydrate forms from the gas inlet and increases the local salinity to three-phase equilibrium value, when no more hydrate can form. Hydrate solidification front and gas front moves further into the sediment (rightward). We neglect the hydrate formation kinetics because hydrate formation is rapid as shown by laboratory (Zatsepina and Buffett, 2003) and field (Rehder et al., 2002) studies. Therefore, gas saturation is zero at the downstream side of the hydrate solidification front (point *a* in Figure 3). It increases gradually from the hydrate solidification front to the gas inlet (Figure 3). We also neglect the diffusion transport.

This semi-infinite system contains three phases (subscript κ), gas (g), liquid water (l) and hydrate (h) phases, and three components (subscript β), brine with the three-phase equilibrium salinity (*B*), pure water (*W*) and methane (*M*).

The mass conservation equation for methane is

$$\frac{\partial G_M}{\partial \tau} + \frac{\partial H_M}{\partial \varepsilon} = 0 , \qquad\qquad \text{Eq 6}$$

where τ is the dimensionless time; ε is the dimensionless distance from the gas inlet; G_M is the dimensionless overall concentration of methane; and H_M is the dimensionless overall flux of methane. These parameters are defined as

$$\tau = \frac{q_{gi}t}{L\phi},$$

Eq 7

$$\varepsilon = \frac{x}{L},$$

Eq 8

$$G_M = X_{M,l}\rho_{lD}S_l + X_{M,g}\rho_{gD}S_g + X_{M,h}\rho_{hD}S_h,$$

Eq 9

$$H_M = v_D\left(X_{M,l}\rho_{lD}f_l + X_{M,g}\rho_{gD}f_g\right),$$

Eq 10

where t is time (sec); L is characteristic length (m); ϕ is porosity of the sediment (m³ m⁻³); $X_{M,l}$, $X_{M,g}$ and $X_{M,h}$ are the mass fraction of methane (dimensionless) in liquid water, gas and hydrate phases, respectively; ρ_{lD}, ρ_{gD} and ρ_{hD} are the dimensionless density of liquid water, gas and hydrate phases, respectively, and $\rho_{lD} = \frac{\rho_l}{\rho_{gi}}$, $\rho_{gD} = \frac{\rho_g}{\rho_{gi}}$, $\rho_{hD} = \frac{\rho_h}{\rho_{gi}}$; ρ_l, ρ_g and ρ_h are the density of liquid water, gas and hydrate phases (kg m⁻³), respectively; S_l, S_g and S_h are the saturation of liquid water, gas and hydrate phases (dimensionless), respectively; v_D is the dimensionless total flux, and $v_D = v/q_{gi}$; v is the total flux (m sec⁻¹) of the mobile phases; f_l and f_g are the fractional flow of liquid water and gas phases (dimensionless), respectively.

$$f_g = \frac{\lambda_g}{\lambda_g + \lambda_l}\left[1 + \frac{k\lambda_l}{v}\left(\frac{\partial P_c}{\partial x} + (\rho_l - \rho_g)g\sin\theta\right)\right],$$

Eq 11

$$f_l = 1 - f_g,$$

Eq 12

where λ_l and λ_g are the mobility (Pa⁻¹ sec⁻¹) of gas and liquid water phases, respectively, and $\lambda_g = k_{rg}/\mu_g$, $\lambda_l = k_{rl}/\mu_l$; k_{rg} and k_{rl} are the gas and liquid water phase relative permeabilities (dimensionless), respectively; μ_g and μ_l are the gas and water dynamic viscosities (Pa sec), respectively; k is the intrinsic permeability of the sediment (m²); g is the gravitational acceleration (m sec⁻²); θ is the dip angle measured as the angle between the flow direction and a horizontal line (rad); P_c is the capillary pressure between the gas and liquid water phases (Pa). f_g can be broken into three components: a viscous component ($\frac{\lambda_g}{\lambda_g + \lambda_l}$), a capillary component ($\frac{\lambda_g}{\lambda_g + \lambda_l}\frac{k\lambda_l}{v}\frac{\partial P_c}{\partial S_g}\frac{\partial S_g}{\partial x}$) and a gravity component ($\frac{\lambda_g}{\lambda_g + \lambda_l}\frac{k\lambda_l}{v}(\rho_l - \rho_g)g\sin\theta$) (DiCarlo et al., 2012).

According to method of characteristics (Orr, 2007), the overall concentration of methane G_M does not change with time on the characteristic curve

$$\xi = \frac{\partial H_M}{\partial G_M} \tau + \varepsilon_0 \,,$$

Eq 13

where ε_0 is the initial dimensionless position of the composition G_M. The same procedure can be applied to the component of pure water and brine with three-phase equilibrium salinity.

A leading shock develops at the hydrate solidification front where the system changes from three phases to one phase (Orr, 2007) (Figure 3). The shock wave velocity equals the composition wave velocity at b in Figure 3. Each component must have the same shock wave velocity. Therefore,

$$\Lambda_B^{ab} = \Lambda_W^{ab} \,,$$

Eq 14

$$\Lambda_B^{ab} = \Lambda_M^{ab} \,,$$

Eq 15

$$\Lambda_B^{ab} = \frac{\partial H_\beta}{\partial G_\beta}\Big|_b = v_D^b \frac{\partial f_g}{\partial S_g}\Big|_{S_g = S_g^b} \,,$$

Eq 16

where the superscripts a and b means the downstream and upstream side of the leading shock, respectively; Λ_β^{ab} is the dimensionless leading shock velocity calculated by the component β. It is also the dimensionless hydrate solidification front advancing velocity and is expressed as

$$\Lambda_\beta^{ab} = \frac{H_\beta^a - H_\beta^b}{G_\beta^a - G_\beta^b}, \quad \beta = B, W, M \,.$$

Eq 17

If both the gravity and capillary components of the gas fractional flow f_g is neglected, we can obtain the hydrate (S_h), liquid water (S_l) and gas phase saturations (S_g) at b and the ratio of the flux between a and b (v_D^a / v_D^b) by solving the nonlinear equation group of Eqs. (6), (7) and (9)-(12). The trailing shock calculation provides the saturations at point c in Figure 3.

The total liquid water and gas phase flux between c and b is uniform and equals that at c or b because it is in the three-phase region and the phase compositions are fixed (Orr, 2007). Therefore, composition wave velocity between c and b can be calculated as (Orr, 2007)

$$\Lambda^e = v_D^c \frac{\partial f_g}{\partial S_g}\Big|_{S_g = S_g^e} \,,$$

Eq 18

where S_g^e is an arbitrary gas saturation between c and b or between S_g^c and S_g^b; Λ^e is the dimensionless composition wave velocity for gas saturation of S_g^e. At the dimensionless time τ, the dimensionless distance between the place where gas saturation equals S_g^e and the gas inlet ξ^e is calculated as

$$\xi^e = \Lambda^e \tau .$$
<div align="right">Eq 19</div>

Hydrate saturation is homogeneous from c to b ($S_g^c = S_g^b$). That is because the system initial condition is nearly homogeneous and we neglect the salt diffusion. Hydrate and liquid water phase saturation at ξ^e (S_l^e) are

$$S_h^e = S_h^b ,$$
<div align="right">Eq 20</div>

$$S_l^e = 1 - S_g^e - S_h^e .$$
<div align="right">Eq 21</div>

B.1.2.2b Example calculations

Figure 4 shows the characteristics of an example calculation with the parameters listed in Table 1. The saturations of each phase does not change along the characteristics (Figure 4). The characteristics for the initial composition (100% liquid water) emanate from $\tau = 0$ and have the slope of 5.9 (red lines in Figure 4). The characteristics for the injection composition (100% gas) emanates from $\tau = 0$ and along the $\xi = 0$ line (Figure 4). There is a trailing shock from the injection composition to the gas saturation of 28.5%, but it has zero wave velocity. Therefore, the fan of characteristics for the discontinuity initially present at the gas inlet extends all the way from the gas saturation of 10.7% to $\xi = 0$. Leading shock happens where the characteristic of gas saturation 10.7% intersects the initial composition (red lines in Figure 4). Any line in the characteristics figure that is parallel to the line of $\tau = 0$ provides the saturation distribution along the column at a certain time. Any line that is parallel to the line of $\xi = 0$ provides the system composition evolution with time at a certain distance from the gas inlet (Figure 5).

The hydrate solidification front advancing velocity or the leading shock wave velocity is 0.63 cm hour^{-1}. The hydrate saturation is 68.4% behind the hydrate solidification front (Figure 5). The gas saturation continuously decreases from 28.5% (point c) to 10.7% (point b), and water saturation continuously increases from 3.1% (point c) to 20.9% (point b) (Figure 5). Hydrate formation at the hydrate solidification front causes total volume loss and decreases the total flux from 10^{-6} m sec^{-1} (point b, c and d) to 1.71×10^{-7} m sec^{-1} (point a).

B.1.2.2c Comparison with numerical models

Liu and Flemings (2007) developed a fully coupled multiphase multicomponent fluid flow and mass transport numerical model to simulate the methane hydrate formation and dissociation dynamics. We did two simulations to investigate the hydrate system development using this model with the same parameters listed in Table 1. The first one considers the capillary pressure (dashed lines in Figure 5), and the second one neglects the capillary pressure (dotted lines in Figure 5). Compared with these two numerical simulations, the hydrate saturation calculated by the analytical solution are lower while the gas saturation are higher (Figure 5). Hydrate solidification front calculated by the analytical solution moves a little faster than the numerical simulations (Figure 5). The analytical solution matches much better with the numerical simulation neglecting the capillary pressure effect (solid lines are more close to the dotted lines than to the dashed lines), because we did not include the capillary component in the fractional flow curve in this analytical simulation. The difference between the analytical and numerical results neglecting the capillary pressure close to the gas inlet is caused by the boundary effect in the numerical simulation. Their difference at the leading shock is caused by the fact that the numerical solution inevitably has numerical diffusion causing smearing of shocks.

B.1.2.2d Gravity effects

In the above discussions, we only consider viscous component of the fractional flow. The viscous component describes the gas flow induced by the gradient of water pressure deviation from the hydrostatic pressure (overpressure gradient). The gravity component describes the gas flow induced by the density difference between the gas and liquid phases (buoyancy). As gravity component is also included, we define the ratio of the vertically upward gas flow under buoyancy to that under overpressure gradient in absence of hydrate as gravity number (R_g , dimensionless) (Lake, 1989)

$$R_g = \frac{k_0 k_{rl}^*}{q_{tot} \mu_l} (\rho_l - \rho_g) g \, ,$$
Eq 22

where k_{rl}^* is the relative liquid permeability when the effective gas saturation reaches the residual value (S_{gr}).

Overpressure gradient dominates gas flow when gravity number R_g is much less than one:

$$R_g = \frac{k_0 k_{rl}^*}{v \mu_l} (\rho_l - \rho_g) g \ll 1 \, .$$
Eq 23

This case is the similar with and the solution construction is the same with the case presented above where only the viscous component of the gas flow is included.

Buoyancy dominates upward gas flow when R_g is much greater than one:

$$R_g = \frac{k_0 k_{rl}^*}{q_{tot} \mu_l} (\rho_l - \rho_g) g \gg 1 \, .$$
Eq 24

The leading shock is no longer a semi-shock (Orr, 2007), as the semi-shock condition would lead to a landing point with a gas fractional flow greater than unity. Instead, the shock is directly to a gas fractional flow of unity. The hydrate saturation from point 'b' to 'c', the gas and liquid saturation at point 'b', and the ratio of the total flux between point 'a' and 'b' are obtained by solving the nonlinear equations ((9), (10), (12) and (20) (DiCarlo et al., 2012).

$$f_g \left(S_{gf}, S_h \right) = 1, \, k_{rw} \neq 0 \, .$$
Eq 25

There is no longer a rare-faction between point 'b' and 'c'. Hydrate, gas and liquid saturations are all constant behind the shock. The gas volumetric flux is constant and equals gas injection rate, and the liquid volumetric flux is zero from point 'b' to 'c'. The water pressure equals the hydrostatic water pressure, overpressure equals zero, and gas migration is driven solely by buoyancy (England et al., 1987; Hubbert, 1953).

The dimensionless and dimensional advancing velocity of hydrate solidification front is calculated by Eq. (21a) and (21b), respectively.

$$v_{reaction}^{D} = \frac{H_{\beta}^{b} - H_{\beta}^{a}}{G_{\beta}^{b} - G_{\beta}^{a}}, \quad \beta = B, W, M \,,$$
<div align="right">Eq 26</div>

$$v_{reaction} = \frac{q_{gi}}{\phi} \frac{H_{\beta}^{b} - H_{\beta}^{a}}{G_{\beta}^{b} - G_{\beta}^{a}}, \quad \beta = B, W, M \,.$$
<div align="right">Eq 27</div>

Buoyancy dominates downward gas flow when Eq. (19) is true. The gas fractional flow f_g versus the saturation for downward flow decreases with gas saturation from zero, reaches a trough value less than zero, and then increases with gas saturation and gradually converges to one at high gas saturation. The solution is similar with and the solution construction is the same as the case when overpressure gradient dominates the gas flow. The only difference is that the fractional flow curve goes negative for certain saturations – these saturations are not observed in the solution because of the discontinuous changes in saturations at the shock.

For this discussion, we will concentrate on the results for a flow velocity of 10^{-9} m^3 m^{-2} s^{-1}, combined with the other parameters listed in Table 1 results in a gravity number of R_g=464. We begin the discussion with the gas saturation behind the hydrate solidification front. Gas saturations are quite different for horizontal, downward, and upward flows (Figure 6a). Gas saturation continuously decreases from the gas inlet to the hydrate solidification front for horizontal and downward flow, whereas gas saturation is homogeneous behind the hydrate solidification front for upward flow (Figure 6a). Gas saturation is over 42.9% for downward flow at this rate, is over 10.7% for horizontal flow, and is at 2.6%, close to the residual value for upward flow ($S_{gr} = 2.0\%$).

These differences are caused by the effect of gravity and can be understood as follows. According to Darcy's law of gas volumetric flux, the gravity or the buoyancy contributes to upward flow, is zero for horizontal flow, and inhibits downward flow. Therefore, for the same overpressure gradients, the magnitude of the impelling force (overpressure gradient plus buoyancy) for a gas element is smallest for the downward flow, and largest for the upward flow. The gas relative permeability adjusts itself to allow flow at the rate it is supplied, and gas permeability depends monotonically on the gas saturation. Thus the gas saturation is higher for downward flow in order to overcome gas buoyancy (lower driving force), and it is lower in upward flow where buoyancy works with the flow. These differences disappear at high gas supply rates, when the overpressure gradients dominate the flow.

In contrast to the gas saturation, the liquid saturation behind the front is highest for upward flow and lowest for downward flow (Figure 6b). It is over 20% for upward flow, and less than 15% for the downward flow (Figure 6b). These differences are caused by the gas saturation differences at the hydrate solidification front. When there is a low gas saturation behind the front, as seen for upward flow, there is necessarily more water behind the front. When there is a high gas saturation behind the front, as seen in downward flow, there is necessarily less water behind the front. In all cases, the water behind the front is converted to hydrate until the remaining water reaches the three-phase salinity. More water initially left behind the front results in a higher liquid saturation after hydrate formation (upward flow).

In addition, more water initially left behind the front means more fresh water available to form hydrate. Since gas is being continuously supplied, the limiting factor for hydrate formation is the amount of fresh water available. Simply, more water initially left behind the front results in a higher hydrate saturation. Therefore, the hydrate saturation follows the liquid saturation. It is highest for upward flow and lowest

for downward flow. It is 76.7% for upward flow, 68.4% for horizontal flow, and 43.4% for downward flow (Figure 6c).

In all these cases gas is supplied at the same rates, but the velocities of the fronts change with these changes in saturations due to the volume change on mixing. Because the density of methane in the hydrate phase is much greater than in the gas phase for the parameters listed in Table 1, flow with the highest hydrate saturation (upward) yields the lowest front velocity, and the lowest hydrate saturation (downward) yields the highest front velocity. In addition to changing the front velocity, the different hydrate saturations also change the exiting volumetric flux. Higher hydrate saturations consume more methane with the result being the exiting volumetric flux is highest for downward flow and lowest for upward flow (Figure 6d).

In addition to the flow direction, the saturations depend on the flow rate. We will focus the discussion on hydrate saturation here. For horizontal flow, hydrate saturation is independent on the gas injection rate (Figure 7: the red line is flat). That is because there is no gravity or buoyancy, and the impelling force only includes the overpressure gradient. Overpressure gradient increases with the flow rate, and a same gas or hydrate saturation can be obtained for different flow rates.

For upward flow, hydrate saturation increases with decreasing gas injection rate when it is between 10^{-11} and 10^{-6} m^3 m^{-2} s^{-1} (Figure 7: green line). Buoyancy decreases the gas saturation and increases the hydrate saturation for upward flow. The relative importance of buoyancy increases as the overpressure gradient decreases with the flow rate, which results in a higher hydrate saturation at a lower flow rate. The hydrate saturation versus gas injection rate flattens out at very low (<10^{-11} m^3 m^{-2} s^{-1}) gas injection rate, where buoyancy dominates the flow, and gas saturation is very close to the residual value. It also flattens out at very high (>10^{-6} m^3 m^{-2} s^{-1}) gas injection rates, where the overpressure gradient dominates the upward flow.

For downward flow, hydrate saturation decreases with the gas injection rate when it is less than 10^{-6} m^3 m^{-2} s^{-1} (Figure 7: blue line). Buoyancy increases the gas saturation and decreases the hydrate saturation for upward flow. Therefore, a lower flow rate results in a lower hydrate saturation. The hydrate saturation versus gas injection rate flattens out at very high (>10^{-6} m^3 m^{-2} s^{-1}) gas injection rates, where the overpressure gradient dominates the downward flow.
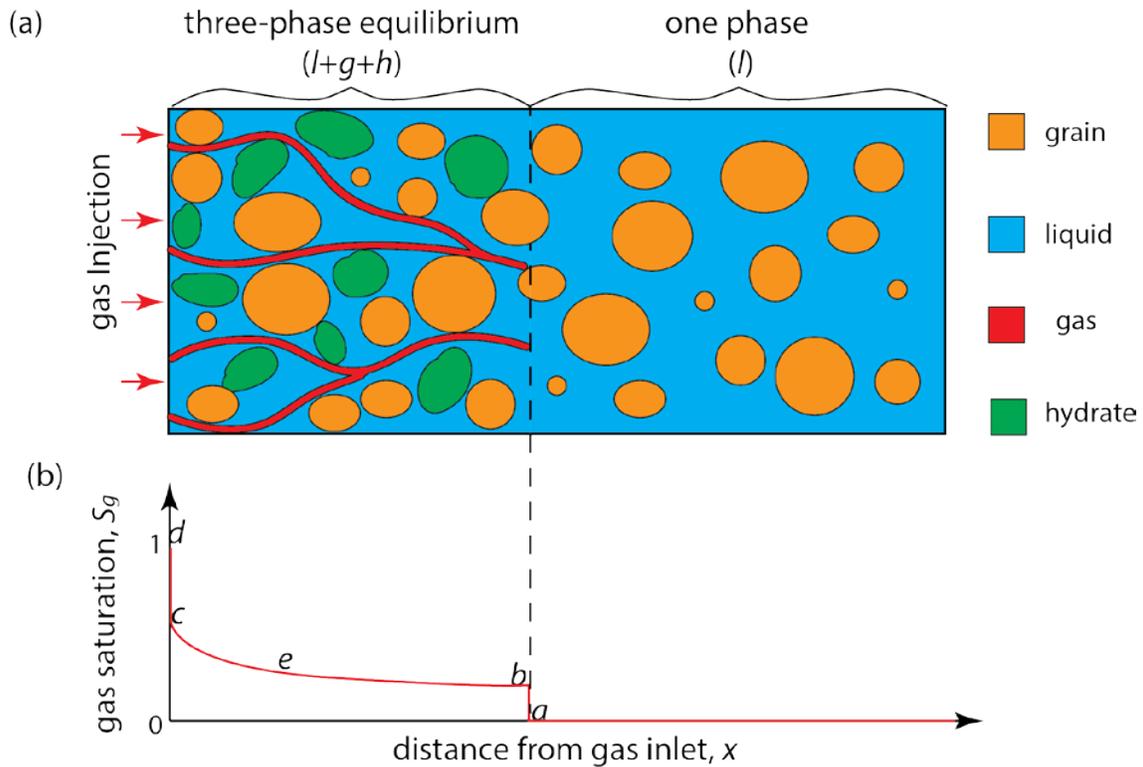
Figure 3: (a) Schematic diagram of methane gas injection into a brine-saturated sediment within the methane hydrate stability zone. (b) The corresponding gas saturation distribution. The system reaches three-phase equilibrium behind the hydrate solidification front (to the left of point b): in this region brine at an elevated salinity coexists with methane gas and hydrate. Gas saturation decreases from 100% at the upstream side of the gas inlet (point d) to 0% at the downstream side of hydrate solidification front (point a). l, g and h means liquid, gas and hydrate phases, respectively. Points a and b delineate the downstream and upstream sides of the leading shock, respectively. Points c and d delineate the downstream and upstream sides of the trailing shock, respectively. Point e is any position between point b and c.
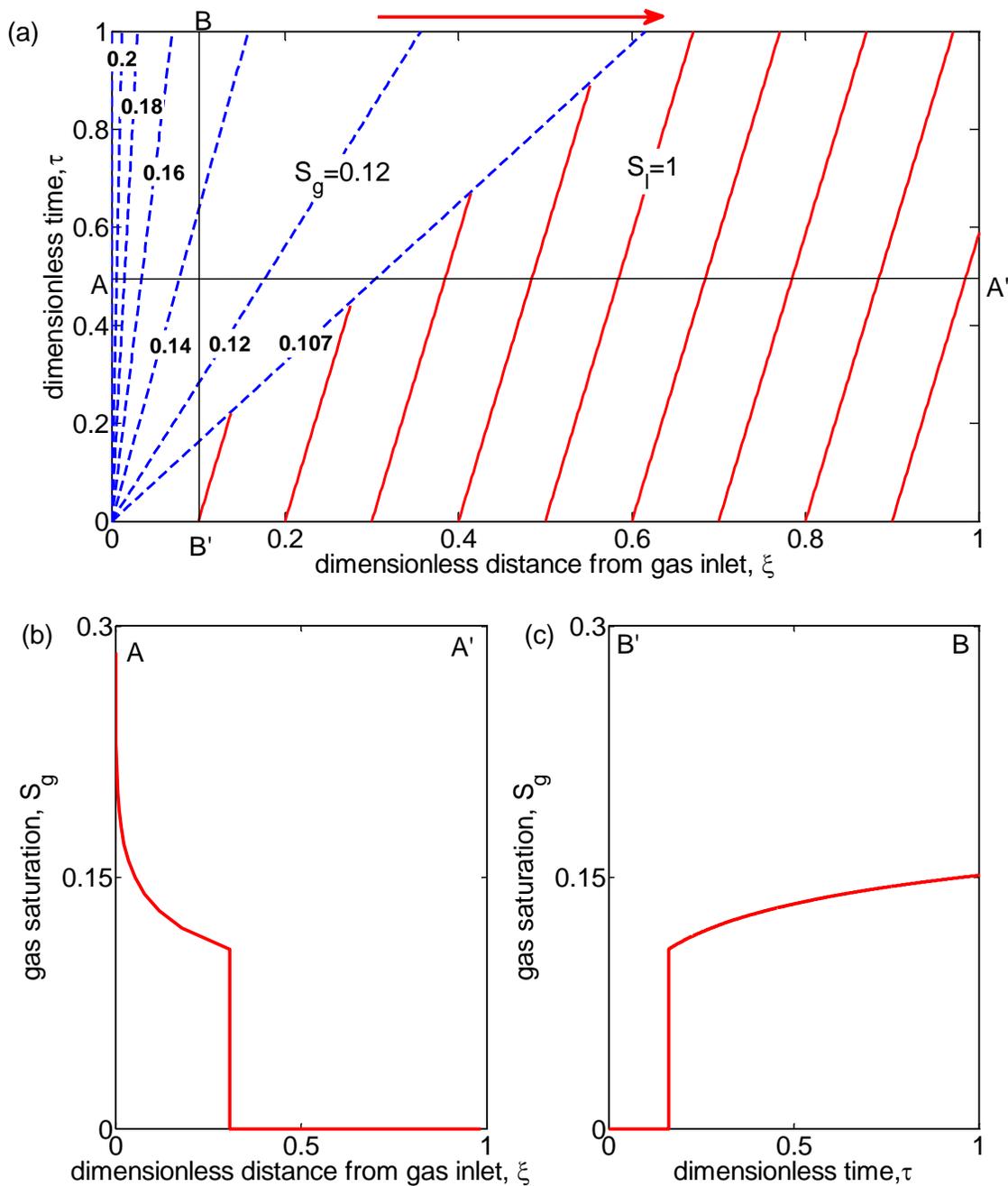
Figure 4: (a) Characteristics for methane gas injection into a brine-saturated sediment with the pressure of 6.89 MPa, temperature of 4 °C, initial salinity of 3 wt.% and gas injection rate of 10^{-6} m sec-1. The hydrate saturation is 0.684 behind the hydrate solidification front. The dashed blue lines are the characteristics for the discontinuity initially present at the gas inlet. Numbers on the blue lines are gas saturations. The red lines are the characteristics for the initial composition ($S_l=1$) in the sediment. The line $\tau = 0$ is the characteristics for the injection composition. (b) Change of gas saturation along line A-A' ($\tau = 0.5$). (c) Change of gas saturation along line B-B' ($\varepsilon = 0.1$). The red arrow on the top of shows the flow direction.
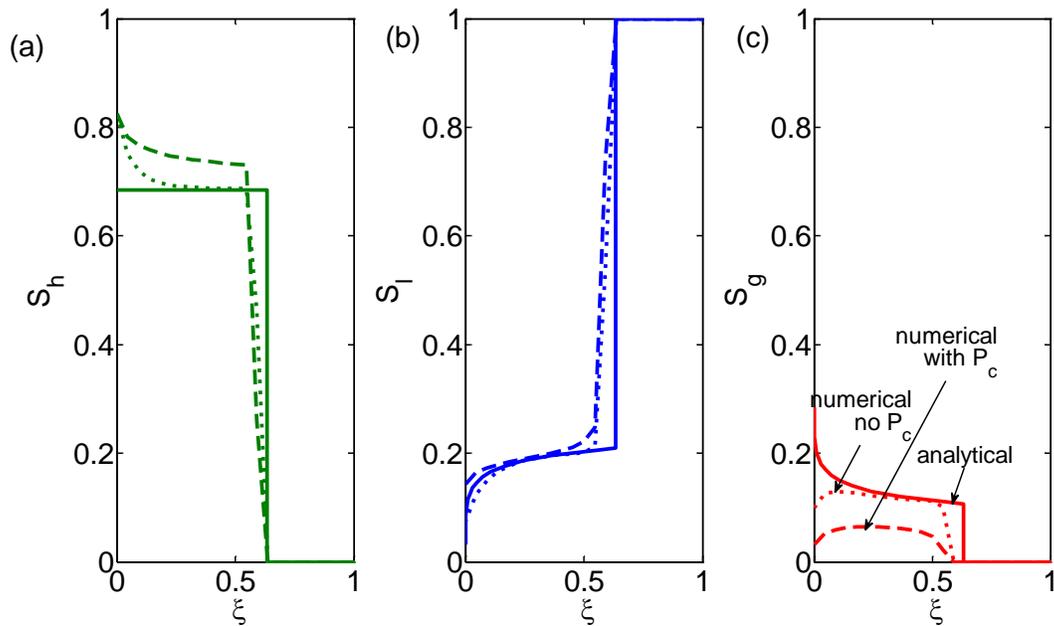
Figure 5: a) Hydrate (S_h, green lines), b) water (S_w, blue lines) and c) gas (S_g, red lines) saturation distributions in the sediment at dimensionless time 1.0 calculated by the analytical solution (solid lines), the numerical solution developed in Liu and Flemings (2007) with capillary pressure (dashed lines) and the numerical solution without capillary pressure (dotted lines).
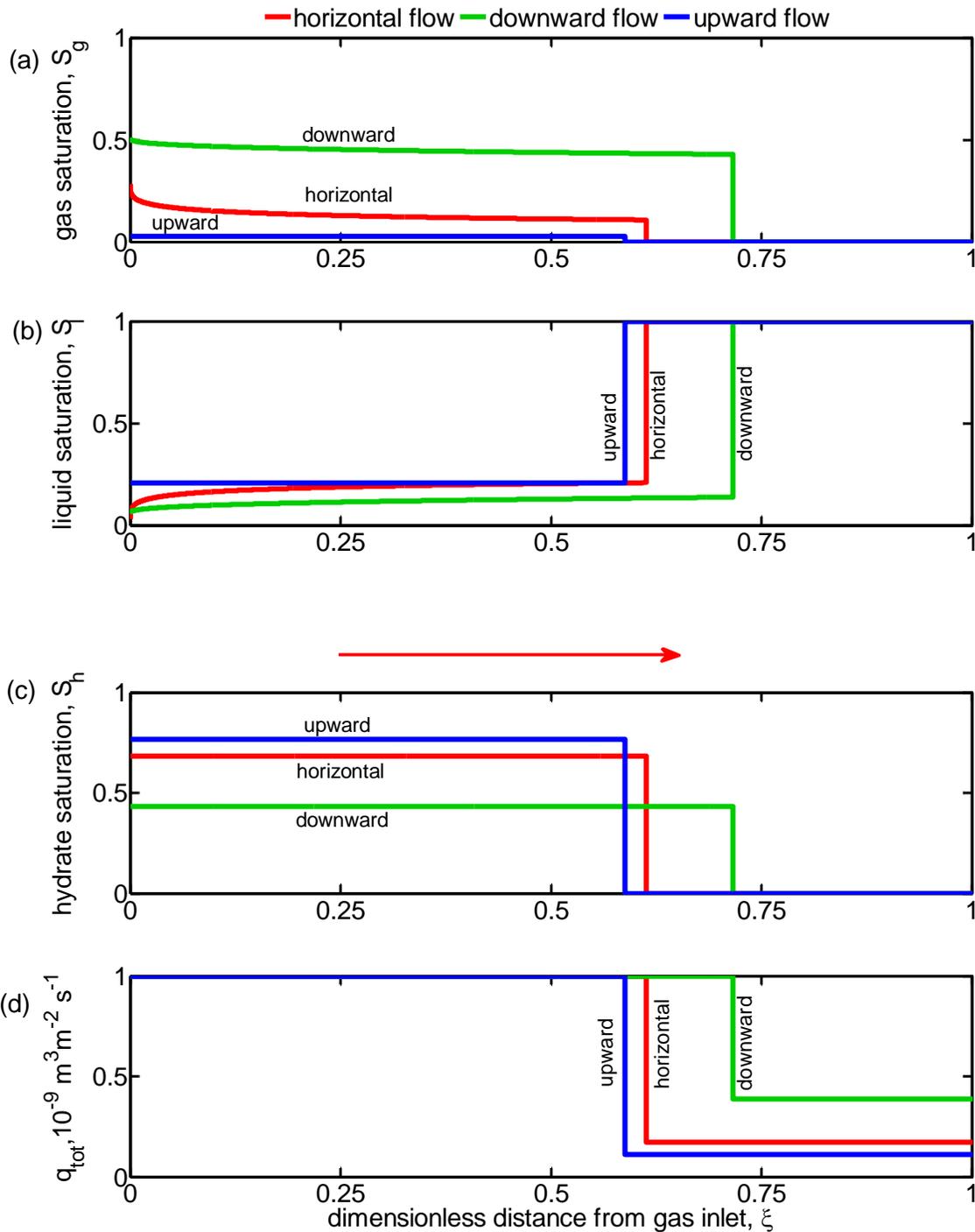
Figure 6: Comparison of (a) gas (S_g), (b) liquid (S_l), (c) hydrate saturation (S_h), and (d) total volumetric flux (q_{tot}) distribution at $\tau = 1$ for horizontal (red lines), downward (blue lines) and upward (green lines) flow at the gas injection rate of 10^{-9} m3 m-2 s-1. The red arrow indicates the flow direction. The thermodynamic and flow parameters are listed in Table 3.
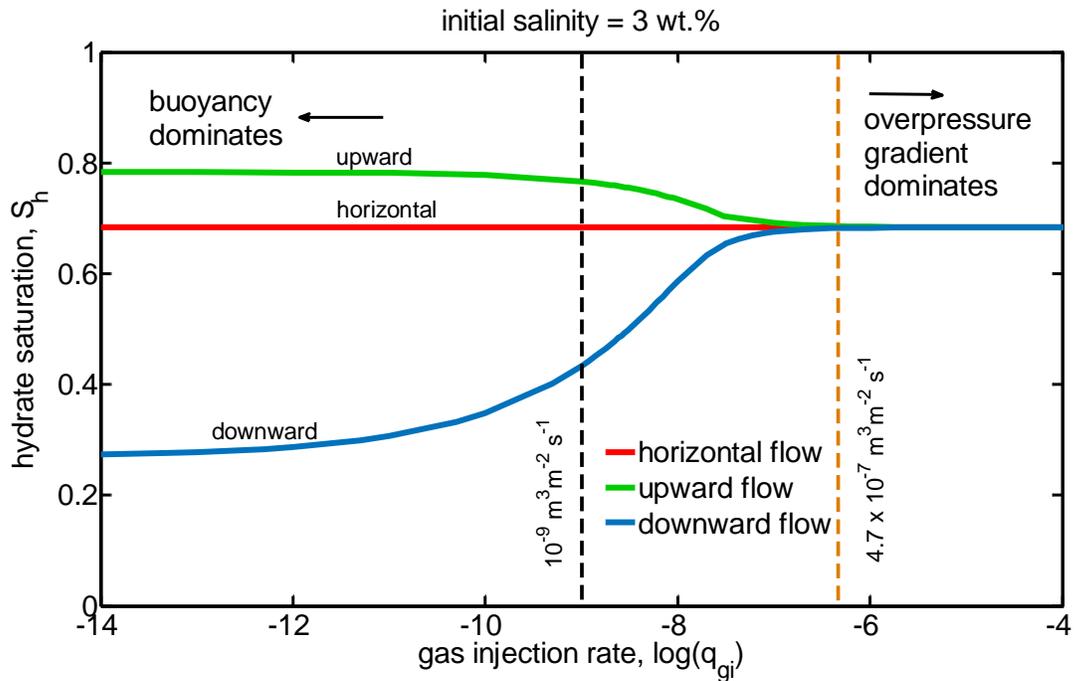
Figure 7: Change of hydrate saturation with gas injection rate for horizontal (red line), upward (green line), and downward flow into a hydrate stability zone at the pressure of 6.89 MPa, temperature of 4 oC and initial salinity of 3 wt.%. The flow parameters are listed in Table 3. The dashed orange line shows the critical flow rate of 4.7×10-7 m3 m-2 s-1. The dashed black line shows the flow rate of 10-9 m3 m-2 s-1. Gravity forces dominate the flow, and hydrate saturation depends on the flow direction when the flow rate is much less than 4.7×10-7 m3 m-2 s-1. Viscous forces dominate the flow, and hydrate saturation does not depend on the flow direction when the flow rate is much greater than 4.7×10-7 m3 m-2 s-1.

Table 3: Parameters used in the example calculation.

Variables	Physical meanings	Values
P_0	Pressure (MPa)	6.89
T_0	Temperature (^{o}C)	4
cl_0	Initial salinity (wt.%)	3
cl_e	Three-phase equilibrium salinity (wt.%)	10.96
L	Column length (m)	0.11
q_{gi}	Methane gas injection rate (m sec^{-1})	10^{-6}
ρ_{gi}	Density of gas injected (kg m^{-3})	56
ϕ	Porosity in absence of hydrate	0.35
ρ_h	Hydrate density (kg m^{-3})	912

k_0	Sediment intrinsic permeability without hydrate (m²)	10^{-13}
θ	Dip angle of the system (rad)	0
S_{gr}	Residual gas saturation	0.02
S_{wr}	Residual water saturation	0.1
μ_g	Gas dynamic viscosity (Pa sec)	2×10^{-5}
μ_l	Liquid water phase dynamic viscosity (Pa sec)	1.31×10^{-3}
$X_{M,h}$	Mass fraction of methane in hydrate (wt.%)	13.4
$X_{W,h}$	Mass fraction of water in hydrate (wt.%)	86.6

B.1.2.3 1D Numerical Fracture Growth Model

B.1.2.3a Introduction

We have been investigating the hypothesis that narrow, hydrate-filled fracture networks act as conduits for vertical gas migration through the hydrate stability zone. Our previous petrophysical analysis of various hydrate-bearing sites (Phase 1 report (Flemings, 2014b)), supported by additional published studies, has revealed that, in fine-grained material, hydrate frequently forms in high-angle fractures (Daigle et al., 2011; NGHP Expedition 01 Scientists, 2007; Rees et al., 2011; Riedel et al., 2010; Ryu et al., 2013). It is commonly hypothesized that these fractures form from the development of a gas reservoir beneath the GHSZ with a pore pressure that overcomes the least principle stress and creates hydraulic fractures in the overlying sediment (Daigle and Dugan, 2011; NGHP Expedition 01 Scientists, 2007; Rees et al., 2011; Riedel et al., 2010; Ryu et al., 2013). It is commonly hypothesized that these fractures form from the development of a gas reservoir beneath the GHSZ with a pore pressure that overcomes the least principle stress and creates hydraulic fractures in the overlying sediment (Daigle et al., 2011; Daigle and Dugan, 2011). Seafloor methane gas vents are also frequently observed above hydrate-filled fracture networks (Bangs et al., 2011; Haeckel et al., 2004; Torres et al., 2011), which suggests that these fracture networks also act as conduits for gas migration (Daigle and Dugan, 2011; Haacke et al., 2009; Mazumdar et al., 2009).

This observation has led researchers to question the mechanism that allows the vertical migration of gas in these fractures through the hydrate stability zone. Three primary hypotheses have been proposed (Figure 8). First, the kinetics of hydrate formation limit hydrate precipitation such that gas can migrate through the fractures without forming hydrate (Haeckel et al., 2004; Torres et al., 2004). Second, hydrate formation is limited by the amount of water available in the fracture such that, after some initial hydrate formation and gas consumption, hydrate ceases to precipitate and gas can migrate vertically (Clennell et al., 1999; Ginsburg and Soloviev, 1997). Finally, hydrate formation elevates the salinity in the pore water, producing three-phase equilibrium conditions and limiting the formation of additional hydrate, which allows the gas to pass through the remaining pore space (Liu, 2006; Meyer and Flemings, 2014; Milkov et al., 2004).(Liu, 2006; Meyer and Flemings, 2014; Milkov et al., 2004). As we have moved forward in our research concerning the formation of hydrate in fractures, we focused on this final

hypothesis as the primary mechanism for vertical gas migration, assuming that formation kinetics are negligible and that there is always water available to form hydrate.

B.1.2.3b Model Development

To gain some initial understanding of the physics controlling this process, we have developed a numerical model describing the movement of water and salt associated with the formation of hydrate in fractures. We are specifically interested in osmotic pressure as a potential driving force for fluid flow. The intrinsic osmotic pressure of a fluid is calculated with Equation 28 (Malusis et al., 2003):

$$u_{os} = -\omega \cdot v \cdot R \cdot T \cdot C \qquad \text{Eq 28}$$

where ω, v, R, T, and C are the chemico-osmotic efficiency coefficient, ion reaction constant, gas constant (8.314 J/mol-K), temperature (K), and salt concentration, respectively. The ω-value describes how ideally semi-permeable a membrane acts. A value of ω = 1 indicates an ideally semi-permeable membrane, while ω = 0 indicates a fully permeable membrane. A membrane with a ω > 0 separating two fluids of different salinities, will produce an osmotic pressure gradient that can result in fluid flow (Bader and Kooi, 2005). In our model, we assume a matrix of fine-grained material, which has been shown to act as a non-ideal, semi-permeable membrane. Although the ω-value is dependent on the porosity of the material and salt concentration of the fluid, it is typically non-zero (Barbour and Fredlund, 1989).

The model domain extends from the fracture wall to the half-fracture spacing and the model keeps track of the fluid overpressures (total, water, and osmotic), salinity, and porosity within the domain over time (Figure 9). External to the domain, within the fracture, the formation of hydrate increases the salinity of the water proximal to the fracture wall, increasing the osmotic pressure and decreasing the total pressure relative to hydrostatic pressure within the domain. This pressure gradient produces a driving force for the advection of water and salt from the matrix into the fracture, which supports the continual hydrate formation and salinity elevation. The model holds the following assumptions:

   a. One-dimensional model (homogeneous material)
   b. Constant water density
   c. Darcy's Law applied for water flow
   d. No salt diffusion
   e. Matrix acts a non-ideal semi-permeable membrane (ω = 0.01)
   f. All the water that enters the fracture forms hydrate
   g. Hydrate formation kinetics are negligible

Using water and salt mass balance and Darcy's Law (Eq. 31), we derived the follow water (Eq. 29) and salt (Eq. 30) advection equations and half-fracture thickness (Eq. 32) calculation:

$$\frac{du_w}{dt} = \left[\frac{k \cdot (1+e)^2 \cdot \sigma' \cdot \ln(10)}{C_c \cdot \mu} \right] \cdot \frac{du_{tot}}{dx} \qquad \text{Eq 29}$$

$$\frac{d(\phi C)}{dt} = - \frac{d(q_w C)}{dx} \qquad \text{Eq 30}$$

$$q_w = - \frac{k}{\mu} \frac{\partial (u_w - u_{os})}{\partial x} \qquad \text{Eq 31}$$

$$L_{frac} = \left[\frac{\rho_w}{\left(\rho_h \cdot \left(\frac{M_w}{M_H} \cdot n \right) \right)} \right] \cdot \int_0^t q_w(x=0)_t \cdot dt \qquad \text{Eq 32}$$

We then discretized equations B and C and solved them using an explicit, numerical method. The values for permeability (k) and compression index (C_c) were estimated from geotechnical tests previously performed on Resedimented Boston Blue Clay (RBBC) material (Schneider, 2011).

B.1.2.3c Results

The model was run on a domain 2 meters wide over a period of 1 year in order to achieve pressure equilibrium. The model results (Figures 10) express the following initial and boundary conditions as the solid lines:

   a. Constant hydrostatic pressure and three-phase salinity at fracture boundary
   b. No flow boundary at the half-fracture spacing
   c. Initially seawater salinity and hydrostatic pressure throughout the domain

Once the model starts, water flows down the pressure gradient toward the fracture, decreasing the water and total pressure in unison (Figure 10a). The reduction in water pressure results in a decrease in effective stress and a 0.33 percent decrease in porosity due to consolidation (Figure 10b). Additionally, the consolidation resulted in a 0.33 percent increase in salinity (Figure 10c). After a year, the total pressure reaches equilibrium across the domain and water ceases to flow into the fracture (Figure 10d). At this point, the amount of water that entered the fracture would make a hydrate-filled fracture approximately 1.6cm thick (Figure 10e).

B1.2.3d Conclusions

This model is a relatively simplistic look at the physics controlling hydrate formation in fractures; however the results provide some interesting initial understanding into this problem. The model uses well supported fluid flow physics with constrained sediment characteristics and produced a fracture thickness that is reasonable compared to those found in nature. This suggests that osmotic pressure gradients across fracture boundaries could be a reasonable driving force for water flow into a fracture and continual hydrate formation. From this point, we will be continuing our research in this area with additional model advancements, including salt diffusion, capillary-induced flow, and cryogenic suction effects.
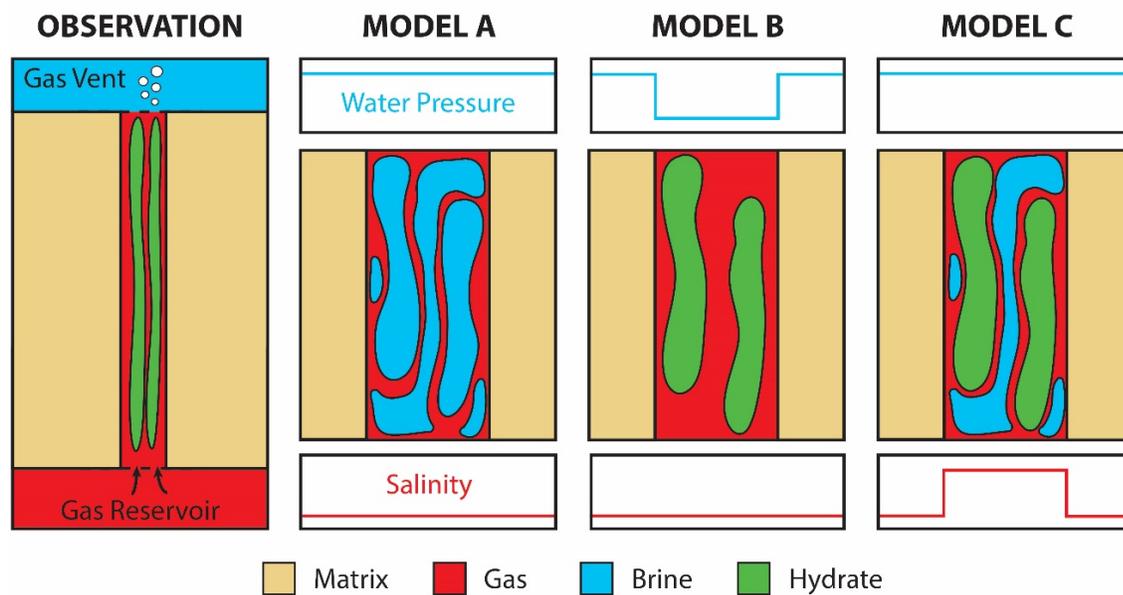
Figure 8: Cartoon describing the three major hypotheses presented to explain the observed methane gas vents associated with hydrate-filled fractures. Model A indicates that hydrate formation is limited by kinetics. Model B states that the hydrate consumes the readily available water and becomes water limited. Model C suggests that hydrate formation can locally elevate salinity and restrict hydrate formation.
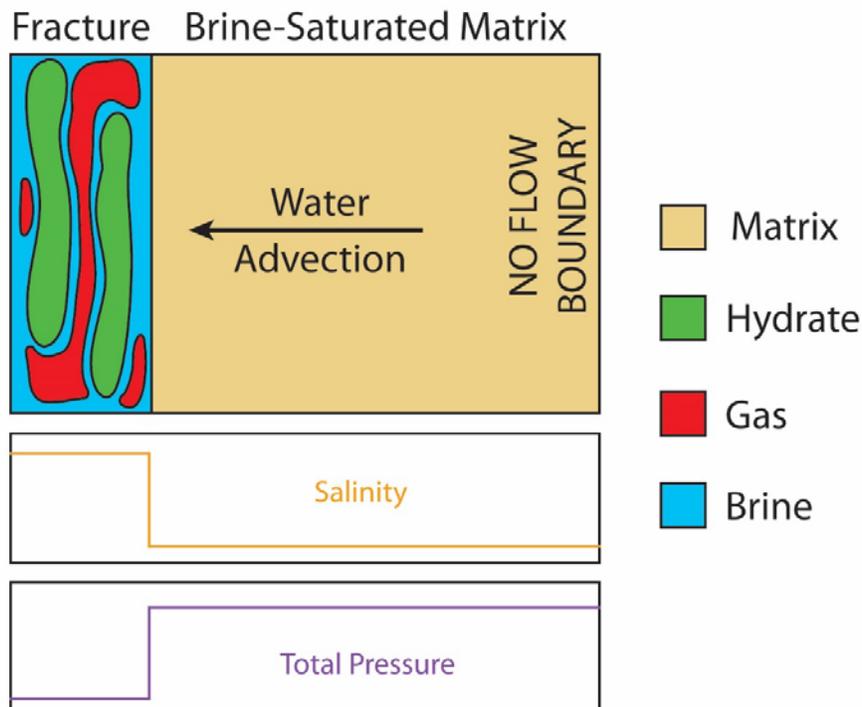
Figure 9: General conceptual model of osmotic pressure as a potential mechanism for water flow toward a fracture to support hydrate formation. Elevated salinity in the fracture, due to hydrate formation, reduces the total pressure in the fracture. This produces a pressure gradient that induces water advection toward the fracture.
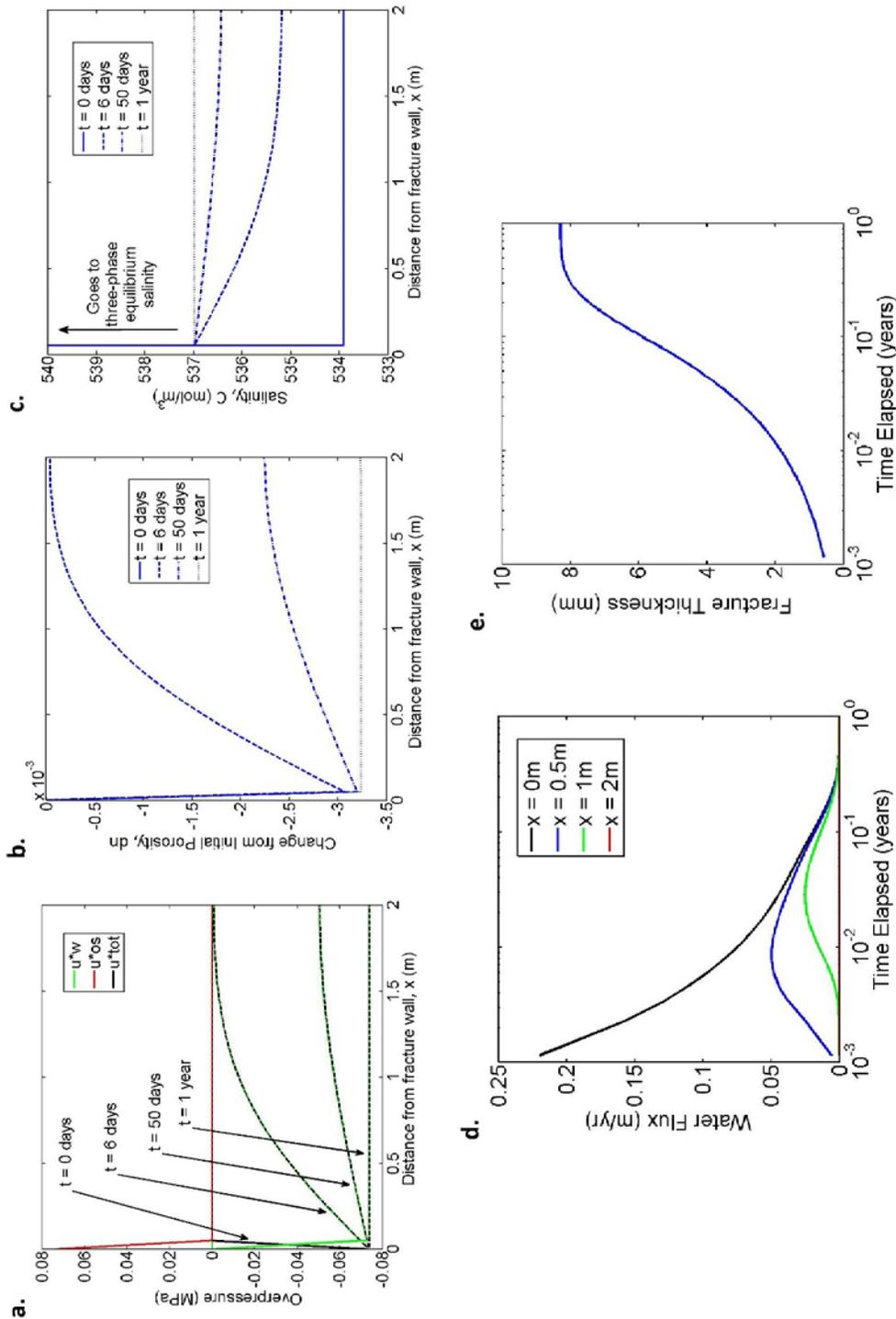
Figure 10: Compilation of the 1-year advection model results. A) Total (u*tot), water (u*w), and osmotic (u*os) overpressure profiles throughout time. B) Porosity profile across the domain during the model. C) Salt concentration within the matrix throughout time. D) Water flux over time at various points within the matrix. E) Fracture half-thickness as a function of time. Over the course of the model, water flows out of the matrix and into the fracture, reducing overpressures, porosity, and water flux and increasing salinity and fracture half-thickness.

B2. Subtask 5.2 - Apply 1D expulsion to laboratory experiments (Complete)

B2.1. Goal:

The Recipient shall validate the conceptual and physical basis of the gas expulsion model against experiments conducted in Task 6.

B2.2. Activities Phase 2:

In this section, we discuss the numerical simulation of experiment HVT0008 where methane gas invades into a vertically-placed hydrate stability zone from the top. The sediment has a length of 13 cm and diameter of 5.08 cm. Initially, the sediment is saturated with brine (NaBr) of salinity 7 wt.%, at the pressure of 12.24 MPa and temperature of 1 $^{\circ}$C (Figure 11). We keep a constant gas pressure of 12.24 MPa at the top to simulate the gas pump that is connected at the top of the sediment. We set a fixed water flow rate of 0.001 ml/min at the bottom to simulate the brine pump that is connected at the bottom of the sediment. We keep a constant sediment temperature of 1 $^{\circ}$C through the simulation.

When brine is pulled out from the bottom, the pressure in the sediment decreases. Methane gas flows in from the top and forms methane hydrate from the top of the sediment (Figure 12). Hydrate formation excludes salt, and increases the local salinity until three-phase equilibrium value (31 wt.%). The gas and hydrate fronts move further down the sediment with a velocity of 0.035 cm/hour. There are three phases, gas, hydrate and liquid, from the gas inlet to the hydrate solidification front, and salinity equals 31 wt.%. There is one phase, liquid, from the hydrate solidification front to the bottom of the sediment. And the salinity is slightly increased close to the front because of the salt advection and diffusion from the front. Gas breakthroughs at about 375 hours, when the entire sediment reaches three-phase equilibrium. Hydrate saturation decreases from 88% at the top to about 79% at the bottom, with a bulk saturation of 82% in the sediment. The measured gas consumption is much less than the numerical prediction (Figure 13: the orange line is much lower than the red line), but it is greater than the measurement brine consumption. This means there was hydrate formation in the experiment, but hydrate saturation was much lower than the three-phase value and the bulk system did not reach three-phase equilibrium.
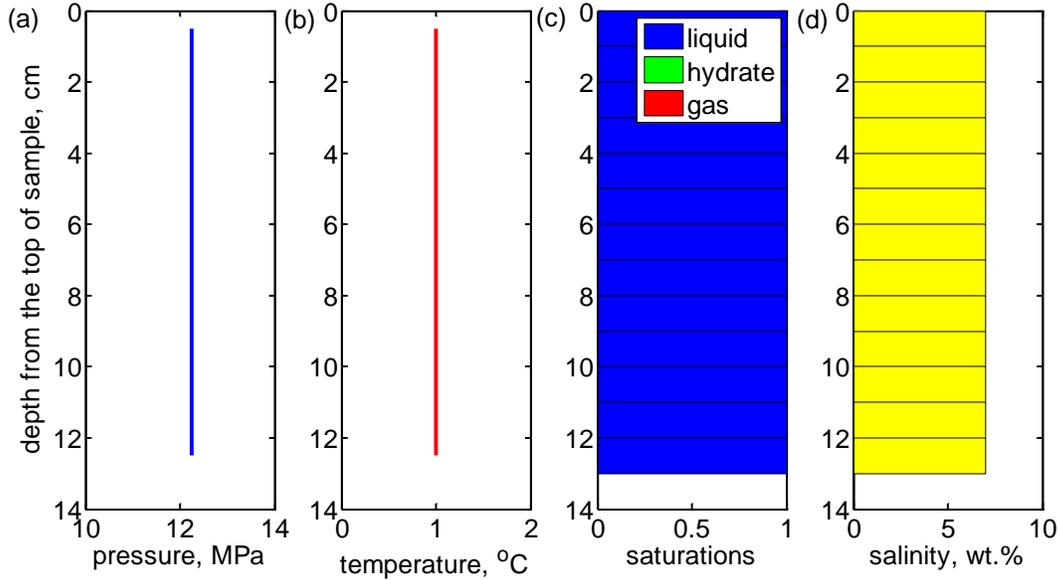
Figure 11: (a) the initial pressure, (b) temperature, (c) liquid (blue), hydrate (green) and gas (red) saturation, (d) salinity distribution in the sediment.
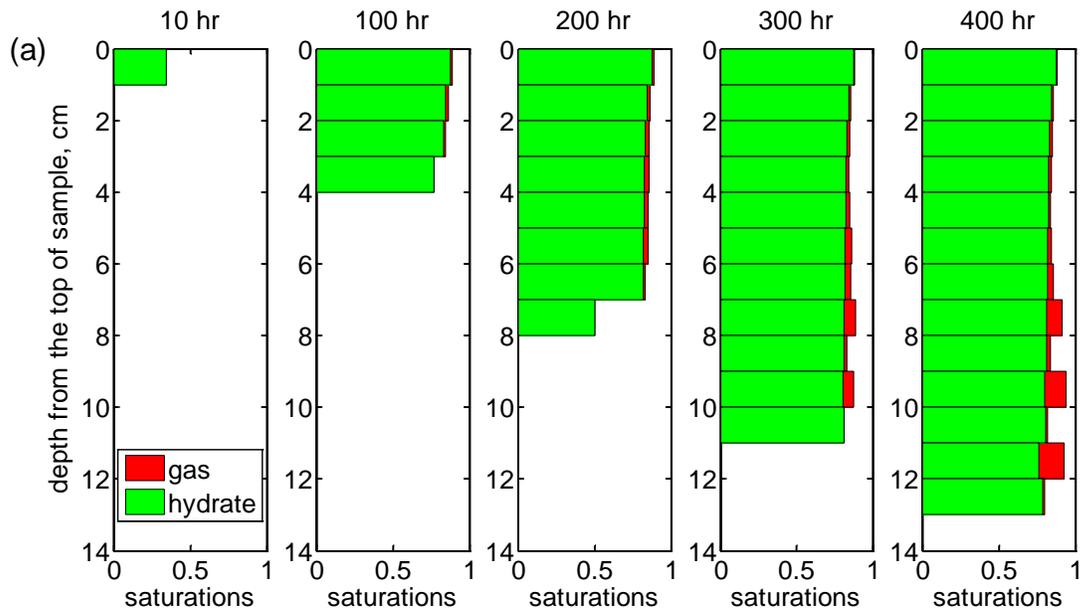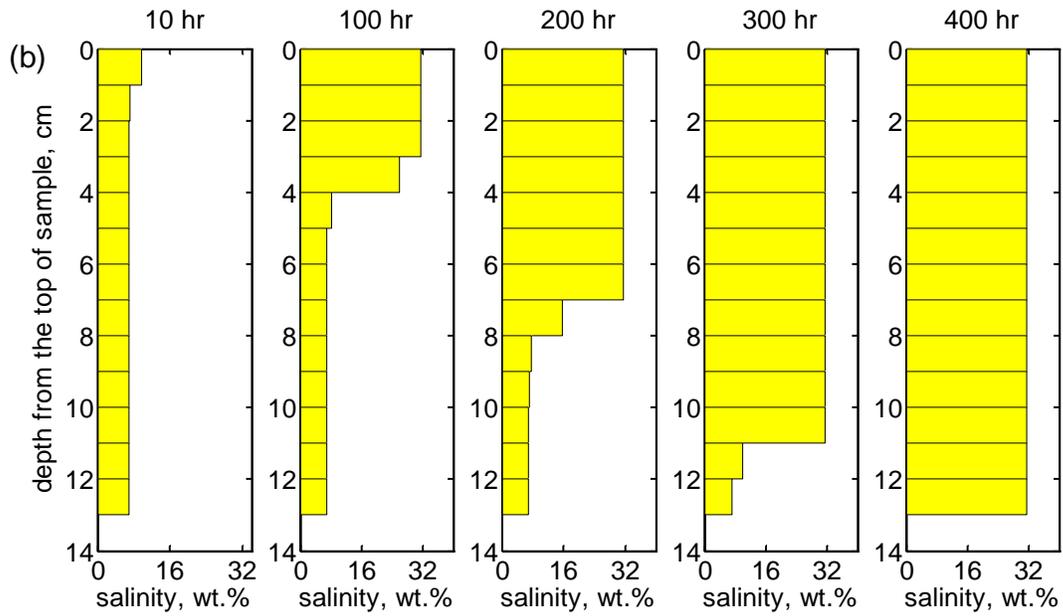
Figure 12: (a) hydrate (green) and gas (red) saturations, and (b) salinity (yellow) distribution in the sediment at 10, 100, 200, 300 and 400 hours after the start of brine withdraw.
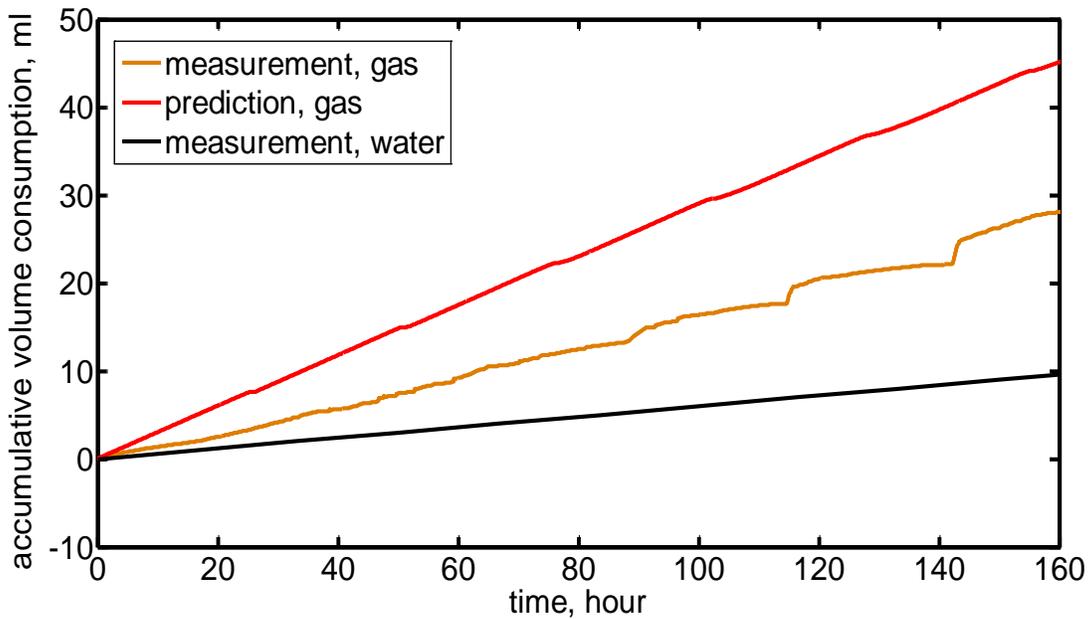
Figure 13: Comparison of the measured and numerically predicted accumulative gas consumption in the experiment HVT0008 .

Besides, we analyzed our laboratory experiments of gas invasion and hydrate front advancing using the MOC analytical model, which are discussed in subtask 6.1.

Subtask 5.3 - Apply 1D model of natural hydrate accumulations (Complete)

B2.3. Goal:

The Recipient shall simulate the migration of gas out of the hydrate‐bearing sediment, and shall determine conditions under which migration continues to the seafloor or atmosphere. Specifically, the latent heat of hydrate formation, the effect of salinity, and the effect of flow via fractures or matrix shall be included. The Recipient shall model the time evolution of the gas flow and predict under what conditions and at what rate gas will be vented. Initial conditions that are both within the liquid‐hydrate (L+H) stability region and within the three‐phase equilibrium (L+H+G) region shall be considered.

B2.4. Activities Phase 2:

The model has been developed and presented in the June 2014 quarterly report.

The model is currently being applied to the permafrost zone such as in Alaska (Figures 11-14) and to the deepwater continental margins (Figure 15).

Permafrost Zones:

The purpose of this section is to investigate the interrelated ice and hydrate melting during global warming. We use the Mallik gas hydrate field as an example. The same study can be extended to other hydrate fields. Mallik gas hydrate field is located in Mackenzie delta on the coast of Beaufort Sea, in the northwest territories of Canada (Haberer et al., 2005). It was shown to be one of the most concentrated gas hydrate deposits in the world (Dallimore and Collett, 2005). Relatively thick sections of high-saturation methane hydrate (often over 80%) lie between 897 and 1110 m (Taylor et al., 2005). Ice-bearing permafrost extends from ground surface to the depth of about 600m.

In our simulation, the initial water pressure increases hydrostatically with depth (Figure 14a). Present average ground surface temperature is -6 °C (Majorowicz et al., 2012) (Figure 14b). We set the initial temperature at the base of permafrost (600 m) at -1 °C (Henninges et al., 2005) (Figure 14b). Below the base of permafrost temperature increases linearly with the gradient of 26 °C km^{-1} (Figure 14b). A fixed geothermal flux of 56 mW m^{-2} is applied at the bottom (1400 m), providing an equilibrium initial temperature distribution. Sediments in the shallow depth of the Beaufort-Mackenzie Basin is largely terrestrial, and low salinities below 0.1-0.5 wt.% can be expected (Dallimore and Collett, 2005). We assume the salinity from ground surface to 600 m to be 0.5 wt.% in absence of ice. We also assumes there is no salt transport during ice freezing. The initial ice saturation S_{i0} can be calculated from the salinity $X_{l0}^s = 0.5 wt.\%$ and the salinity when ice equilibrates liquid phases X_{l+i}^s (calculated from the initial temperature and ice-liquid phase boundary) as $S_{i0} = 1 - \dfrac{X_{l0}^s}{X_{l+i}^s}$ (Figure 14c). The BHSZ is at 1100 m.

Two hydrate layers with variable saturations are present from 900 to 1000 m, and from 1080 to 1100 m (Figure 14c). The initial hydrate saturations are obtained by averaging the nuclear magnetic resonance-derived gas hydrate saturation for Mallik 5L-38 well (Dallimore and Collett, 2005). The initial salinity decreases with depth in the permafrost, and is uniformly 3 wt.% beneath the base of permafrost (Figure 14d). The porosity is uniformly 35%, and the permeability of the hydrate and ice-free sediments is 10^{-13} m^2 (Dallimore and Collett, 2005).

At 0 k.y. we increase the ground surface temperature linearly from -6 to 0 °C for 300 years and then keep the surface temperature at 0 °C to reflect future climate warming caused by doubling of CO_2 (Majorowicz et al., 2012). Ice melts from ground surface immediately because the local thermal condition is initially on ice-liquid phase boundary (Figure 15). Ice also melts from the base of permafrost (Figure 15c), which is caused by the geothermal flux (Archer, 2015). Ice front retreats faster from the base of permafrost (Figure 15c). There are two reasons for this: first, the initial ice saturation decreases with depth and reaches minimum at the base of permafrost; second, there is a large initial salinity gradient toward the base of permafrost (Figure 15d), and salt diffuses into the base of permafrost and promotes ice melting there. At 18 k.y. the ice has shrunk to the depth between 40 and 420 m with an average saturation of 40% (Figure 15c). The entire ice layer disappears at 33 k.y. from 60 m in depth.

Hydrate starts to dissociate at 16 k.y. from the BHSZ, where the initial thermal state is most close to the hydrate phase boundary. Hydrate dissociation provides methane to the shallower hydrate layer, and secondary hydrate forms there (Figure 15c). Hydrate melting decrease the local salinity, and secondary hydrate formation increases the local salinity. Both effects bring the local system to three-phase (hydrate, liquid and gas) equilibrium and creates a gas pathway in the hydrate deposit (Figure 15c). The entire hydrate deposit and the gas front move upward with old hydrate melting and secondary hydrate formation (Figure 15c). Methane gas reaches ground surface and starts venting to atmosphere at 38 k.y., when hydrate deposit rises to the depth between 540 to 920 m. Hydrate deposit continues rising with methane gas venting at ground surface. Hydrate disappears at 55 k.y.. At 68 k.y. residual gas saturation (2%) remains in the sediment. Temperature is still increasing in the domain (Figure 15a). Ice and hydrate melting redistributes salinity in the sediment (Figure 15b). Salinity in the initial ice layer is much lower than the initial value (Figure 15b). Salinity in the initial hydrate layer reduces to two third to three fourth of the initial value (Figure 15b). We call this melting scenario as melting-1. During melting methane gas front is always far below the base of permafrost before ice disappears. For example, gas front is at 760 m when the remaining ice layer is at 60 m. Therefore, ice cannot prevent methane venting to atmosphere by decreasing the sediment intrinsic permeability.

When the initial ice saturation in each depth is reduced to one half (melting-2) and to zero (melting-3), methane gas starts venting at ground surface at 30 k.y. and 21 k.y., respectively, which was advanced by 8 k.y. and 17 k.y. respectively (Figure 16). There are two stages of gas venting at ground surface. The first stage lasts about 6 k.y. with an average gas flux of about 170 g m^{-2} yr^{-1} (Figure 16). The second stage lasts around 10 k.y. with an average gas flux of about 100 g m^{-2} yr^{-1} (Figure 16)

We then move the base of permafrost to 300 m. This yields a HSZ between 260 and 580 m. We move the entire hydrate deposit to the depth between 380 and 580 m, and do the same melting simulation as in melting-1. We call this simulation as melting-4. Methane gas starts venting at ground surface at 8.5 k.y. and lasts until about 18.5 k.y., when the entire hydrate deposit disappears and residual gas saturation remains in the domain (Figure 17). Different from melting-1, -2 and -3, gas venting at ground surface in this case lasts for shorter time but with a much higher average flux, about 200 g m^{-2} yr^{-1}.

We then investigate the effect of sea level rise. We set the initial water depth at ground surface to be zero. We increase the water depth with a rate of 3 mm yr^{-1} for 1 k.y. We then keep the water depth at 3 m for the remaining time. We immediately increase the ground surface temperature from -6 to 0 °C at 0 k.y. to simulate seawater flooding. We call this case melting-5. We have two drives for ice and hydrate dynamics in melting-5: the first is water pressure, and increasing water pressure stabilizes both ice and hydrate in the sediments; the second is temperature, and increasing temperature destabilizes both ice and hydrate. Very similar melting behavior is obtained with melting-1, except that the increasing water depth delays the time when gas starts venting at ground surface by 1 yr (Figure 17).
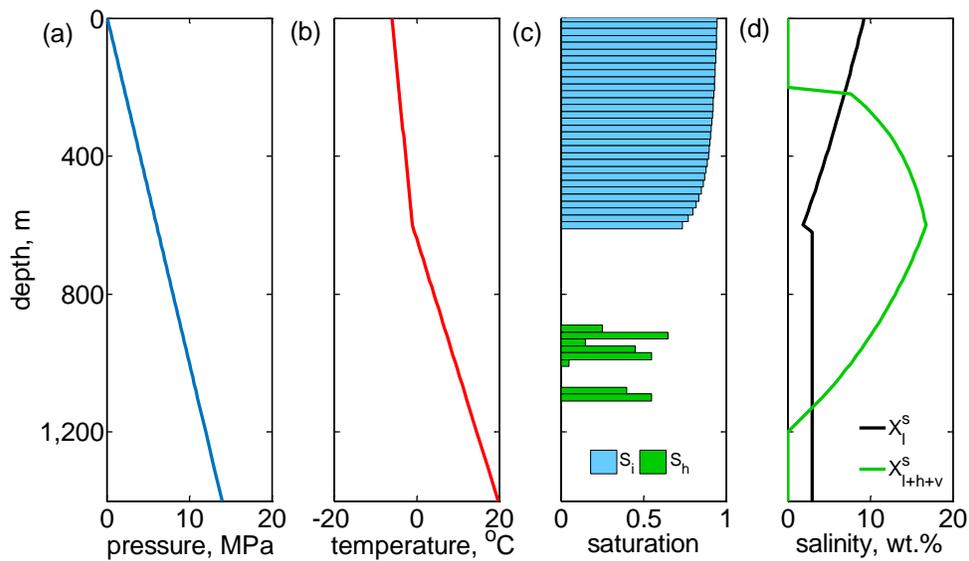
Figure 14: Initial (a) pressure, (b) temperature, (c) saturation and (d) salinity distributions for Mallik site hydrate melting simulation. Si is ice saturation, Sh is hydrate saturation, Xsl is initial input salinity, and Xsl+h+v is three-phase equilibrium salinity for liquid, gas and hydrate phases.
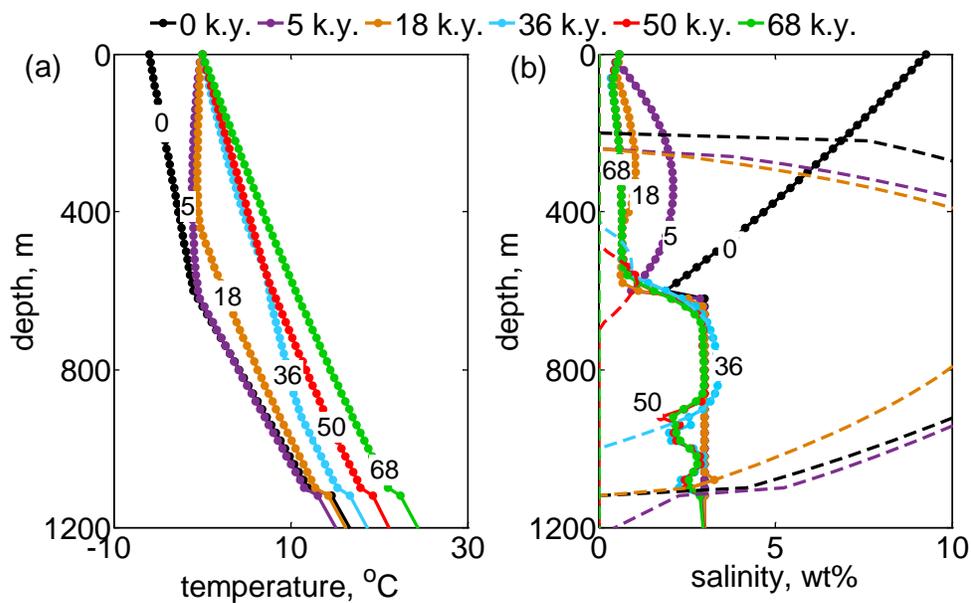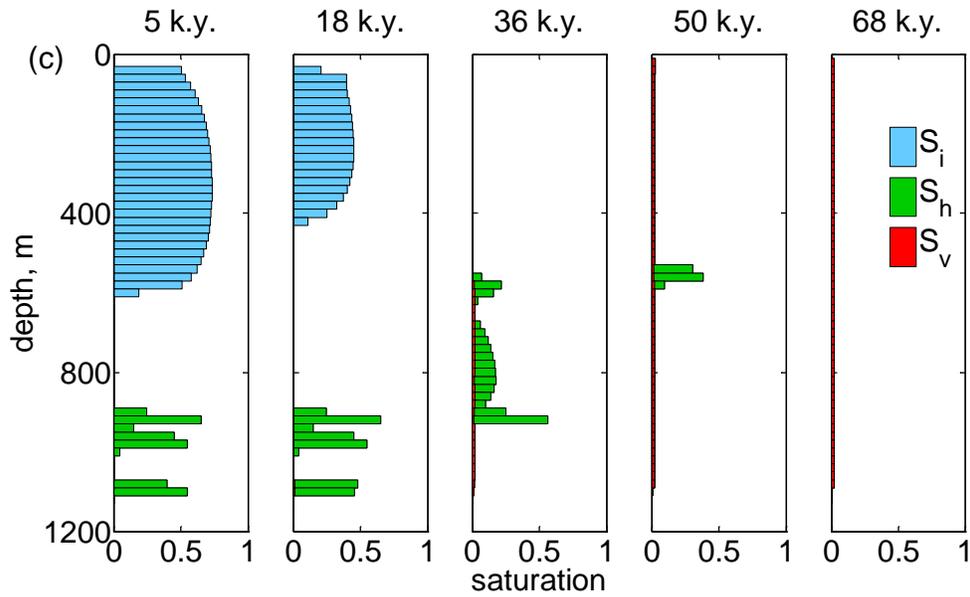
Figure 15: Hydrate and ice melting at Mallik site with average ice saturation 90%. (a) temperature, (b) in-situ salinity (solid lines with dots) and three-phase equilibrium salinity (dashed lines), and (c) ice (blue), hydrate (green) and gas (red) saturation distributions at 0 (black), 5 (purple), 18 (brown), 36 (blue), 50 (red) and 68 (green) k.y., respectively.
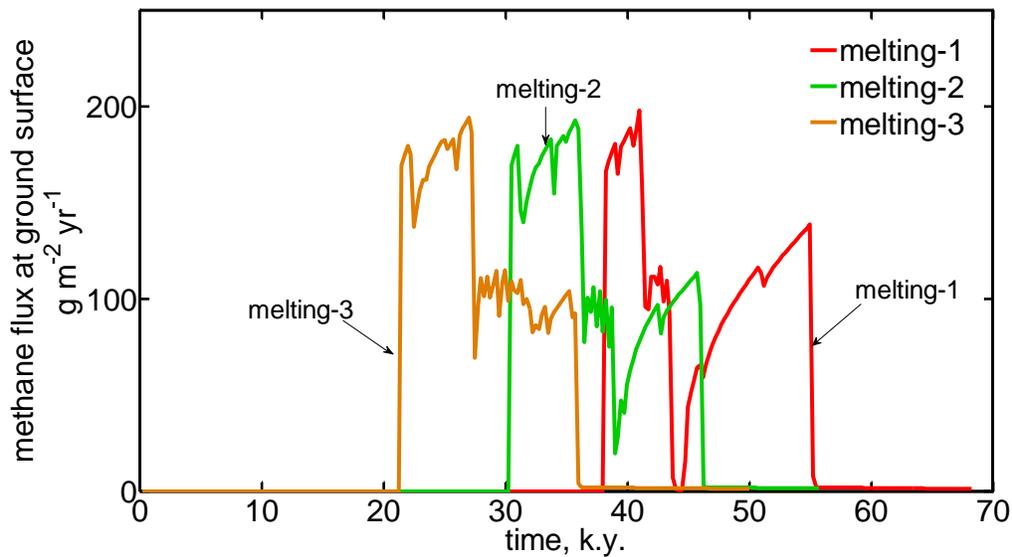

Figure 16: Evolution of methane gas flux at ground surface in response to future global warming when the base of permafrost is at 600 m, and the average ice saturation is 90% (melting-1), 45% (melting-2) and zero (melting-3).
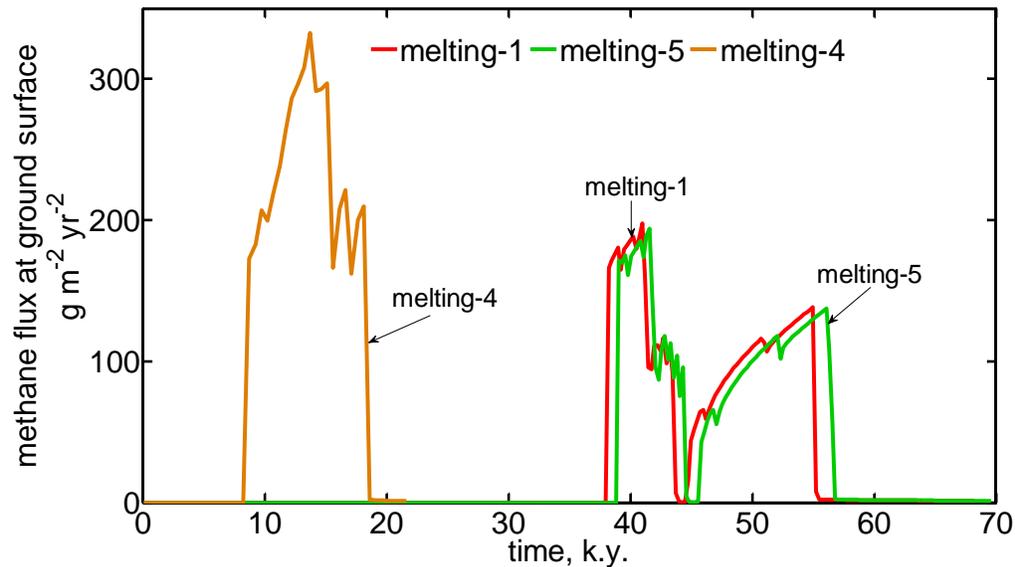
Figure 17: Evolution of methane gas flux at ground surface in response to future global warming when the base of permafrost is at 600 m (melting-1) and 300 m (melting-4), and in response to sea water transgression when the base of permafrost is at 600 m (melting-5).

Continental Margins:

On continental margins, we have extended our numerical results to describe the general behavior of venting in hydrate systems. Our results constrain when gas will vent due to a thermal perturbation and when it will not (Milestone 2.B). An analytical model captures the general behavior.

In the analytical model, we compare the mass of gas liberated by warming against the mass of gas that the warmed and shortened gas hydrate stability zone (GHSZ) can actually convert to hydrate. The liberated hydrate amount determined by the initial conditions, while the allowable hydrate amount in the warmed and shortened GHSZ is set by the three-phase equilibrium conditions. If more gas is available due to warming than is allowable by the system, venting temporarily occurs.

We calculate the depth of the BHSZ after complete warming, B_f. We assume that all hydrate beneath B_f dissociates, that no hydrate is initially above B_f, and that any salt transport is negligible[1]. We estimate the mass of gas supplied by dissociation, α, as

$$\alpha = A\theta_g \int_{B_f}^{B^i} S^i_h(z)dz,$$

Eq 33

where S^i_h is initial hydrate saturation, ρ_h is hydrate density and A is the nominal area (1 m²), θ_g is the fraction of methane contained in hydrate ($\theta_g = 0.14$ by assuming a hydration number of 6). We

---

[1] Multiple simulations showed that salt transport was negligible.

then calculate how much gas, γ, is necessary to establish a three-phase equilibrium chimney from B_f to the seafloor.

$$\gamma = A\theta_g \int_0^{Bf} S^{eq}{}_h(z)dz = A\theta_g \int_0^{Bf}(1 - {}^{c_0}/_{c_{eq}(z)})dz \qquad \text{Eq 34}$$

where S_h^{eq} is the hydrate saturation corresponding to three-phase equilibrium salinity, c_0 is the initial salinity (3.5 w.t. %), and c_{eq} is the three-phase equilibrium salinity after complete warming. Then, Λ is the ratio of gas supplied (α) to the amount of hydrate needed to form a vent (γ):

$$\Lambda = \alpha\gamma^{-1}. \qquad \text{Eq 35}$$

Transient venting occurs when $\Lambda > 1$ and when a GHSZ remains after warming ($B_f > 0$). *Complete venting* occurs when the GHSZ vanishes after warming ($B_f \leq 0$), and *no venting* occurs under all other scenarios. This analytical approach predicts similar behavior to the multiphase flow model. These simulations produce *transient venting* within the expected *transient venting* temperature range of the analytical model (filled circles, Figure 18b).

We use equation (4) to analyze venting for an idealized continental margin (Figures 13a and 13b) that has the same initial seafloor temperature and geothermal gradient as our previous simulations. A bottom water temperature increase of 2.5∘C shoals the base of the hydrate stability zone upward approximately 80m (dashed lines, Figure 18a). *Complete venting* occurs over a lateral distance of 400m, where the GHSZ vanishes ($B_f \leq 0$). *Transient venting* occurs over a finite distance downdip of the GHSZ pinch-out. According to the linear relationship between S_h^i and Λ in equations (2)–(4), the width of the *transient venting* zone is dependent on the concentration of hydrate within the dissociated layer (thick lines, Figure 18b). For instance, a few percent hydrate saturation causes venting for only tens of meters seaward of the GHSZ pinch-out, while nearly 100% hydrate saturation would be necessary to cause venting several kilometers seaward of the pinch-out (between vertical white lines, Figures 18a and 18b). If we assume 5% hydrate saturation, then the *transient venting* region spans approximately 200m downdip of the apparent pinch-out of the GHSZ (between vertical white lines, Figures 18a and 18b).

We evaluate the sensitivity of the analytical model (Figure 19) by perturbing the model from a base state. For this sensitivity, we perturb the water depth, seafloor temperature, magnitude of warming, geothermal gradient, and initial hydrate saturation. We include one base state that matches the conditions present in the example of transient venting (Figure 19a) and a second base state that does not produce venting (Figure 19b). Water depth and seafloor temperature (combined temperature from T_{sf} and ΔT) have the most dramatic effect on the results (Figure 19), since they control the locations of the BHSZ before and after warming. In addition, the initial hydrate saturation has a significant effect on the results where greater initial hydrate increases the potential for venting (Figure 19). These basic relationships are corroborated in the multiphase model (Figure 20). We provide a code at https://github.com/kdarnell/TransientVenting that calculates Λ for a given set of input parameters.
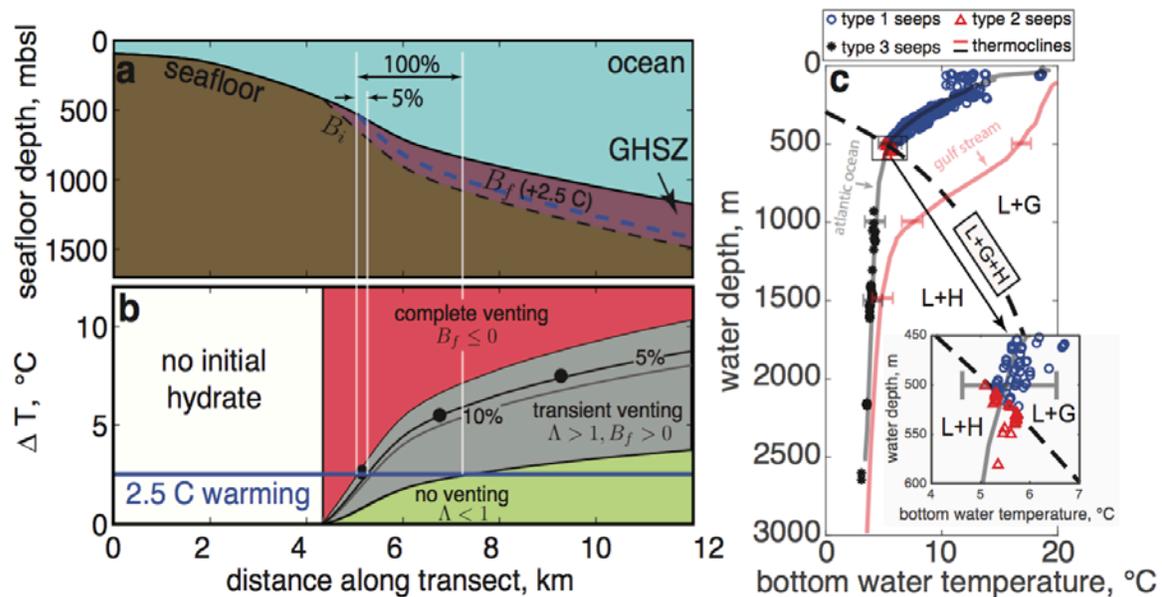
Figure 18: (From Darnell and Flemings (2015)) Venting predictions for an idealized continental margin using simple analytical model (equations (1)–(3)) and venting observations from a seep database. (a) Dip section of continental margin taken from eastern Atlantic. Black dashed line denotes initial BHSZ (Bi), and blue dashed line denotes warmed BHSZ (Bf). (b) Modeled warming response for initial 3°C seafloor temperature with 40°C/km thermal gradient and initial salinity of 3.5 wt %: complete venting (red region) for a large warming, no venting (green region) for a small warming, and transient venting (gray region) for warming in between end-member responses. Transient venting at a given temperature change occurs at hydrate saturation greater than saturation curve. Black, filled circles denote multiphase simulation results that record transient venting at 10% hydrate saturation. Vertical white lines denote region where transient venting is expected at warming of 2.5∘C for 5% and 100% hydrate saturation. (c) Hydrate phase diagram of calculated bottom water temperature using conductivity- temperature-depth (CTD) from World Ocean Database (Levitus et al., 1998) versus reported water depth for the 577 seeps observed by Skarke et al. (2014). Faint black and red lines denote the Atlantic Ocean and Gulf Stream thermoclines identified by Phrampus and Hornbach (2012).. Dashed line denotes the three-phase equilibrium (L + G + H) boundary for a salinity of 3.5 wt % and a density of 1030 kg m−3. Hydrate stability (L + H) occurs below L + G + H boundary. Twenty-nine Type 2 seeps (red triangles) are estimated to lie within the present-day hydrate stability zone but less than 2°C from destabilization.

We compare our venting predictions with a database of seeps identified by Skarke et al. (2014) (Figure 18c). We use their published water depths and geographical coordinates to calculate bottom water temperature using CTD data from the World Ocean Database (Levitus et al., 1998). These temperatures compare well with the Atlantic Ocean thermocline (Figure 18c) identified by Phrampus and Hornbach (2012).

We plot the seeps in a temperature versus water depth hydrate phase diagram (Figure 18c) assuming seawater salinity (3.5 wt %) and converting water depth to a hydrostatic pressure (with ρ = 1030 kg m−3). We identify three types of seeps (Figure 18c). Type 1 seeps (blue circles, Figure 18c) are located outside of the hydrate stability zone. Type 2 seeps (red triangles, Figure 18c) are located within the hydrate stability zone but would require warming of less than 2°C to destabilize hydrate. Type 3 seeps (black asterisks, Figure 18c) are well within the hydrate stability zone.

We interpret that the Type 2 seeps (29 of 577 seeps) could be transient vents, but additional field data are needed for confirmation. We base our interpretation on the fact that these Type 2 seeps are located where gas should not be stable (red triangles, Figure 18c) for the calculated seafloor temperature and assumed seawater salinity. Therefore, temperature or salinity at these seeps must be locally increased to explain their presence if thermodynamic equilibrium is assumed. The seeps may even be at three-phase equilibrium as has been shown for seeps in the Gulf of Mexico (Smith et al., 2014). If only salinity is elevated, we calculate the elevated salinity required for local three-phase equilibrium ranges from 3.55 wt % to 6.1 wt % depending on the temperature and water depth of each seep. Thus, transient venting induced by past warming, as might have occurred since the Last Glacial Maximum, could produce three-phase conditions and explain the present-day gas venting at these seeps. Precise bottom water temperature, seafloor salinity, and gas composition will test this interpretation.
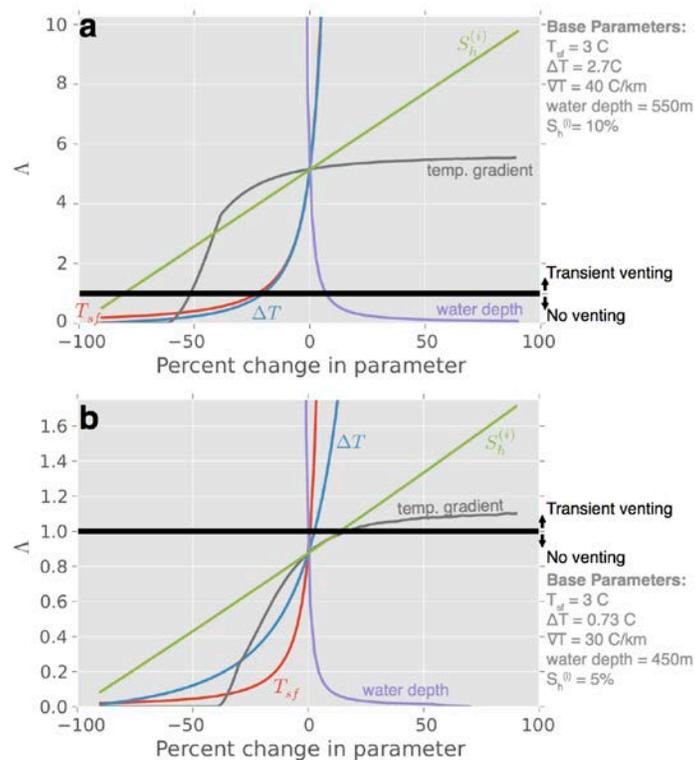

Figure 19: (From Darnell and Flemings (2015)) Sensitivity analysis of analytical model with variations to the seafloor temperature (Tsf), seafloor warming (ΔT), seafloor temperature gradient (∇T), water depth, and initial hydrate saturation ($S_h^{(i)}$). Each parameter is adjusted in isolation as a percentage change of its base value while all other parameters remain fixed. The resulting Λ value calculated from equation (4) is used to determine whether or not transient venting occurs. (a) The base parameters are the same as those used in the example of the main text, which produced transient venting. (b) Arbitrary base parameters that are different parameters from Figure 6a and where the base parameters produce no venting.
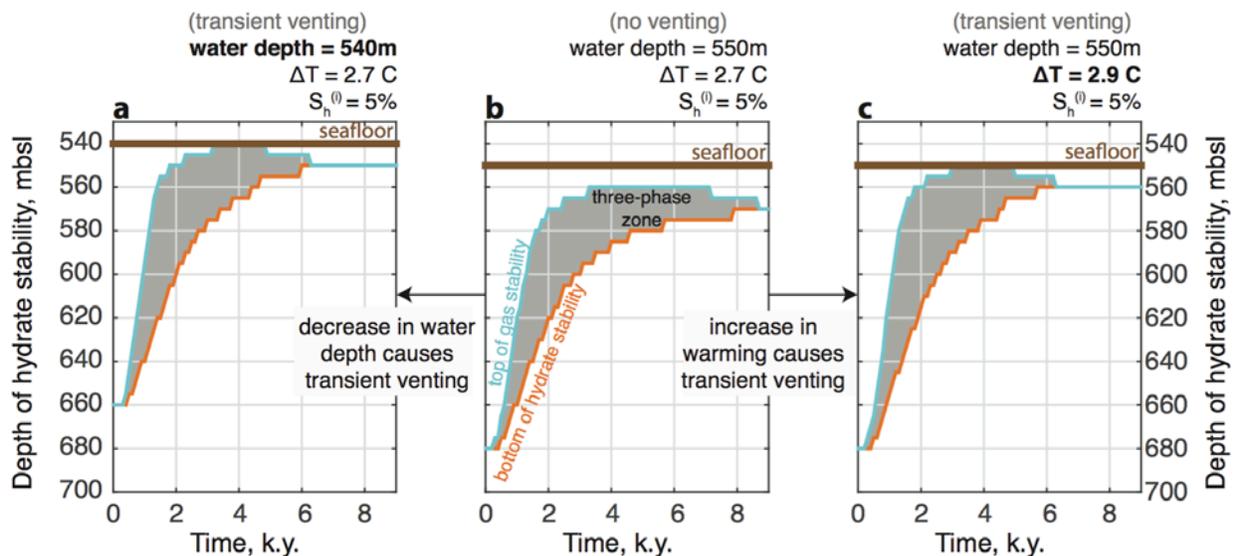
Figure 20: (From Darnell and Flemings (2015)) Comparison of multiphase dynamic simulation for initial hydrate saturation of $S_h^{(i)}$ = 5% with small variations in model parameters. For all three panels, the temperature gradient (40 °C/km) and initial seafloor temperature (3 °C) are held constant. Middle panel (b) is the base case. (a) Trajectory of hydrate/gas stability as a function of time where the water depth has been decreased by 10 meters from (b). (b) Trajectory of hydrate/gas as function of time where all parameters are equal to an example that produces transient venting, except $S_h^{(i)}$ has been decreased from 10% of pore volume to 5%. The gray area is the three-phase zone, which is located between the top of gas stability (cyan line) and bottom of hydrate stability (orange line) (c) Trajectory of hydrate/gas stability as a function of time where the temperature has been increased 0.2 °C from (b).

2.3. Task 6: Gas expulsion experiments (Complete)

Milestone 2.C Demonstration of reaction transport experiment where gas invades hydrate stability zone and creates three phase stability.

A. Goal:

The Recipient shall provide data to validate the gas expulsion model developed in Task 5, and to provide insight into whether this process of hydrate formation is self‐limiting. The hydrate saturation profile formed as gas invades the hydrate stability zone shall be representative of hydrate‐bearing sediments along continental margins. Thus the dissociation portion of the experiment also provides insight into possible differences in behavior between Arctic and oceanic systems.

B. Activities Phase 2:

B1. Subtask 6.1 - Gas invasion into water-saturated hydrate saturated zone

B1.1. Goal:

The Recipient shall perform a test to determine gas invasion into a water-saturated hydrate saturated zone. In this test, the vessel shall be filled with coarse sand and then X-ray CT scanned. The sand shall then be saturated with seawater and re-scanned. Temperature shall be held constant everywhere so

that the entire column is within the hydrate stability zone. Methane gas shall be introduced into the top of the vessel through a mass flow controller operating at a prescribed (slow) rate. Seawater shall be allowed to leave from the bottom of the column using a high-pressure syringe pump operating at constant pressure mode. Although this geometry is inverted compared to natural systems, it results in a better-controlled gas front which is very important for the measurements to be made. Temperatures, pressures, resistances shall be recorded frequently (~ every 30 sec) and ultrasonic (P wave) data shall be collected by hand regularly (~daily). At the conclusion of the test (salt front breakthrough significantly advanced through the column), the vessel shall be rescanned and hydrate dissociated while observing using CT. Gas mass flow, temperatures, and pressures shall be recorded over the dissociation to determine hydrate location, saturation, and to characterize the advancement of the reaction front.

B1.2. Activities Phase 2:
B1.2.1 Summary

Over the course of Phase 2 of the project we have addressed Milestones 1.E and 2.D through the following activities related to Task 6. 1) The design and construction of an operational experimental setup for running hydrate formation experiments at the University of Texas at Austin (UT). 2) The execution of 5 successful hydrate formation front experiments and 2 hydrate dissociation experiments between UT and Lawrence Berkeley National Laboratory (LBNL). 3) The analysis of the data from these experiments to improve our understanding of the distribution and saturation of the brine, hydrate, and gas phases within the samples.

Due to the challenging nature of the hydrate formation experiments required to complete Task 6, we decided previously (Flemings, 2014a) that it would be prudent to assemble an additional hydrate formation vessel at UT to increase our productivity. The most recent iteration of the hydrate formation equipment setup at UT is discussed in detail below, in section B1.2.2. This setup has been continuously revised as we have determined way to improve our experimental execution.

The parameters of the successful hydrate formation experiments are described in Table 3. The purpose of each of these experiments was to form hydrate to three-phase equilibrium conditions through the induction of a propagating gas front into a brine-saturated sample. From these experiments we determined that: A) the degree of subcooling is an important control on the induction time, B) hydrate formation is rate-limited, and C) lowering the gas flow rate reduces the rate-limitation on hydrate formation. Through these experiments we demonstrated a successful reaction transport front with hydrate formation near three-phase equilibrium.

B1.2.2 UT Hydrate Lab Equipment

As it currently stands, the synthetic hydrate formation lab at UT consists of the following major components: the hydrate formation vessel and cooling jacket, the vertical hanger frame, the 3 Teledyne ISCO 500D syringe pumps, the circulating refrigeration unit (CRU), and data acquisition system (DAQ), and the temperature control box (TCB). The pumps and TCB were purchased and assembled over the course of Phase 2 as we determined they were required for experimentation. We also collaborated with

Dr. David DiCarlo at the UT Petroleum and Geosystem Engineering Department (PGE) to perform one test (HVT0005) in the computer tomography (CT) lab and collect CT data during the experiment.

The hydrate formation vessel (Figure 21) is constructed with steel endcaps and a CT-transparent aluminum wall. It was designed to be similar to the vessel at LBNL, but rated to a maximum pressure of 2500psi (maximum working pressure of 2200psi). Aluminum sleeve is contained within a PVC cooling jacket that allows the CRU to maintain a constant confining temperature to ±0.1℃. The vessel can be hanged vertically using a compression hanger collar (Figure 22) and the aluminum hanger frame (Figure 23).The three syringe pumps separately control the pressure and flow of the confining, brine, and methane fluids during the experiment to an accuracy of ±1psi and 0.001mL/min, respectively. The vessel, hanger, and pumps are all contained within the TCB, which maintains a constant temperature of up to 5.5 ± 0.1℃ above the surrounding room temperature (Figure 23 and 24). Temperature is measured at the top and bottom of the confining cell as well as inside and outside the TCB. Confining, inlet, and outlet pressures are dually measured by transducers attached to each pump as well as by separate transducers built into the fluid lines. The pressure and temperature data are recorded automatically at a set interval by the DAQ.

Each sample consisted of a homogeneously-packed fine sand in a cylindrical sleeve to a 2" diameter and approximately 5" length. The sleeve was made of fluid impermeable Viton to separate the pore and confining fluids while allowing for the confining stress to translate to the sample. The sample was confined on top and bottom with two Delrin endcaps, each of which had a fluid port (Figure 25).

B1.2.3 HVT0001

B1.2.3a Introduction

This experiment was done in LBNL to examine methane hydrate formation under three phase (gas/brine/hydrate) conditions, followed by thermal dissociation from the bottom. In this test, a vertically oriented cylindrical sand sample saturated with 7% NaCl brine was drained at 1014 psia and 4C, with the brine replaced by methane. These conditions are within the methane hydrate stability zone, and hydrate formation was expected. The test was monitored using multiple pressure and temperature sensors, and X-ray computed tomography (CT) was used to assess phase saturations. When drainage proceeded to the point where the methane gas approached the sample bottom, the connection to the gas was closed, and brine was allowed to imbibe into the sample under constant pressure. Upon completion of imbibition, the hydrate was dissociated by warming, using system designed to heat the sample from the bottom.

B1.2.3b Methods

Sample Instrumentation

A lightweight 1/16" garolite rod was assembled with four Type T thermocouple probes (Omega Engineering, Stamford CT) and 2 silver/silver chloride electrodes. This rod was attached to a 1/8 inch stainless steel tube, and the thermocouple probes and wires from the electrodes were sealed with epoxy in the tube. The tube was run concentrically through a ¼ inch stainless steel tube that connects to

the bottom 2-inch diameter endcap (Figure 26a). A 2-inch inner diameter EPDM sleeve was attached to the endcap with a double wrap of wire forming the base and sides of the cylindrical sample.

Sample

White quartz sand (Sigma Aldrich) (50 to 70 mesh ~ 212 – 300 micron grain size sand properties) was poured into the EPDM sleeve preassembled onto the PVC endcap partially filled with 7% NaCl brine. The sand was slowly poured to reduce air entrainment, and the assembly was vibrated constantly during the pour to minimize pore space. When the appropriate quantity of sand had been poured into the sleeve, the top endcap containing a Type T thermocouple (Omega Engineering, Stamford CT) was emplaced and a double wrap of wire was placed around the sleeve at the top endcap. The temperature outside the sleeve was monitored with another Type T thermocouple attached to the sleeve with electrical tape, shown schematically in Figure 26b, and an X-ray scan is presented in Figure 26c.

Sample Assembly

The sample assembly was installed into a pressure vessel containing a confining fluid of 50% propylene glycol 50% water separated from the sample by the EPDM jacket and the endcaps. The pressure vessel was contained in a thermal jacket through which temperature-controlled water/propylene glycol was flowed (Figure 27). The pressure vessel assembly was mounted to a frame that held it in the vertical orientation under normal operation, but allowed it to be rotated into the horizontal orientation for brief periods for X-ray CT scanning. The frame was mounted to the moving table of the X-ray CT scanner to minimize alignment errors on ongoing sets of CT scans.

The confining fluid region outside of the sample was connected to an Isco 500D syringe pump to allow constant confining pressure control. The fluid inlet and outlet to the sample were also connected to Isco 500D syringe pumps, with the downstream pump connected to the sample bottom (when oriented vertically) containing 7% NaCl brine, and the upstream pump connected to the sample top containing methane. The pumps were exposed to room temperature in a temperature-controlled laboratory. The tubing within the vessel was initially filled with brine.

Temperature measurements at 7 locations and pressure measurements at 4 locations were recorded every 20 seconds during the test (Figure 28a). Thirty-five multi-energy (80, 100, 120, and 140 kV) sets of CT scans were collected (an example is as shown in Figure 32) to document the status of the sample. Each set of scans required adjusting the orientation of the custom-built sample holder, and each set of scans was performed at 80, 100, 120, and 140 kV energies.

B1.2.3c Test Sequence

 The test was performed in three stages: 1) brine drainage under hydrate-stable conditions (4°C and 1010 psi), 2) brine imbibition under hydrate-stable conditions (4°C and 1010 psi), and 3) hydrate dissociation by warming from the bottom. Each stage will be described separately. Temperatures, pressures, and fluid volumes, and sample mass computed from CT data for these stages are shown in Figure 28.

Drainage (0 – 92.4 hours)

The sample temperature was set nominally to 4°C. As shown in Figures 28a and 28b, a temperature gradient formed in the sample, with warmer temperatures at the top of the sample. The magnitude of the temperature difference between the sample top and bottom was about 0.3°C during the drainage and imbibition. This temperature gradient was largely unaltered when the sample orientation was changed for CT scanning. The sample was drained at a rate of 0.003 mL/min while methane gas was supplied to the top of the sample at 1010 psi. This drainage rate yields a Darcy velocity of 2.13 mm/day (0.089 mm/hr). This drainage rate was maintained for the first 92.4 hours, after which it was determined by X-ray CT scanning that the invading methane gas phase was approaching the sample bottom, however all still completely contained in the sample. At this time, the valve allowing the methane gas to enter the sample was closed, and the brine pump that was previously withdrawing the brine at the constant rate was set to run at a constant pressure equal to 1010 psi. Methane hydrate formation would consume gas from the gas phase, allowing brine to imbibe.

Hydrate formation is indicated by concomitant increase in temperature and consumption of gas. Figure 29 shows temperature differences between locations in the sample and system over this time period to make comparisons easier. These locations include thermocouple locations in the sample (compared to the lowest thermocouple location) and either the temperature indicated by the lowest elevation thermocouple, outside the sleeve, or the temperature bath to examine environmental influences on the system and thermal driving forces. Two periods of probable hydrate formation are indicated as periods 1 and 2 in Figure 29, where temperature increases at the upper thermocouples exceeded those at the lower thermocouples. Two periods where the temperatures at the upper thermocouples decline also occur following the temperature increases. The temperature of the lower thermocouple reflects the temperature at the bottom of the sample. Little change would be expected at that location because drainage was not significant there (no gas/brine contact to induce hydrate formation). Temperature data show only mild temperature signals for hydrate formation because the salinity was high and rate of drainage was so slow resulting in the rate of heat-generating hydrate formation being low relative to the ability of the system to transfer heat to the bath.

Imbibition (92.4 hours – 546 hours)

Imbibition was performed by allowing brine to imbibe into the sample bottom at constant pressure (1010 psi). Brine then could fill the pore space as methane was consumed by hydrate formation. Over one period of about 100 hours, the imbibition was halted by shutting the valve allowing brine to reenter the vessel, and sample (shut in from both gas and brine) was allowed to equilibrate. Over that period, the pressure in the sample dropped to about 860 psia. Upon reopening the valve, the pressure was restabilized to 1010 psi and imbibition continued.

Imbibition, indicating methane consumption, continued over the imbibition duration with an initial rapid rate that slowed to a near zero rate while the system was shut in (233-329 hours) and increased again when imbibition was restarted, and then tailed to a very low rate at about 550 hours (see green line in Figure 28c.) These differences in fluid volumes indicate that methane was being consumed by hydrate formation over this time. Temperatures remained fairly constant over the imbibition showing no obvious indication of hydrate formation (Figures 28a and 30), with the exception of the temperature

spike of several tenths of a degree lasting about 1.5 hours when brine was allowed to flow into the sample following the shut in period. Approximately 5 mL of brine imbibed over that time.

Dissociation (546 hours to 750 hours)

Hydrate was dissociated over the final 250 hours of the test by stepwise increasing the temperature of a heating coil situated at the base of the sample. Over this time period, the brine pump remained shut in, allowing fluids (gas + water) produced by methane hydrate dissociation to flow into the gas pump, which was maintained at a constant pressure of 1010 psia. Heating the coil in the bottom of the pressure vessel was accomplished by flowing temperature-controlled water through the tube using a separate controller from that used for overall temperature control.

Temperature differences over the dissociation are shown in Figure 31, and gas production is shown as decreasing values on the black and green curves in Figure 28c over this time period. At about 660 hours, the thermal gradient in the sample was reversed from top-warm to neutral, and then to bottom-warm at about 690 hours. Hydrate dissociation and gas production were minimal until that point. This bottom warm condition remained until about 720 hours when the sample became top-warm again. The lion share of the hydrate had dissociated by this time as well, although some gas production continued past 750 hours.

CT Data

CT images presented in Figure 32 show changes in density from the starting condition and proceed over the course of the experiment. In these images, replacing the brine-saturated sand with either partially gas-saturated or hydrate-saturated sand will result in a decrease in density (shown in red). Increases in density, perhaps from brine concentration or most likely indicating a slight misalignment when subtracting two data sets are indicated in blue. The "internal standard slice" is also present in these images about one third down, and can be ignored. In the top row, the decrease in density is shown by the increasing red color showing the drainage process including gas replacing brine and hydrate formation. In the middle row, the red color is mitigated by imbibition of brine. Towards the end of this phase, a large amount of the previously red volume has become mostly resaturated with brine and residual hydrate. Upon hydrate dissociation however, it is clear that hydrate was present low in the sample because gas evolved from hydrate dissociation again reduces the density (more red color).

B1.2.3a Analysis

 There should be leakage in the brine pump according to the brine pump volume data. The brine pump was closed between 233.0667 and 329.4 hours. During this time, the volume in the brine pump decreased by 0.74 ml. These data yielded a leakage rate of 0.0078 ml/hour. During the brine drainage and hydrate formation period, the volume in the brine pump increased from 250.8 ml at 1.4333 hour to 267.17 ml at 92.4 hour. This yielded a brine withdraw rate of 0.1800 ml/hour. The corrected brine withdraw rate should be 0.1878 ml/hour (=0.0078+0.1800 ml/hour) when the leakage rate was considered. The diameter of the sample is 2 inches or 5.08 cm. Therefore, the water flow rate at the downstream end of the sample is 2.57e-8 m/sec.

With the sample pressure of 6.96 MPa, temperature of 4 °C, initial salinity of 7 wt.% (NaCl), and brine withdraw rate of 2.57e-8 m/sec, we can predict the saturations, the hydrate solidification front velocity, and the gas consumption rate in Table 5. We compare the gas consumptions measured in the first period of the experiment with prediction from the MOC analytical solution (Figure 33). There is clearly a significant amount of induction time at the beginning when the measured gas consumption follows the 1:1 ratio of gas to brine volume (Figure 28: the blue line follows the red line for brine volume less than 6 ml). After that, the measured gas consumption increases with a greater rate. However, the measured gas consumption is still lower than the prediction from the MOC solution, which means the hydrate system does not reach three-phase equilibrium. This is consistent with the fact that the volume in the brine pump keeps decreasing in the imbibition period (red line in Figure 28c).

B1.2.4 HVT0004

B.1.2.4a Experimental Setup

The sample was packed using slow pluvation, had a final length of 5.125", and was vacuum saturated with a 7 wt% NaBr brine. The porosity was gravimetrically calculated to be 0.393 (Table 4). The level of sample saturation was qualitatively assessed by increasing the confining fluid pressure and recording the pore pressure response. The b-value (b = P_{pore} / P_{conf}) was greater than 0.95, indicating a very well saturated sample. Once the system reached temperature and pressure equilibrium at experimental conditions, the methane pump was set to a constant pressure of 1775 psi and the brine pump was set to a constant outflow of 0.003 mL/min (0.18 mL/hr). This experiment did not have a shut-in phase and it is likely that, after 57 hours, gas was flowing out of the sample, which rendered mass balance impossible. Therefore, we only analyze data from the first 57 hours here.

B.1.2.4a Data Collection

In this experiment, the volumes of gas and brine in the pumps was recorded by hand at 30-minute to 14-hour intervals and the confining, outlet, and inlet pressures and confining, coolant, and room temperatures were recorded at a 5-second interval by the DAQ.

B.1.2.4a Analysis

Gas Consumption Analysis

We compared the gas consumption during this and the following experiments to three end-member cases (Figure 34): 1) The gas consumption assuming no hydrate formation (dashed line), representing the minimum potential gas consumption, 2) The gas consumption assuming S_h = 1 behind the hydrate formation front (dot-dashed line), representing in the maximum potential gas consumption, and 3) The Methods of Characteristics (MOC)-predicted gas consumption (solid black line) at the experimental conditions (Flemings, 2015) representing the expected gas consumption for this experiment. Cases 1 and 2 calculate the gas consumption from equations 36 and 37, respectively:

$$V_g = V_b \hspace{9cm} \text{Eq 36}$$

$$V_g = \left[\frac{L_f}{L} \cdot V_{TOT} \cdot \phi\right] \cdot \left[\frac{\rho_h \cdot M_g}{M_h \cdot \rho_g}\right] \hspace{5cm} \text{Eq 37}$$

Where L is the length of the sample, L_f is the length of the hydrate formation zone (HFZ), V_{TOT} is the total sample volume, ρ_h and ρ_g are the densities of hydrate (0.912 g/cm³) and methane gas (0.111 g/cm³) phases, respectively, and M_h and M_g are the molecular masses of hydrate (119.655 g/mol) and methane gas (16.04 g/mol), respectively.

Figure 35 shows the gas consumption during HVT0004 experiment compared to three end member consumption models. Gas was consumed at a relatively constant rate of 0.32mL/hour, which is 49 percent of the consumption rate predict by the MOC solution. In total, 18mL of methane were consumed during the drainage phase, which was far below the MOC-predicted gas consumption. These results indicate that hydrate was not forming to three-phase equilibrium behind the front.

Bulk Phase Saturations from Mass Balance

We derived a set of mass balance equations (Appendix A), using the mass of water withdrawn and gas consumed (You et al., 2014), to calculate the bulk saturation of each phase (brine, hydrate, and methane) behind the hydrate formation front throughout each experiment. We began with the following set of mass balance equations (Eqs. 38 – 40):

$$\Delta W = V_{TOT}\phi\rho_W \cdot \Delta S_W + \frac{V_{TOT}\phi\rho_H N M_W}{M_H} \cdot \Delta S_H \hspace{3cm} \text{Eq 38}$$

$$\Delta M = V_{TOT}\phi\rho_G \cdot \Delta S_G + \frac{V_{TOT}\phi\rho_H M_G}{M_H} \cdot \Delta S_H \hspace{3cm} \text{Eq 39}$$

$$0 = \Delta S_G + \Delta S_H + \Delta S_W \hspace{6cm} \text{Eq 40}$$

Where, ΔS_W, ΔS_H, and ΔS_G are the changes in saturation in the water, hydrate, and gas phases, respectively; ΔM and ΔW are the changes in methane and water masses in the pumps, respectively, ρ_g, ρ_h, and ρ_W are the density of the gas (0.111 g/cm³), hydrate (0.912 g/cm³), and brine (1.037 g/cm³) phases, respectively, M_g, M_h, and M_W are the molecular masses of methane (16.04 g/mol), hydrate (119.655 g/mol), and water (18.02 g/mol), respectively, and N is the hydration number for Structure I methane hydrate (N = 5.75). Assuming that all the gas was either consumed by hydrate or was in the free gas phase, we derived Eqs. 41 – 43, from Eqs. 38 – 40:

$$\Delta S_G = \frac{\left[\left(\frac{V_{TOT}\phi\rho_H M_G}{M_H} \cdot \Delta W\right) + \left(\left(V_{TOT}\phi\rho_W - \frac{V_{TOT}\phi\rho_H N M_W}{M_H}\right) \cdot \Delta M\right)\right]}{\left[\left(V_{TOT}\phi\rho_W \cdot \left(V_{TOT}\phi\rho_G - \frac{V_{TOT}\phi\rho_H M_G}{M_H}\right)\right) - \left(\frac{V_{TOT}\phi\rho_H N M_W}{M_H} \cdot V_{TOT}\phi\rho_G\right)\right]} \hspace{1cm} \text{Eq 41}$$

$$\Delta S_W = \frac{\left[\left(\Delta S_G \cdot \left(V_{TOT}\phi\rho_G - \frac{V_{TOT}\phi\rho_H M_G}{M_H}\right)\right) - \Delta M\right]}{\frac{V_{TOT}\phi\rho_H M_G}{M_H}} \hspace{3cm} \text{Eq 42}$$

$$\Delta S_H = -(\Delta S_G + \Delta S_W) \hspace{6cm} \text{Eq 43}$$

Using these mass balance equations, we calculated the correct bulk hydrate, gas, and brine phase

saturations behind the front during the drainage phase of HVT0004, compared to the predicted hydrate saturation required for three-phase equilibrium (Figure 36). The hydrate, brine, and gas saturations are approximately 0.18, 0.6, and 0.21, respectively. These results indicate that hydrate did not form at three-phase equilibrium as the front progresses through the sample.

B.1.2.4a Conclusions

The gas consumption data indicated that the hydrate formation rate was lower than the MOC-predicted rate. The mass balance-derived bulk hydrate saturation was lower than the predicted saturation from three-phase equilibrium. The results suggest that the hydrate in the sample is not at three-phase equilibrium and that hydrate formation is rate-limited.

B1.2.5 HVT0005

B.1.2.5a Experiment Setup

The sample was packed using slow pluvation, had a final length of 5.125", and was vacuum saturated with a 7 wt% NaBr brine. The porosity was gravimetrically calculated to be 0.383 (Table 4). The level of sample saturation was qualitatively assessed by increasing the confining fluid pressure and recording the pore pressure response. The b-value was greater than 0.95, indicating a very well saturated sample. Once the system reached temperature and pressure equilibrium at experimental conditions, the methane pump was set to a constant pressure of 1775 psi and the brine pump was set to a constant outflow of 0.003 mL/min (0.18 mL/hr). After 57 hours, we stopped the brine pump, because gas was entering the outlet tube, which would cause errors in the mass balance, and let the sample sit for an additional 180 hours.

B.1.2.5b Data collection

In this experiment, the volumes of gas and brine in the pumps was recorded by hand at 30-minute to 14-hour intervals and the confining, outlet, and inlet pressures and confining, coolant, and room temperatures were recorded at a 5-second interval by the DAQ. Finally, while remaining in the vertical position, CT scans were taken at high (130 keV) and low (100 keV) energies throughout the experiment to quantitatively assess the distribution and saturation of the water, hydrate, and gas phases within the sample. Each CT scan consisted of 26 slices taken at 0.5cm spacing and a beam thickness of 1cm. Each slice consisted of a 512x512 matrix of attenuation values in Hounsfield units that included attenuation data from the material outside the sample. The slices were filtered to include only the pixel inside the sample, resulting in a 213x213 matrix where all cells external to the sample are occupied by zeros. From these processed slices, an average attenuation for the slice was calculated by summing all the attenuations in the slice and dividing it by the number of cells in the sample (approx. 35300 cells).

B.1.2.5d Analysis

Mass Balance

Figure 37 shows the gas consumption during the experiment compared to three end member consumption models. In total, 27 mL of methane were consumed during the experiment, which ended

just above the gas consumption predicted by the MOC solution for hydrate formation. During the brine withdrawal phase (0 – 57 hours), gas was consumed at a relatively constant rate of 0.28mL/hour, which is 43 percent of the consumption rate predict by the MOC solution. After the brine pump was shut off, gas consumption continued, but at a greatly reduced average rate of 0.06 mL/hr. It also appears that, during this period (57 – 240 hours), the rate of gas consumption decreased over time as the total gas consumption approached the value predicted by the MOC model.

Using the previously derived mass balance equation (Appendix A), we calculated the correct bulk hydrate, gas, and brine phase saturations behind the front throughout the experiment, compared to the predicted hydrate saturation required for three-phase equilibrium (Figure 38). The hydrate, brine, and gas saturations are approximately 0.15, 0.6, and 0.25, respectively, during the drainage phase of the experiment. After the brine pump is stopped, these values increase to 0.39, 0.48, and 0.13, respectively, by the end of the experiment. These results indicate that hydrate did not form at three-phase equilibrium as the front progresses through the sample.

CT-Derived Bulk Density

Figures 39 and 40 shows slice montages from the initial, brine-saturated core and of the sample at the end of the experiment, respectively. Darker regions are interpreted to be lower density, indicating the presence of hydrate and/or free gas in the core. These images show a low density region forming near the inlet of the sample. This region develops slowing over the course of the experiment and suggests the propagation of a hydrate formation front away from the inlet as the experiment progresses.

We calculate the bulk density profile of the sample using the CT data by assuming the CT-value to be directly proportional to the scanned bulk density. Since the solid mass is not changing (assuming no grain movement), then any change in bulk density is due to changes in the phases occupying the pore space. To perform this analysis, we initially collected calibration scans of a gas- and brine-saturated sample. The average attenuations for each slice in these scans were used as endpoint calibration values. The attenuations from the dry scan (CT_{dry}) were assumed to be the lowest expected attenuation, while those from the saturated scan (CT_{wet}) represented the highest expected attenuation. The attenuation values collected throughout the experiment (CT_{exp}) were then used, in combination with the endpoint values, to linearly interpolate (Eq. 44) between the dry (ρ_b^{dry}) and wet (ρ_b^{wet}) bulk density values to determine the experimental bulk density (ρ_b^{exp}).

$$\rho_b^{exp} = \left[\rho_b^{dry} + \left(\left(\rho_b^{wet} - \rho_b^{dry} \right) \cdot \left(\frac{(CT_{exp} - CT_{dry})}{(CT_{wet} - CT_{dry})} \right) \right) \right] \qquad \text{Eq 44}$$

The CT attenuation values are averaged across the entire slice to reduce the chance of anomalies resulting in non-physical saturations. The dry and wet bulk density of the sample was calculated to be 2.03 g/cm^3 and 1.67 g/cm^3, respectively, using the standard density equation (Eqs. 45 and 46) and knowledge of the porosity of the sample and density of the sediment (ρ_s), brine, and gas:

$$\rho_b^{dry} = \left((1 - \phi) \cdot \rho_s\right) + \left(\phi \cdot \rho_g\right) \hspace{6cm} \text{Eq 45}$$

$$\rho_b^{wet} = \left((1 - \phi) \cdot \rho_s\right) + \left(\phi \cdot \rho_w\right) \hspace{6cm} \text{Eq 46}$$

Figure 41 shows a combined analysis of the CT images and CT-derived bulk density for HVT0005 at the end of the drainage phase (blue line) and shut-in phase (red line). At the end of the drainage phase, we interpret three zones to be present: 1) hydrate formation zone (HFZ) (0 – 5.5 cm); 2) gas invasion zone (5.5 – 9.5 cm) (GIZ); and 3) a water saturated zone (9.5 – 12 cm) (WSZ). The CT images show that there is a large decrease in density near the inlet (0 – 1.75cm). We attribute this to the presence of a high gas saturation in this region. The uniform drop in density in the rest of the HFZ suggests a relatively uniform gas and hydrate saturation in the hydrate formation zone. In the HFZ, the experimental hydrate saturation is interpreted as be approximately 0.2 according to the mass balance results. In the GIZ, the density increases back to nearly initial values. In this region, there is likely some hydrate present, however the density gradient is likely due to a decrease in gas saturation further from the inlet. In the WSZ, densities are approximately equal to the initial value and this is interpreted to be brine-saturated with no free gas or hydrate present. At the end of the experiment, the bulk density within the HFZ and GIZ have increased, due to the additional formation of hydrate and consumption of gas.

CT-Derived Bulk Phase Saturations

We derived a set of equations to calculate the phase saturation profiles (Appendix B) throughout the experiment similar to those presented in Seol and Kneafsey, 2011 and You, K., et al., 2014. The derivation begins with Equation 47, which defines our experimental bulk density as a function of the porosity, grain and phase density, and phase saturations and Equation 48, which defines the fraction of the pore space that is occupied by each phase:

$$\rho_b^{exp} = \left((1 - \phi) \cdot \rho_s\right) + \left(S_W \cdot \phi \cdot \rho_W\right) + \left(S_G \cdot \phi \cdot \rho_G\right) + \left(S_H \cdot \phi \cdot \rho_H\right) \hspace{2cm} \text{Eq 47}$$

$$S_W + S_H + S_G = 1 \hspace{8cm} \text{Eq 48}$$

The saturation (S_g, S_H, and S_w) are unknown. To continue the derivation, we make the following critical assumptions: 1) Gas density is negligible, 2) brine density remains constant, C) the solid grains in the sample do not move, and 3) hydrate only forms within HFZ. With these assumptions, equations 49 – 51 are derived to solve for the phase saturations:

$$S_W = \frac{S_T}{\left(1 + \frac{Xf}{(1-X-Y)}\right)} \qquad \text{Eq 49}$$

$$S_H = \left[\frac{S_T}{\left(1 + \frac{(1-X-Y)}{Xf}\right)}\right] \cdot \left[\frac{\rho_w}{\rho_h}\right] \qquad \text{Eq 50}$$

$$S_G = 1 - S_W - S_H \qquad \text{Eq 51}$$

Where S_T is the total saturation, X is the fraction of the initial water converted into hydrate, Y is the fraction of initial water removed from the sample, and f is the mass ratio of hydrate to water in hydrate, equal to 1.15. These values are defined by equations 52 – 54:

$$S_T = \left(\frac{\rho_b^{exp} - \rho_b^{dry}}{\rho_b^{wet} - \rho_b^{dry}}\right) \qquad \text{Eq 52}$$

$$X = (\Delta V_m - \Delta V_w) \cdot \frac{M_w \cdot N \cdot \rho_H}{V_{pore} \cdot \rho_w \cdot (1-C) \cdot M_H} \cdot \frac{L_{HFZ}}{L} \qquad \text{Eq 53}$$

$$Y = \frac{\Delta V_w \cdot \rho_w}{V_{pore} \cdot \rho_w} \cdot \frac{L_{HFZ}}{L} \qquad \text{Eq 54}$$

Where ΔV_m and ΔV_w are the changes in volume in the methane and brine pumps, respectively, V_{pore} is the pore volume ($V_{pore} = V_{TOT} \cdot \phi$), C is the initial salinity in weight percent, L is the total sample length, and L_{HFZ} is the length of the HFZ. X and Y are corrected for the location of the hydrate formation using the ratio between L and L_{HFZ}.

The denominator of equations 49 and 50 weights the total saturation by the fraction of the total change in water mass in the sample that is due to hydrate formation. As more hydrate formed the denominator in equation 49 increases, reducing S_W while the denominator of equation 50 decreases, showing greater values for S_H. For slices taken beyond the extent of the HFZ, X and Y are assumed to equal zero, which forces $S_H = 0$, $S_W = S_T$, and $S_G = 1 - S_W$, such that any changes in density from the initial are due to gas invasion. For the analysis of this experiment, we assumed that there was no GIZ and that the HFZ extended from 0 – 8cm.

During the brine withdrawal phase (0 – 57 hours) in HVT0005, the CT-derived hydrate saturation profiles (Figure 42B) indicate that hydrate continuously forms throughout the HFZ, which was assumed to be between 0 – 8cm and was confirmed through CT scan images. The rate of hydrate formation increases later in the experiment, but the overall saturation within the HFZ is essentially uniform, ranging from 0.12 – 0.15. The CT-derived gas saturation profiles (Figure 42C) directly mirror the observed changes in density, showing regions with large density decreases as having a greater gas saturation. As the methane is the lowest density phase in the system, the gas saturation will logically be the greatest

controlling factor on changes in density. The water saturation profiles (Figure 42D) show the largest decrease in water saturation near the inlet, where the gas saturation is the largest, a constant, uniform decrease in water saturation from 2 – 8cm, and very little drop in water saturation from 8 – 13cm.

After the brine pump was shut off and the outlet valve was closed in HVT0005 (57 – 172 hours), the bulk density profiles (Figure 43A) indicated the development of three distinct zones within the sample. Zone 1 extends from 0 – 3.75cm and the density continues to decrease over time, reaching a minimum density of 1.92 g/cm^3 near the inlet. Zone 2 extends from 3.75 – 8.25cm and is characterized by a rebound in bulk density back to near initial values, with a final range from 1.99 – 2.03 g/cm^3. Zone 3 extends from 8.75 – 13cm and is the only portion of the sample where the density increases above the initial value, reaching a max density of 2.045 g/cm^3.

The hydrate saturation profiles (Figure 43B) indicate that, after the brine pump was stopped, hydrate begins forming at a more rapid rate within Zone 2, relative to Zone 1, reaching a maximum saturation of 0.35. The overall rate of hydrate formation all appears to decrease over time, indicated by the change in saturation between time steps. The gas saturation profiles (Figure 43C) again mirrors the bulk density profiles, with a maximum gas saturation of 0.31 near the inlet and decreasing across the core. The water saturation profiles (Figure 43D) show an overall decrease in water saturation within in Zones 1 and 2, with a larger decrease in Zone 1.

The CT-derived saturations are lower than those calculated from the mass balance. This is likely due to the assumption that the HFZ extends from 0 – 8cm, which is 2.5 cm further down the core than predicted by the model. Regardless of this, however, these results suggest that hydrate front is not stable and does not form to three-phase equilibrium as the front progresses down the sample.

B.1.2.5d Conclusions

The mass balance results show that hydrate forms at a saturation far below the predicted three-phase saturation during the drainage phase and then continues to form after the brine pump is stopped. The CT-derived bulk density data indicates that there is a gas front that is moving ahead of the predicted hydrate formation front during the drainage phase and that hydrate continues to form in both the HFZ and GIZ during the shut-in phase. The CT-derived phase saturation data show uniform hydrate formation throughout the assumed HFZ during the drainage phase. Additional hydrate forms within the HFZ during the shut-in phase, with formation concentrated in Zone 1. These results suggest that hydrate formation is not homogeneous within the sample and that the hydrate is not forming to three-phase equilibrium within the HFZ.

B1.2.7 HVT0007

B1.2.7a Experimental Setup

The sample was packed using slow pluvation, had a final length of 5.125", and was vacuum saturated with a 7 wt% NaBr brine. The porosity was gravimetrically calculated to be 0.393 (Table 4). The level of sample saturation was qualitatively assessed by increasing the confining fluid pressure and recording the pore pressure response. The b-value was greater than 0.95, indicating a very well saturated sample. Once the system reached temperature and pressure equilibrium at experimental conditions, the

methane pump was set to a constant pressure of 1775 psi and the brine pump was set to a constant outflow of 0.003 mL/min (0.18 mL/hr). After 57 hours, we stopped the brine pump to match the execution of HVT0005.

B1.2.7b Data Collection

In this experiment, the gas, brine, and confining volume and inlet, outlet, and confining pressure data, from both the pumps and inline transducers, were recorded at set intervals throughout the experiment by the DAQ system. Data was initially recorded every 10 seconds and was increased in several increments to 2 minutes by the end of the experiment. Although the shorter interval was nice near the beginning of the experiment to confirm in real time that the experiment was running properly, we determined that it was recording an unnecessary amount of data after the first few hours.

B1.2.7c Analysis

Figure 44 shows the gas consumption over the course of the experiment (pink line) compared to the three end member consumptions models. In total, 31 mL of methane were consumed during the experiment, which ended just above the gas consumption predicted by the MOC solution for hydrate formation. During the brine withdrawal phase (0 – 57 hours), gas was consumed at a relatively constant rate of 0.32mL/hour, which is 50 percent of the consumption rate predict by the MOC solution. After the brine pump was shut off, gas consumption continued, but at a greatly reduced average rate of 0.15 mL/hr. It also appears that, during this period (57 – 144 hours), the rate of gas consumption decreased over time as the total gas consumption approached the value predicted by the MOC model.

Figure 45 shows the bulk hydrate, water and gas phase saturations throughout the experiment calculated from mass balance equations dependent on the volumes of brine withdrawn and gas consumed. The bulk hydrate, water, and gas saturations reach final values of 0.24, 0.56, and 0.20, respectively. After the brine pump was stopped, these values continue to change to a final saturation of 0.62, 0.27, and 0.11, respectively. These results indicate that hydrate did not form at three-phase equilibrium as the front progresses through the sample.

B1.2.7d Conclusions

The gas consumption data indicated a hydrate formation rate below the MOC-predicted rate and showed continued hydrate formation after the brine pump was shut-in. The bulk phase saturations showed a hydrate saturation far below the three-phase equilibrium saturation during the drainage phase that increased during the shut-in phase. These result suggest that hydrate formation is rate limited and that the hydrate in this experiment did not form at three-phase equilibrium.

B1.2.8 HVT0008

B1.2.8a Experimental Setup

The sample was packed using slow pluvation, had a final length of 4.875", and was vacuum saturated with a 7 wt% NaBr brine. The porosity was gravimetrically calculated to be 0.377 (Table 4). The level of sample saturation was qualitatively assessed by increasing the confining fluid pressure and recording the pore pressure response. The b-value was greater than 0.95, indicating a very well saturated sample.

Once the system reached temperature and pressure equilibrium at experimental conditions, the methane pump was set to a constant pressure of 1775 psi and the brine pump was set to a constant outflow of 0.001 mL/min (0.06 mL/hr). After 57 hours, we stopped the brine pump to match the execution of HVT0005 and HVT0007.

B1.2.8b Data Collection

Data collection for this experiment followed the same procedures as HVT0007.

B1.2.8c Analysis

Figure 46 shows this data for HVT0008 during the drainage (0 – 171 hours) and shut-in (171 – 186 hours) phases. During the drainage phase of HVT0008, gas was consumed at 80 percent of MOC-predicted rate. During the shut-in phase, gas was continuously consumed, reaching 91 percent of the MOC-predicted gas consumption, indicating further hydrate formation and suggesting that the system was not at bulk thermodynamic equilibrium behind the formation front.

Figure 47 shows the mass balance-derived bulk water (blue line), gas (red line), and hydrate (green line) phase saturation behind the formation front during the first 17 hours of the experiment (Figure 47A) and over the entire experiment (Figure 47B). These phase saturations are compared to the predicted three-phase equilibrium hydrate saturation (S_h = 0.76) according the MOC solution and used to interpret three periods with distinct hydrate formation behavior. Period 1 (0 – 1 hours) shows little to no hydrate formation, followed by dramatic hydrate formation at the beginning of Period 2 (Figure 47A). We interpret this period to represent the induction time for the experiment.

In Period 2 (1 – 17 hours), following the rapid formation of hydrate to a saturation of approximately 0.65, the hydrate saturation drops to 0.21 at a decreasing rate (Figure 47A). We interpret that this is due to a hydrate formation rate that is lower than predicted due to a small number of nucleation sites behind the front. Over the course of Period 2, the number of nucleation sites grows, which increases the hydrate formation rate until, at 17 hours, the formation rate matches the predicted rate.

In Period 3 (17 – 186 hours), the bulk hydrate saturation increases steadily from 0.31 to 0.67 (Figure 47B), which is 87 percent of the predicted three-phase equilibrium saturation for these experimental conditions. We interpret that, during this period, the hydrate formation rate is greater than the predicted, because additional nucleation sites over time continue to increase the formation rate. This is also possible, because the system is not at bulk three-phase equilibrium and, therefore, hydrate formation is not limited by thermodynamics.

B1.2.8d Conclusions

A detailed analysis of the phase saturation data indicates that this experiment had an induction time of only 1 hour and that over the course of the experiment the hydrate formation rate continued to increase. This is potentially due to an increase number of nucleation sites behind the front. The total experimental gas consumption is lower than the predicted, the hydrate saturation during the drainage phase is always below the modeled three-phase saturation and increases during the shut-in phase.

Therefore, despite the high hydrate formation rate, these results suggest that hydrate formation is rate-limited and that the hydrate in our sample did not form to three-phase equilibrium.

B1.2.9 UT Experiment Comparison

Figure 48 shows the gas consumption data from the drainage phase of all four experiments we have run successfully at UT Austin: HVT0004 (blue line), HVT0005 (green line), HVT0007 (pink line), and HVT0008 (orange line) compared to the three end member solutions. Other than small variations in the sample porosity, the only variable parameter between these experiments is the flow rate (Table 4). The high flow rate experiments (HVT0004, HVT0005, and HVT0007) show a repeatable, rate-limited hydrate formation behavior where hydrate is forming at 46 percent of the MOC-predicted rate, indicating the system is not running at three-phase equilibrium. The low flow rate experiment (HVT0008) has a gas consumption rate that is 80 percent of the MOC-predicted value, indicating that the system is still not running at three-phase equilibrium, but is 1.7 times closer due to the lower flow rate. This indicates that lowering the flow rate reduces the rate-limitation on hydrate formation.

Figure 49 shows the gas consumption from the two experiments (HVT0005 and HVT0007) we've completed where the brine pump was shut off at 57 hours (black vertical line). Similar to Figure 28, the results are compared to the MOC solutions during a gas flooding and hydrate formation case, as well as the maximum potential gas consumption. After the brine pump was shut off, the gas consumption rate in HVT0005 and HVT0007 drops to 0.07 and 0.18 mL/hr, respectively. In both experiments, when the brine pump was stopped, that immediately reduced the gas consumption rate by 0.18 mL/hr, because brine withdrawal is no longer creating free space for gas. This accounts for 72% and 95% of the drop in average consumption rate in HVT0005 and HVT0007, respectively, but not the other 28 – 5% remaining. Additionally, the overall gas consumption rate decreases over time as both experiments near the MOC predicted gas consumption.

Test No.	Location	Brine Stopped	Temp Control Box	ϕ	P_{pore} (psi)	T_{conf} (degC)	Flow Rate (m/yr)	Salinity (wt%)	Salt
HVT0001	LBNL	Y	N	0.336	1000	4	0.78	0.07	NaCl
HVT0004	PRC	N	N	0.393	1775	1	0.78	0.07	NaBr
HVT0005	PGE	Y	N	0.383	1775	1	0.78	0.07	NaBr
HVT0007	PRC	Y	Y	0.393	1775	1	0.78	0.07	NaBr
HVT0008	PRC	Y	Y	0.377	1775	1	0.26	0.07	NaBr

Table 4. Experimental parameters for each of the successful hydrate formation experiments performed during Phase 2.

Hydrate saturation	0.275
Gas saturation at the gas inlet	0.303
Gas saturation at the front	0.652
Front moving velocity, mm/hour	0.62
Gas consumption rate, ml/hour	0.4139

Table 5. Predictions from the MOC analytical solution.
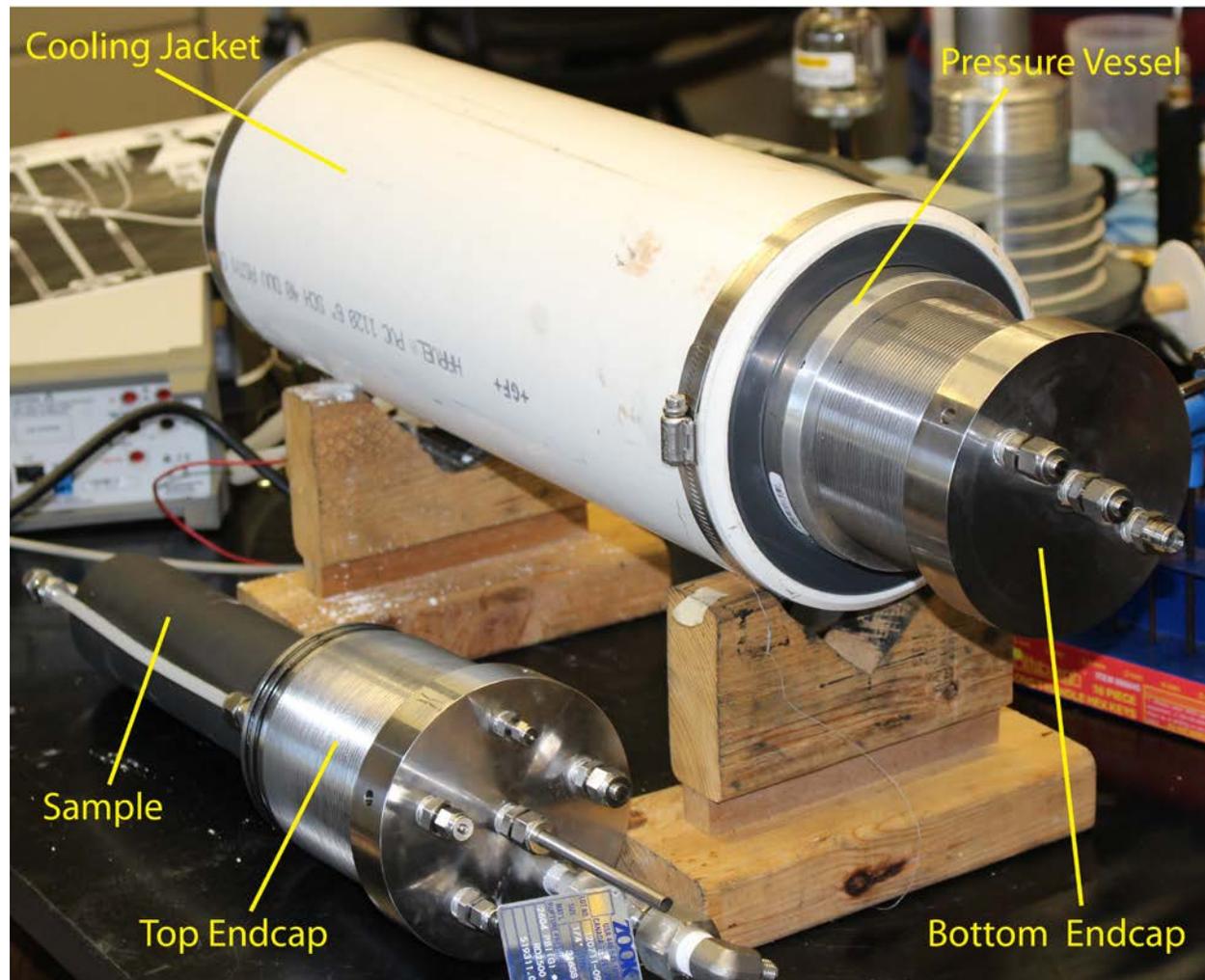
Figure 21. Disassembled hydrate formation vessel showing the top and bottom endcaps, the sample and fluid tubing, and the cooling jacket surrounding the aluminum sleeve.
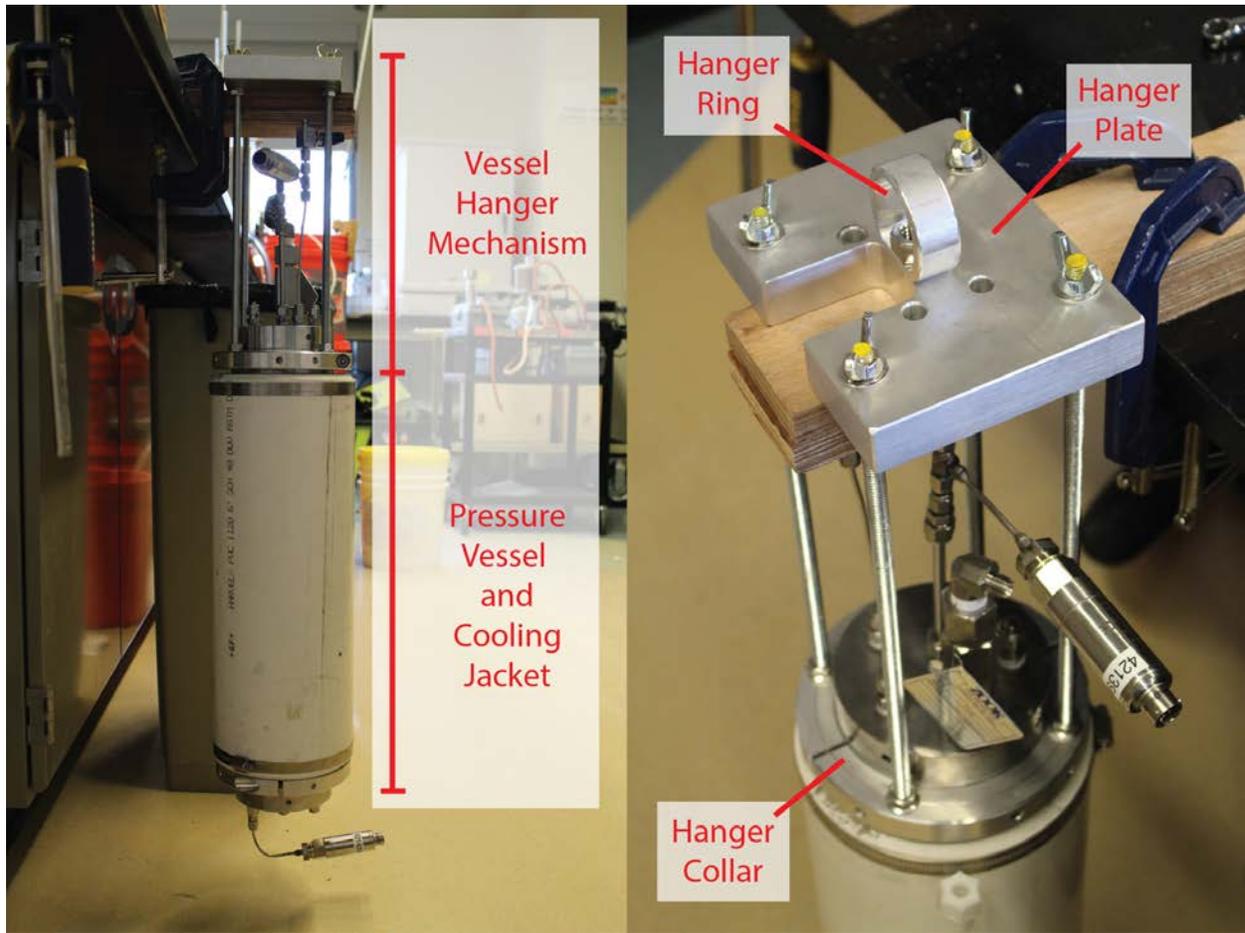
Figure 22: Image of hydrate formation vessel and hanger.
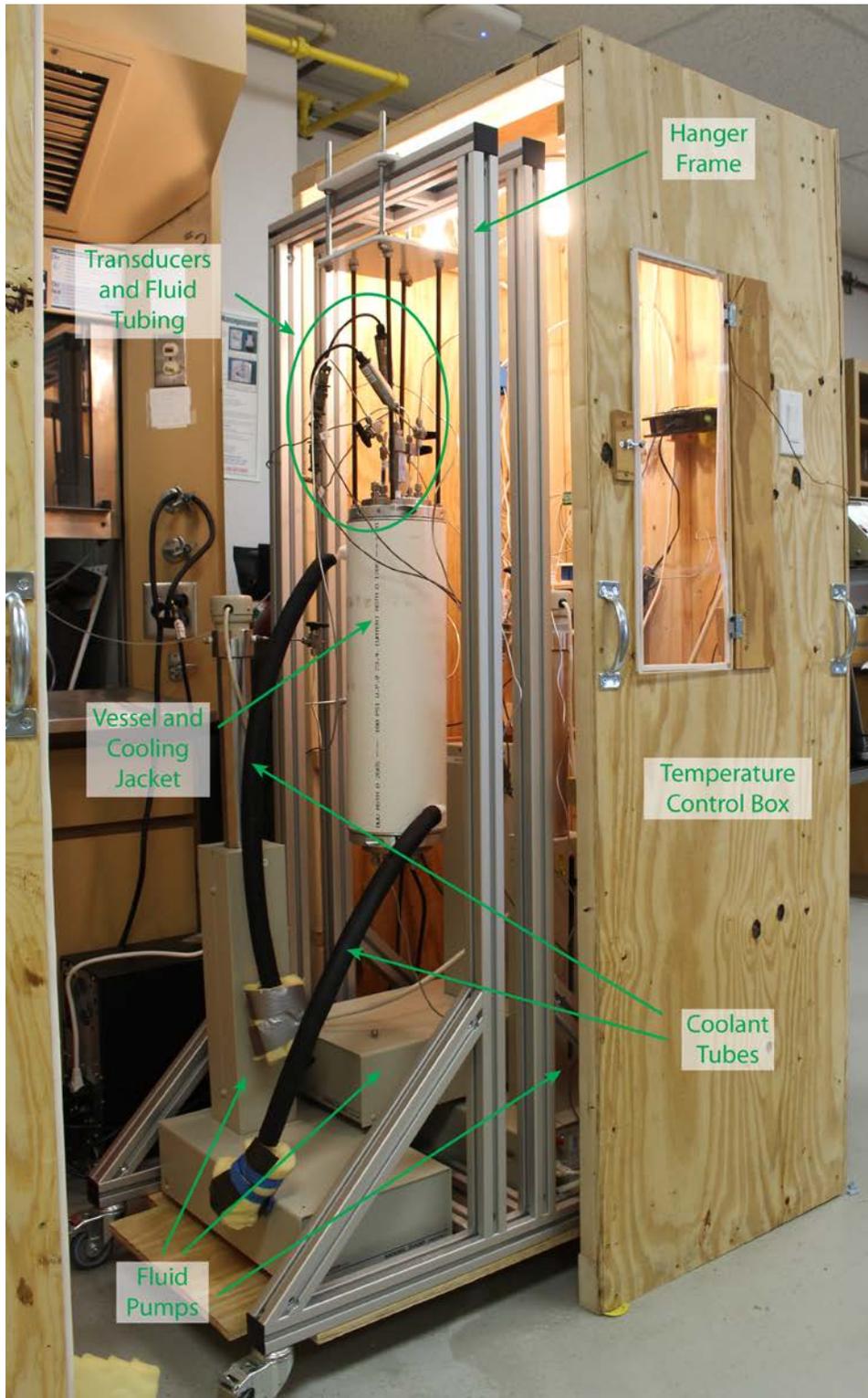
Figure 23: Hydrate formation vessel, aluminum hanger frame, and pore fluid pumps contained within the temperature control box. The two halves of the box close together to insulate the inside from the external room temperature. Four incandescent light bulbs act as heat sources to maintain a constant internal temperature.
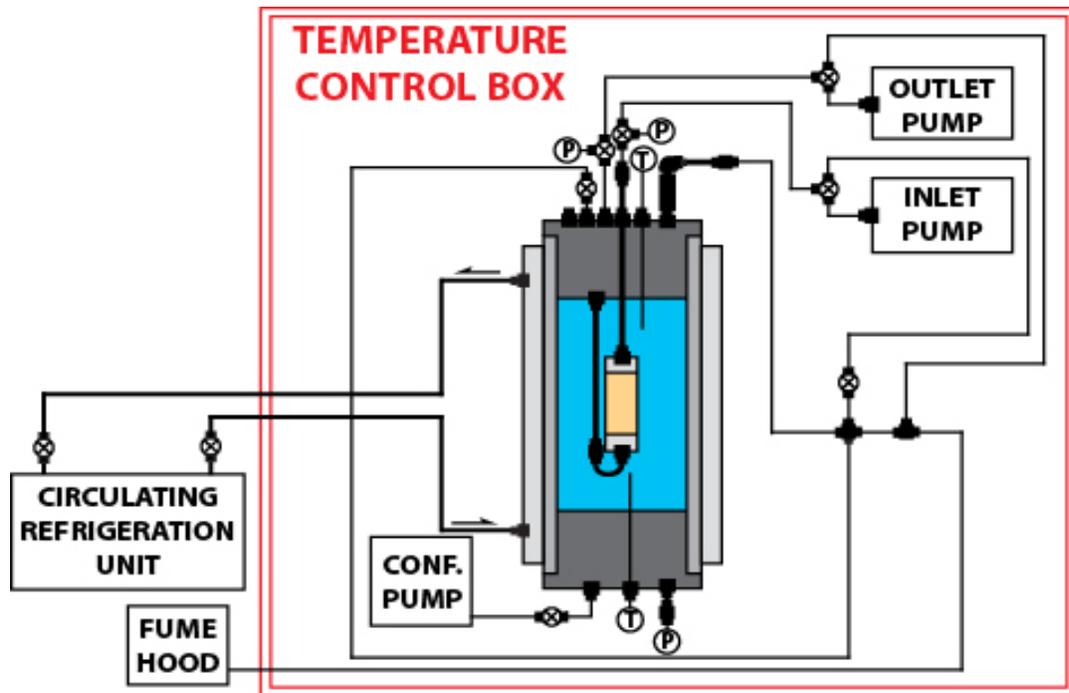
Figure 24: Schematic of the updated equipment setup for HVT0007 and associated plumbing and fittings. Inlet, outlet, and confining pumps were placed inside the temperature control box box to buffer them from diurnal temperature changes. P = pressure transducer; T = thermocouple.
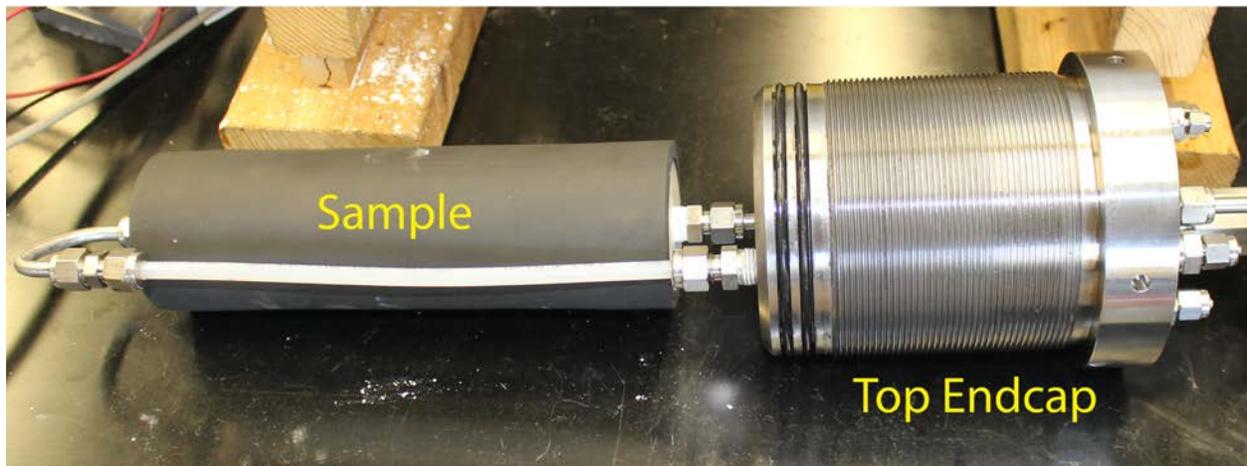
Figure 25: Image of sample connected to the top endcap by the inlet and outlet pore fluid tubing. Sample is encased in a 2" ID Viton sleeve.
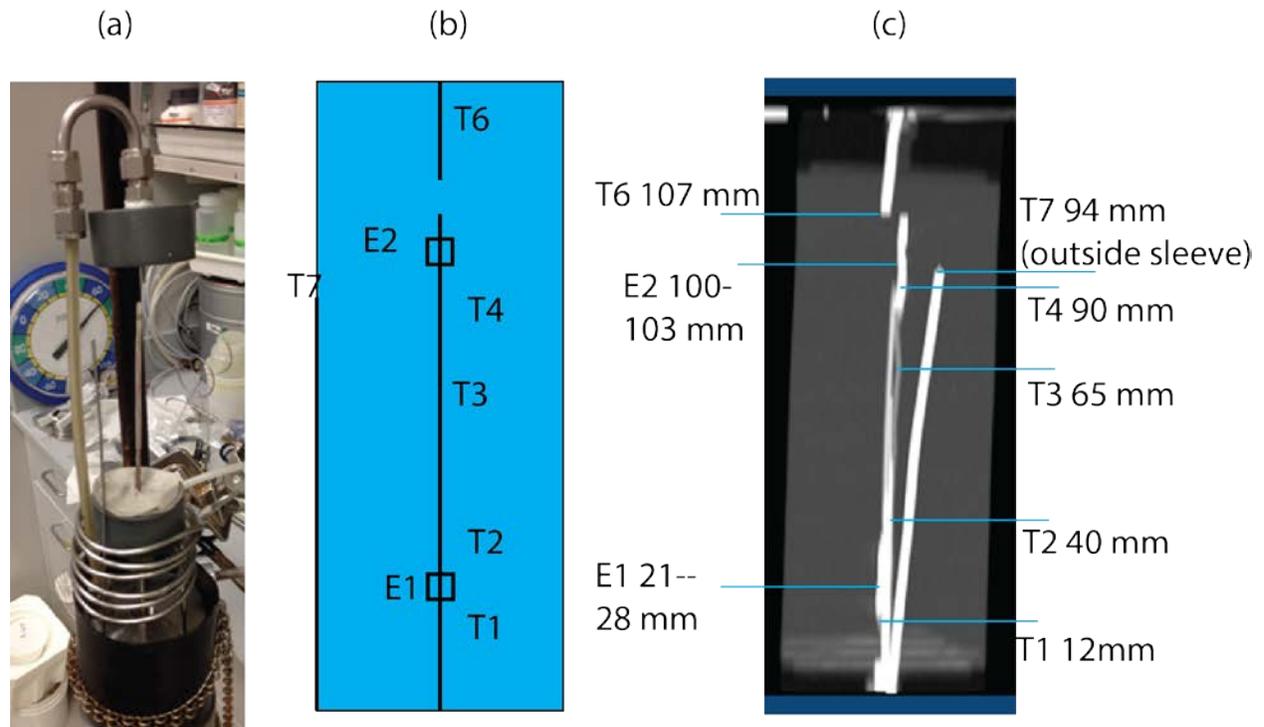
Figure 26: Instrument setup for thermocouples and electrodes in the sample and vessel. a. photo of assembly without EPDM sleeve or sample showing grey PVC endpieces, garolite rod with thermocouples and electrodes. b. schematic arrangement of instruments, c. X-ray image showing actual locations.

(a)
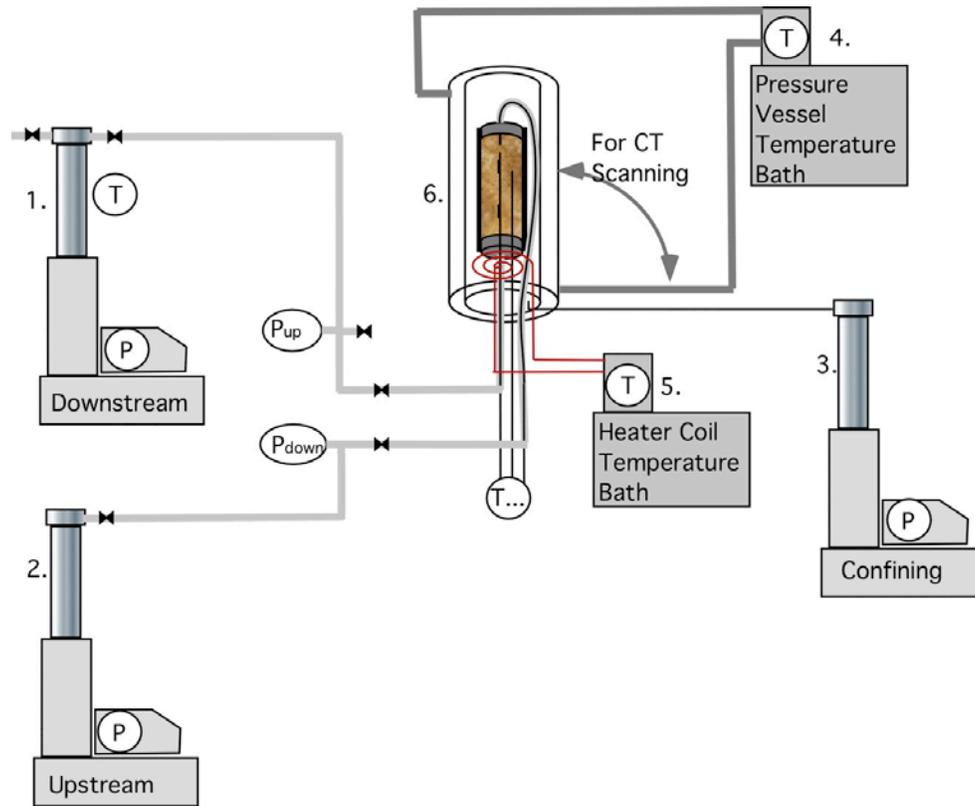
1 - 3. ISCO 500D High Pressure Syringe Pump
4-5. Temperature Controllers
6. Pressure Vessel w/ Sample

(b)
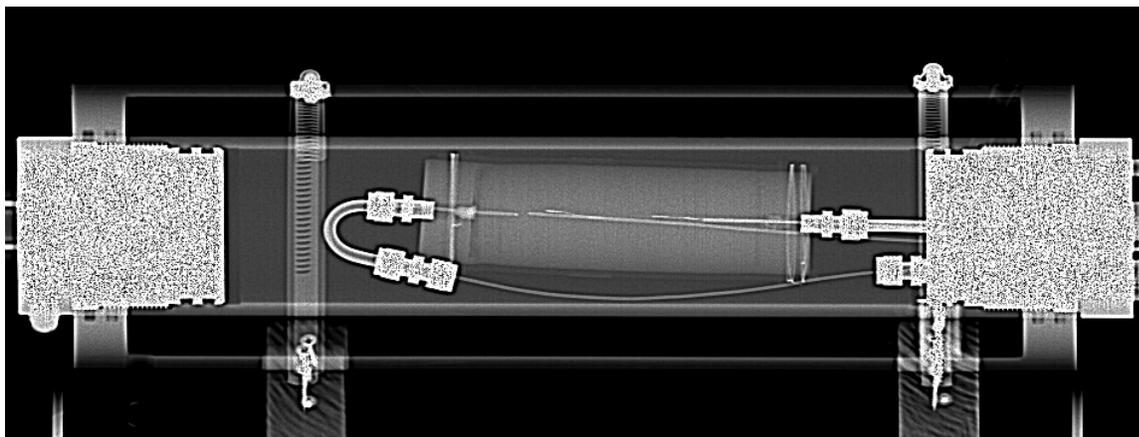
Figure 27: System setup. a. schematic showing sample configuration with respect to pumps controlling brine inlet to the sample bottom (downstream pump), gas inlet to the sample top (upstream pump), a pump to maintain confining pressure around the sample, and temperature control baths. b. X-ray scan showing sample, pressure vessel, and thermal jacket.

(a)
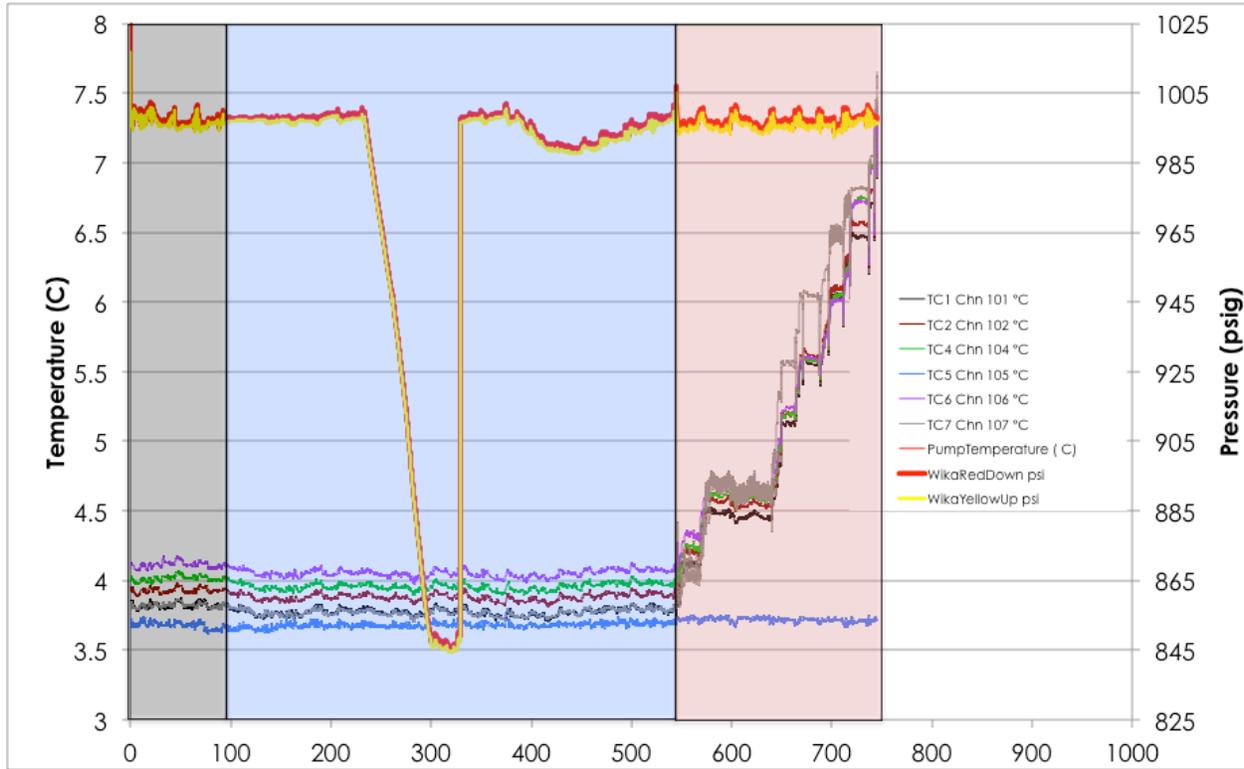
(b)
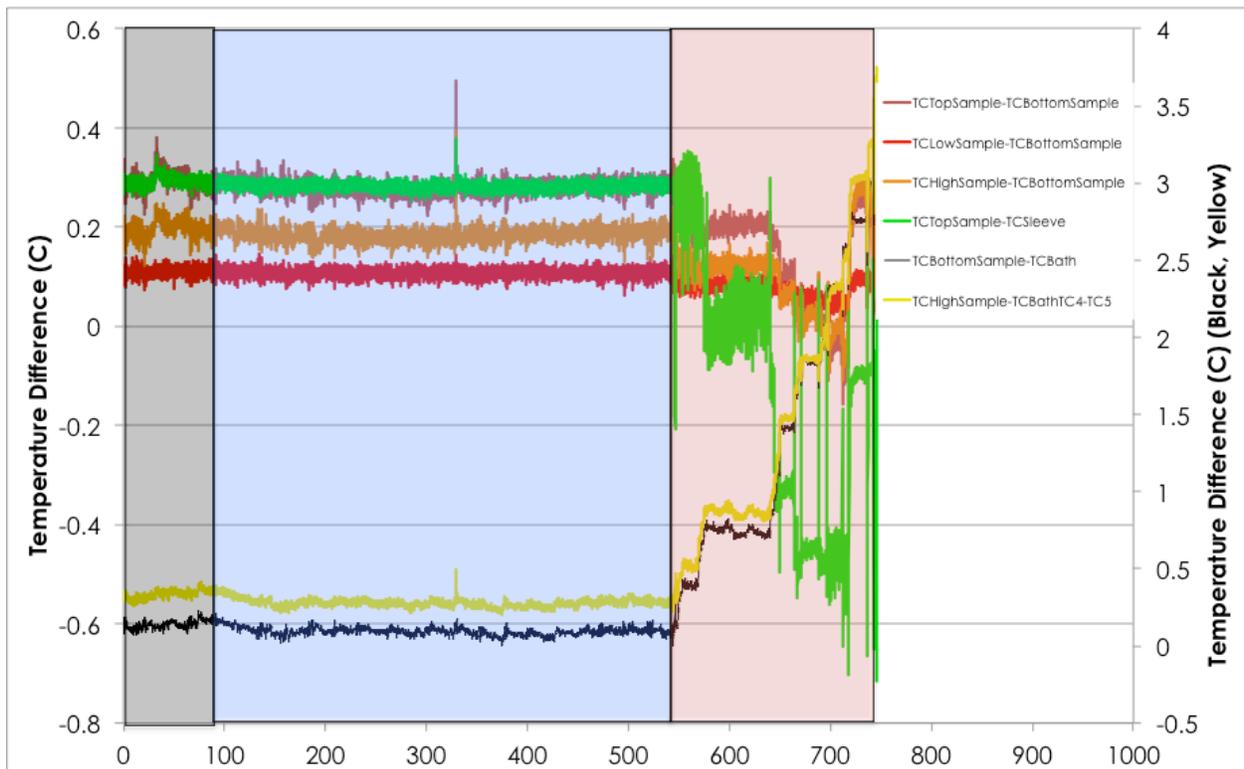
(c)
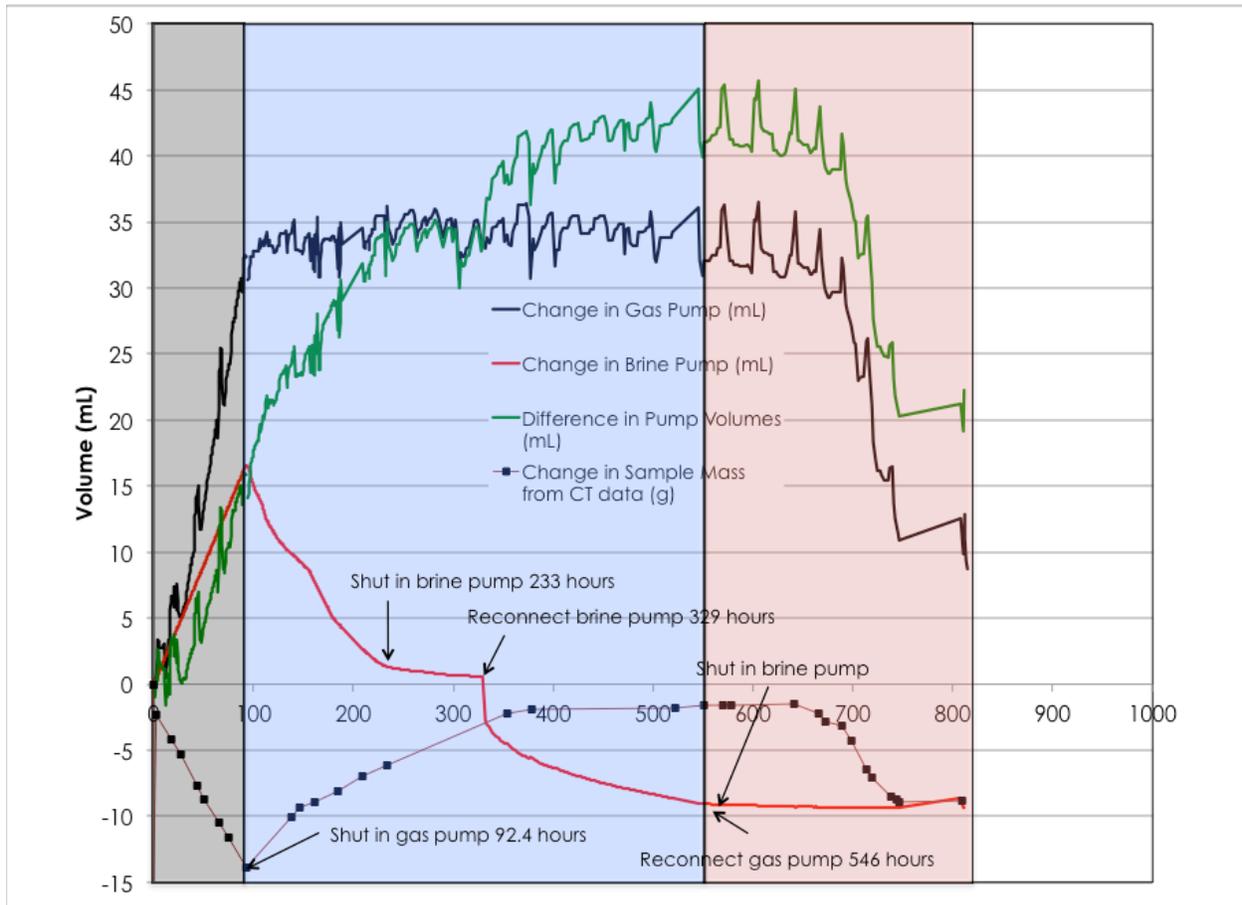
Figure 28: Test conditions. a. Temperatures and pressures over the test duration, b. temperature differences over the test duration, and c. fluid volumes from the syringe pumps, and sample mass computed from X-ray CT scans.
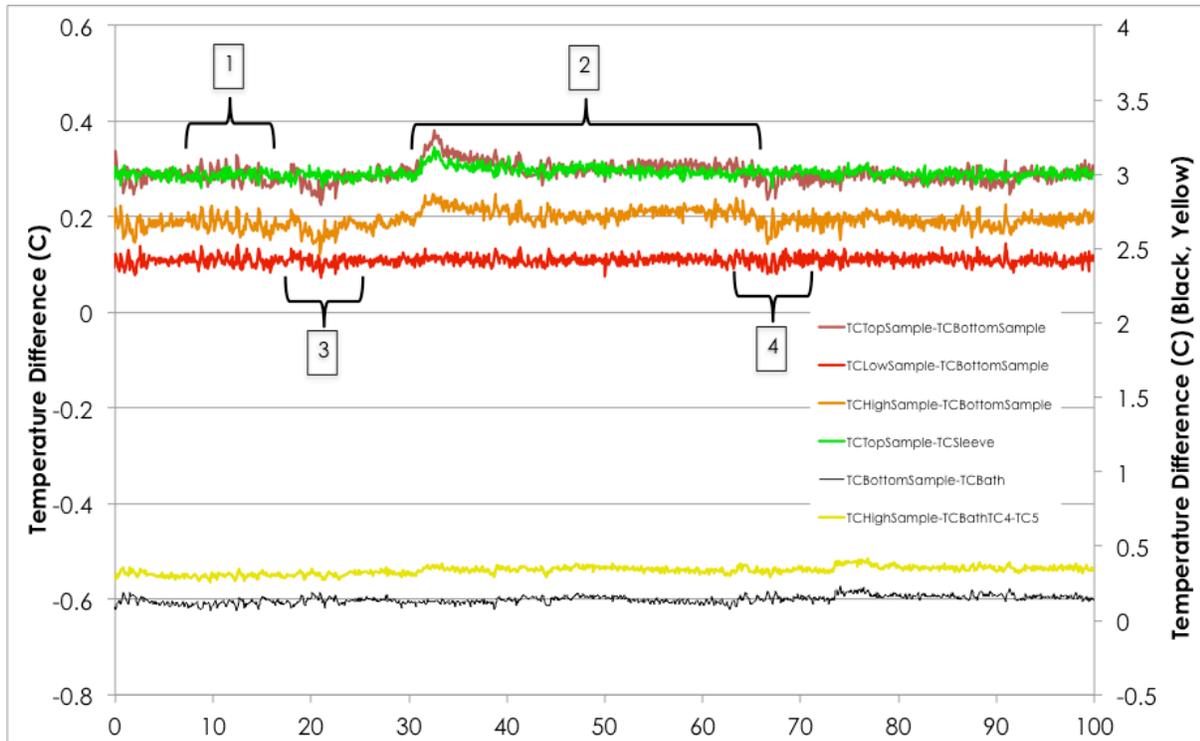
Figure 29: Temperature differences over the drainage test. Increases indicate hydrate formation.
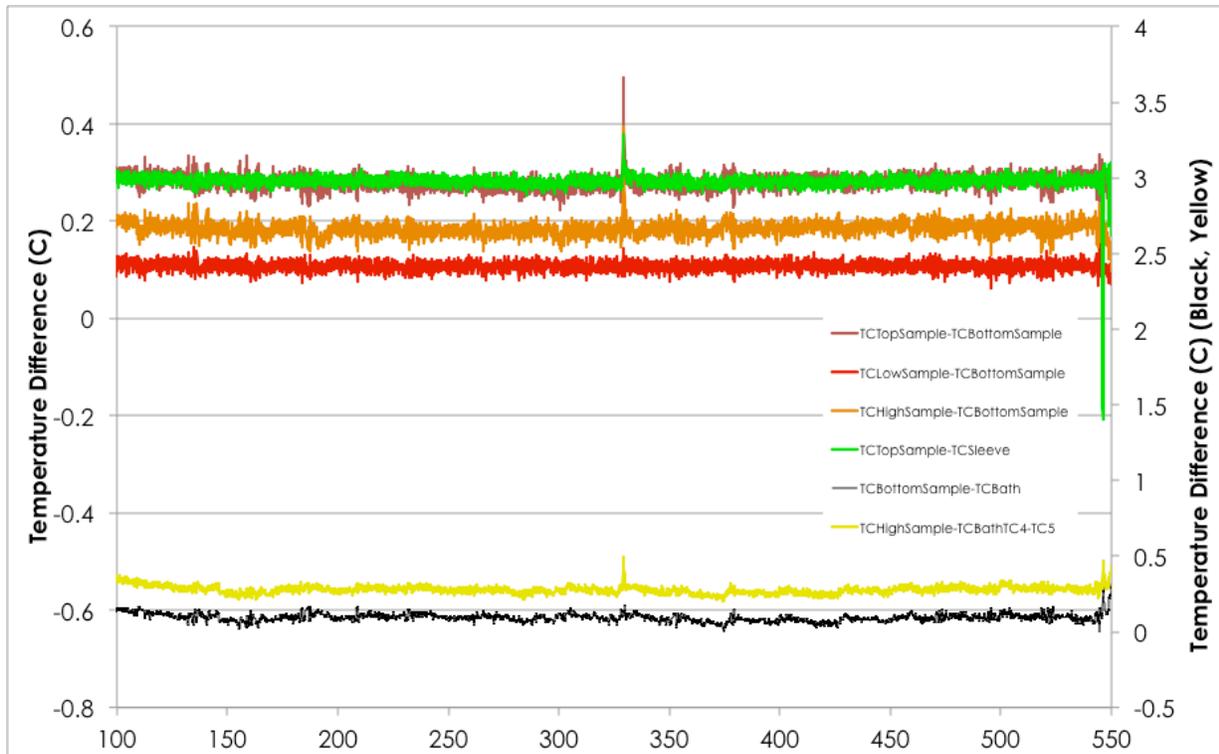
Figure 30: Temperature differences over the imbibition test. Increases indicate hydrate formation.
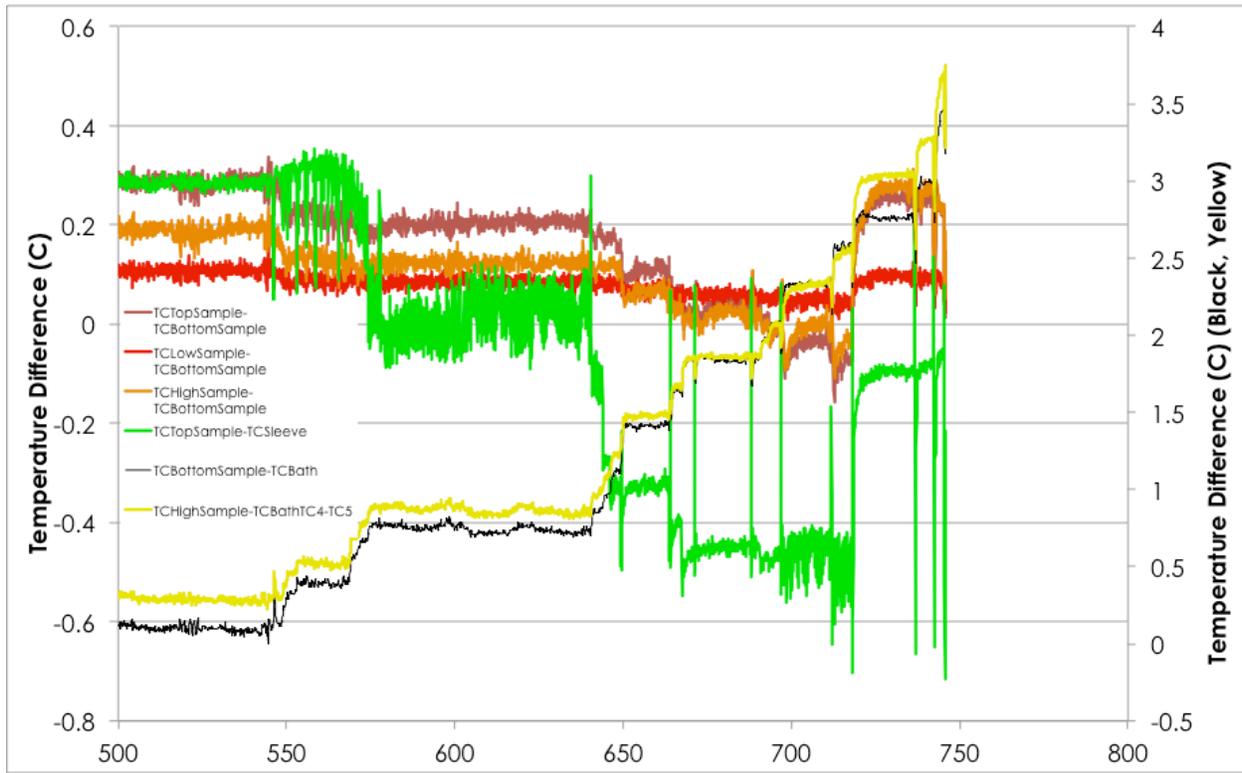
Figure 31: Temperature differences during dissociation. Temperature gradients neutralized and reversed over the 650 to 720 hour period when hydrate dissociation was dominant.
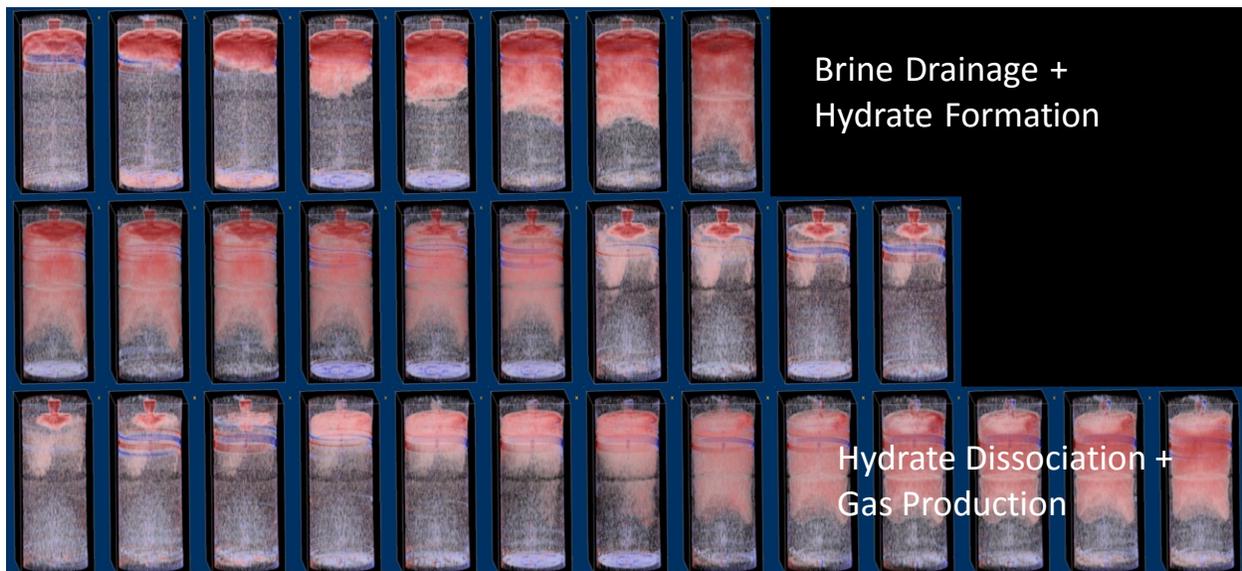
Figure 32: X-ray CT difference images showing density changes in the sample. Red indicates lower density than the initial condition (the highest density) and blue shows increases in density.
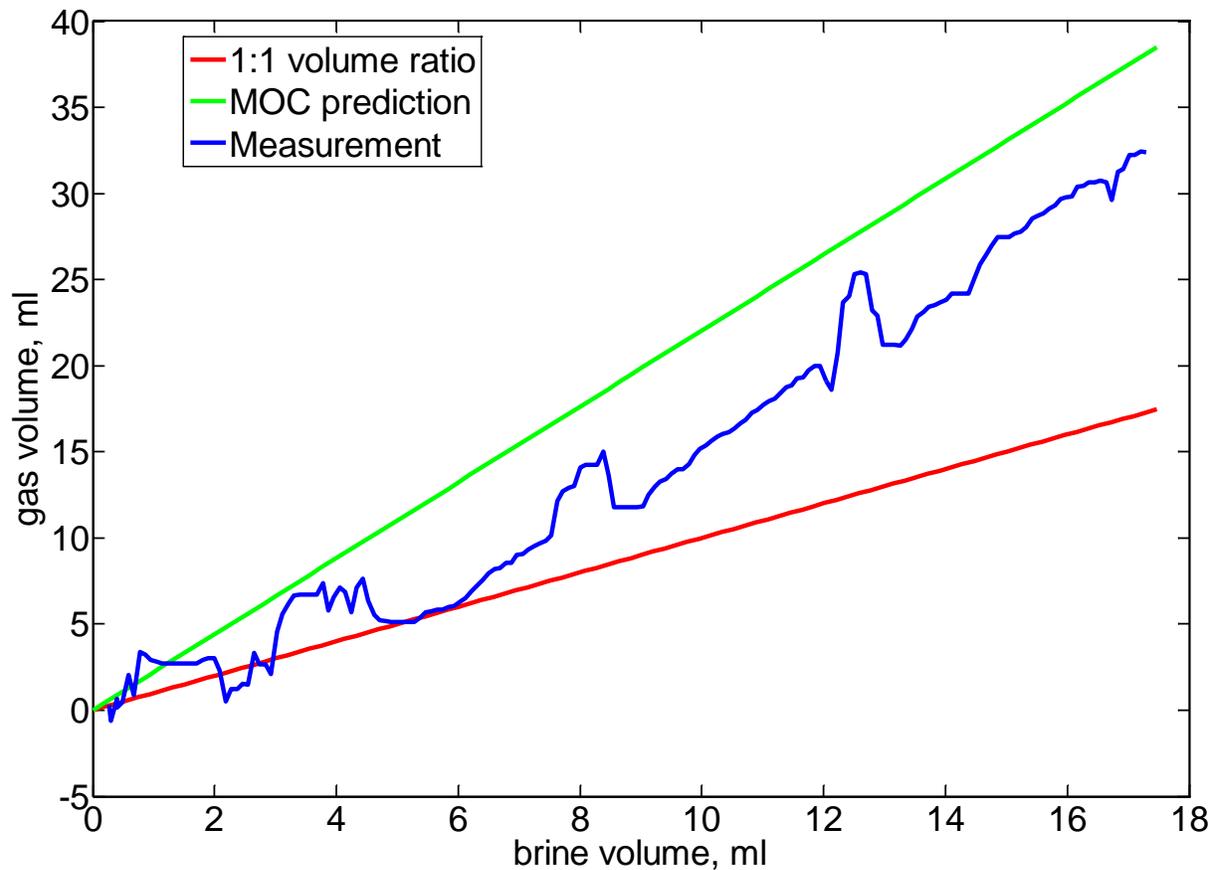
**Figure 33: Comparison of gas consumption data for hydrate formation front experiment HVT0001 (blue line).
Red line indicates the MOC solution for a gas flooding experiment and indicates the minimum gas consumption
needed to maintain volume balance. Green line indicates the gas consumption predicted from the MOC solution
for these experiments calculated at the experimental temperature and pressure conditions.**
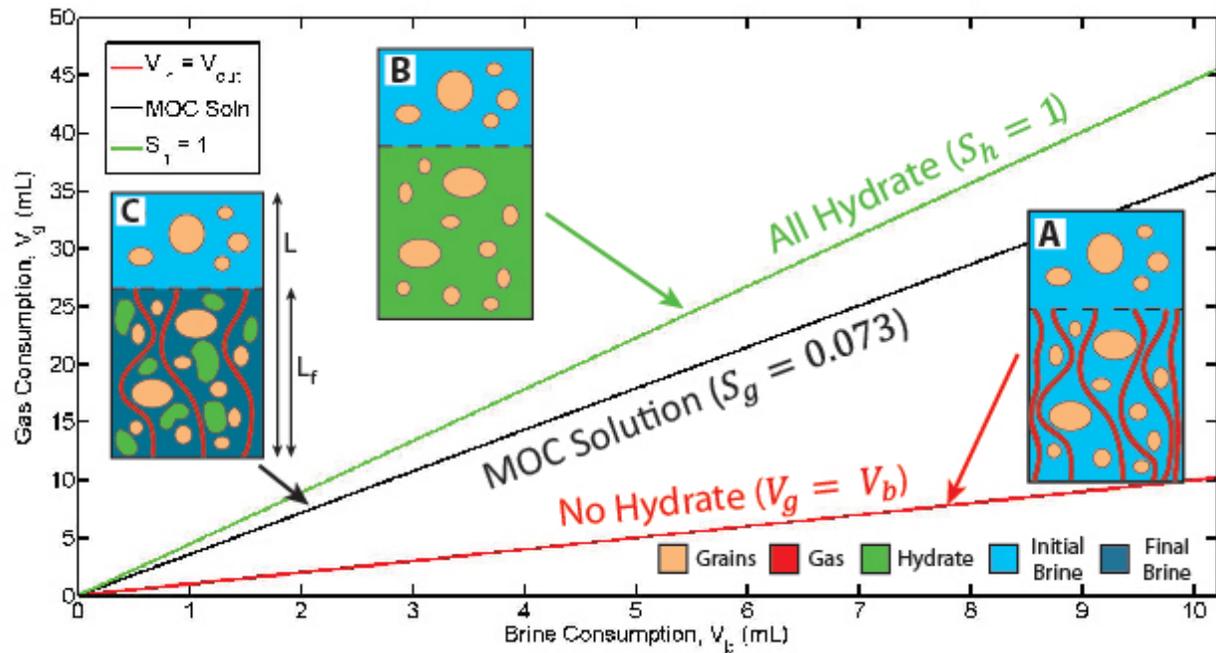
Figure 34: Description of the three gas consumption end member cases: A) no hydrate phase (red line); B) hydrate phase only (green line); C) the Methods of Characteristics (MOC) solution (black line). The no hydrate phase line assumes volume balance between the water withdrawn and the gas consumed. The hydrate phase only line assumes the hydrate saturation is equal to 1 behind the front and calculates the volume of gas required to form that hydrate. The MOC solution (You et al., 2015) is calculated at experimental P-T conditions and reflects the predicted gas consumption for the experiment. The inset figures (A, B, and C) show, graphically, the phases present ahead of and behind the front (dashed line) in each case.
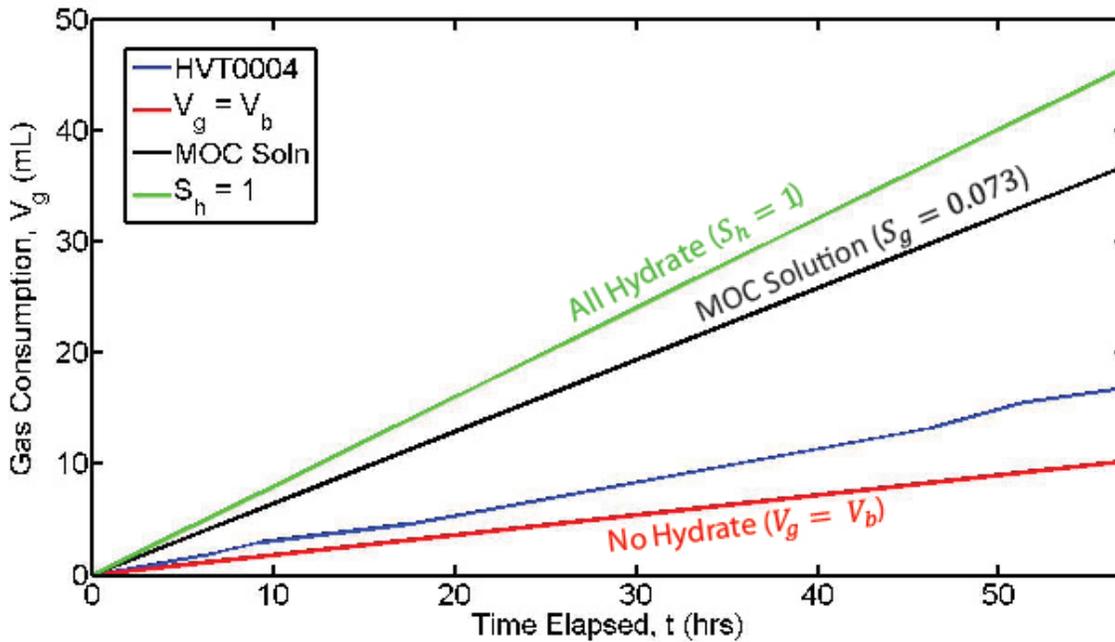
Figure 35: Comparison of gas consumption data for hydrate formation front experiment HVT0004 (blue line). Red line indicates the MOC solution for a gas flooding experiment and indicates the minimum gas consumption needed to maintain volume balance. Black line indicates the gas consumption predicted from the MOC solution for these experiments calculated at the experimental temperature and pressure conditions. Green line indicates the maximum potential gas consumption assuming that all the space made available through water withdrawal is occupied by hydrate.
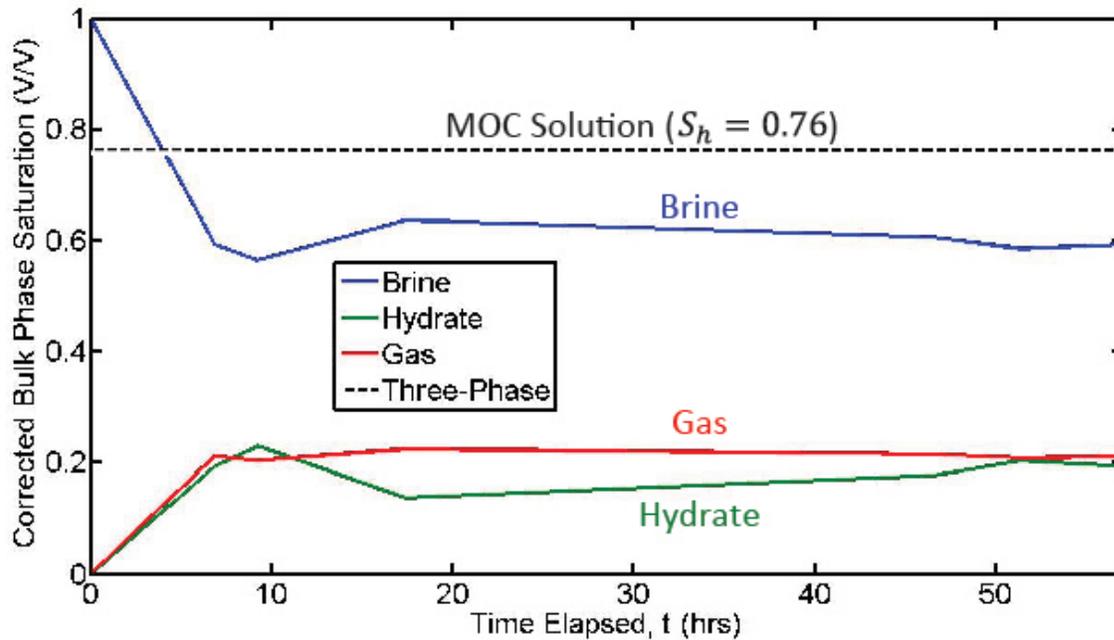
Figure 36: Brine (blue line), hydrate (green line), and gas (red line) bulk phase saturations from mass balance behind the hydrate formation front for experiment HVT0004. Black dashed line shows the predicted hydrate saturation required to elevate the in-situ salinity to three-phase equilibrium conditions.
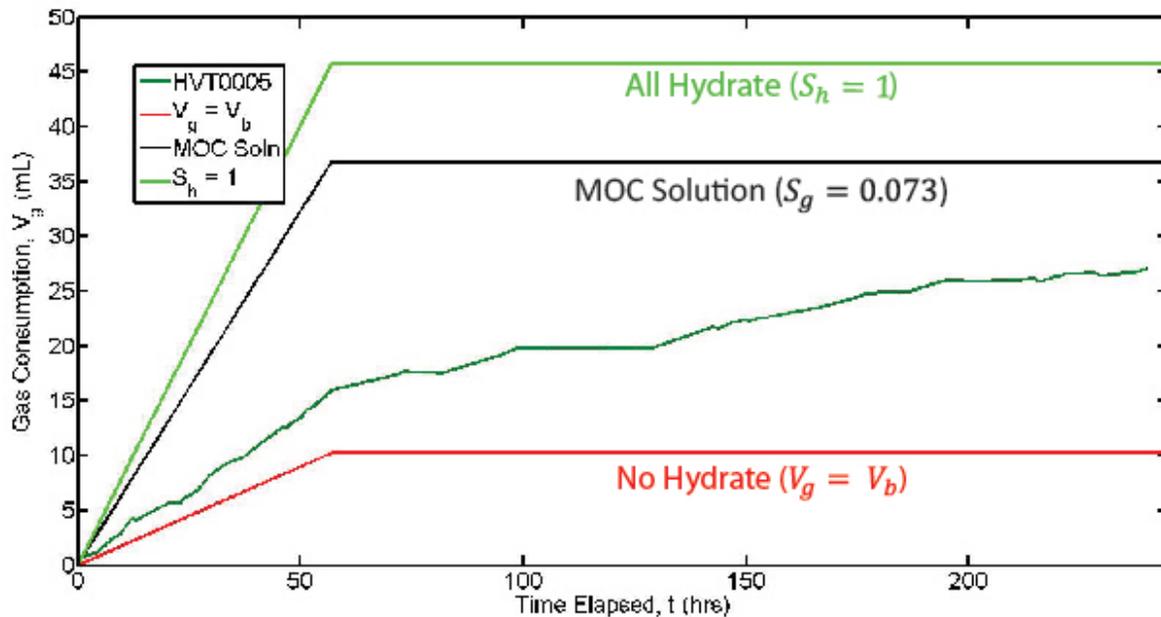

Figure 37: Comparison of gas consumption data for hydrate formation front experiment HVT0005 (dark green line). Red line indicates the MOC solution for a gas flooding experiment and indicates the minimum gas consumption needed to maintain volume balance. Black line indicates the gas consumption predicted from the MOC solution for these experiments calculated at the experimental temperature and pressure conditions. Green

line indicates the maximum potential gas consumption assuming that all the space made available through water withdrawal is occupied by hydrate.
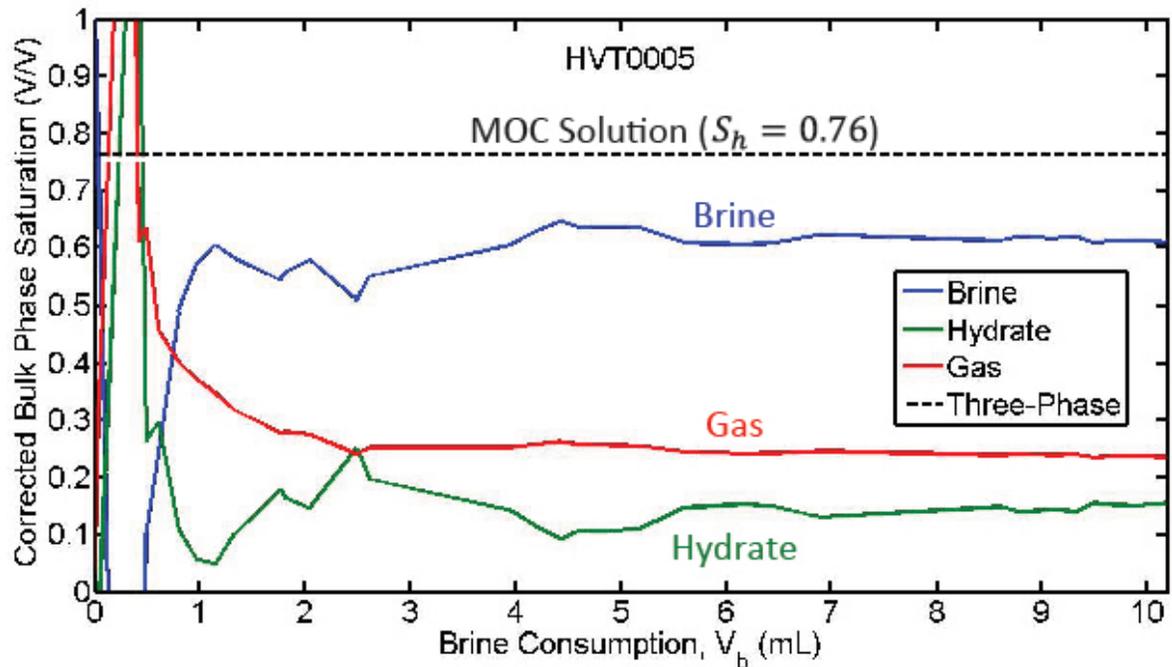
Figure 38: Brine (blue line), hydrate (green line), and gas (red line) bulk phase saturations from mass balance behind the hydrate formation front for experiment HVT0005. Black dashed line shows the predicted hydrate saturation required to elevate the in-situ salinity to three-phase equilibrium conditions.
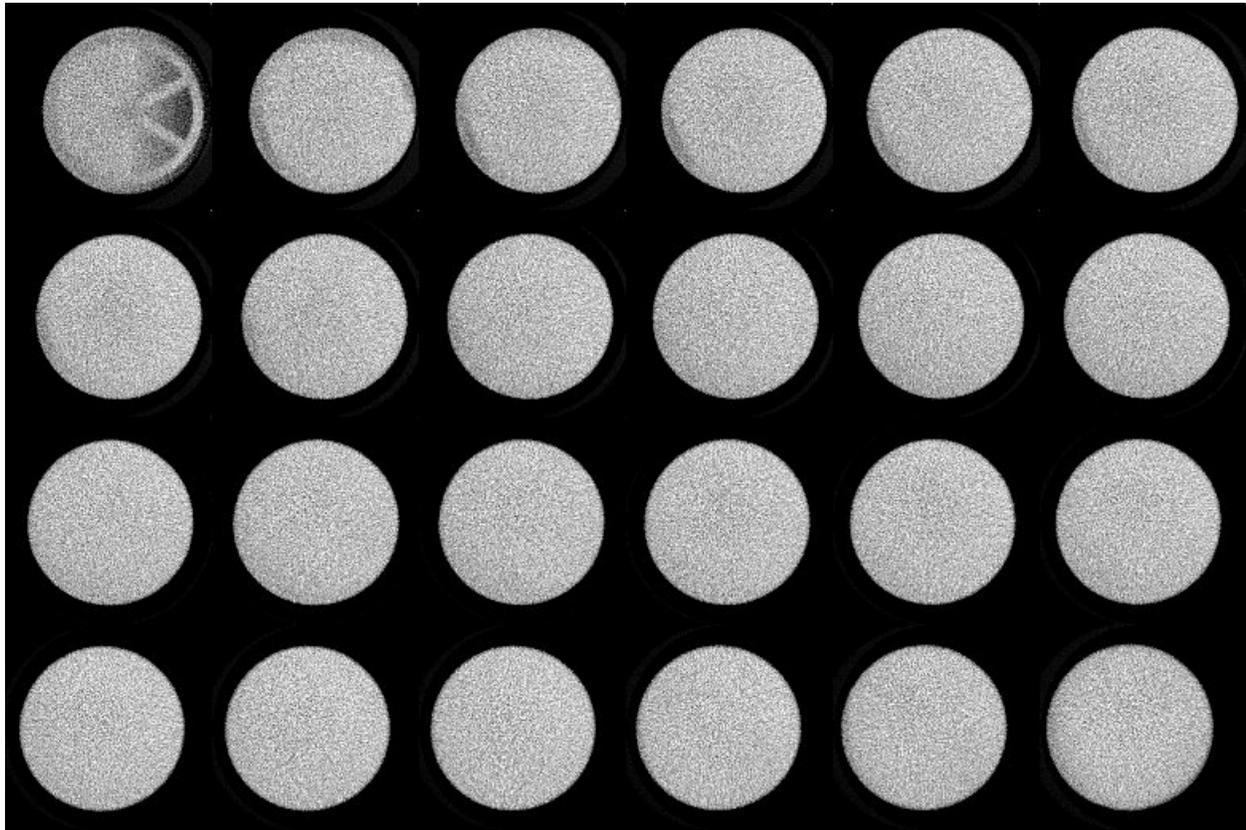
Figure 39: Montage of CT slices taken on the initial sample. Top left shows the endcap grooves at the sample outlet. Bottom right is the location of the inlet. Slices are spaced 0.5 cm apart within the sample. There is a low density region apparent in the bottom left portion of the slices in the lower 2.5 cm of the sample, which could be due to heterogeneous packing.
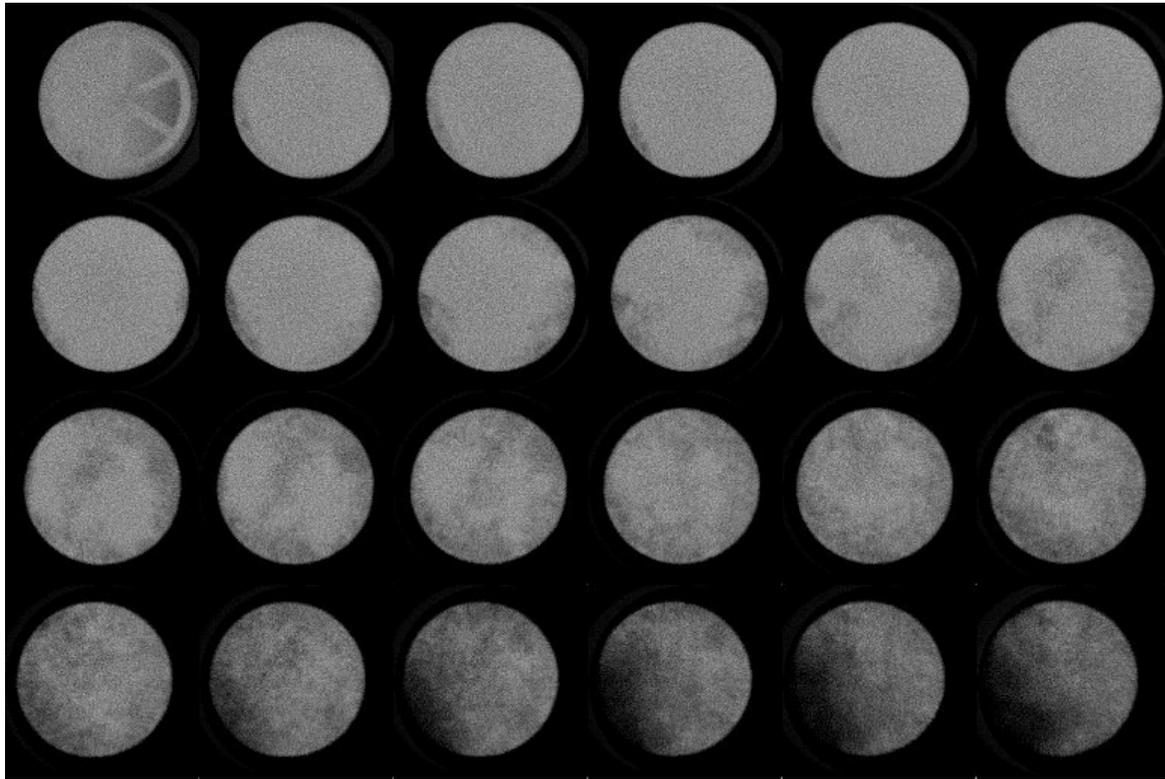
Figure 40: Montage of CT slices taken after 180 hours had elapsed. Top left shows the endcap grooves at the sample outlet. Bottom right is the location of the inlet. Slices are spaced 0.5 cm apart within the sample. The low density region in the lower 2.5 cm is still apparent. Low density regions in the upper 8cm of the sample are likely due to the presence of free gas and hydrate.
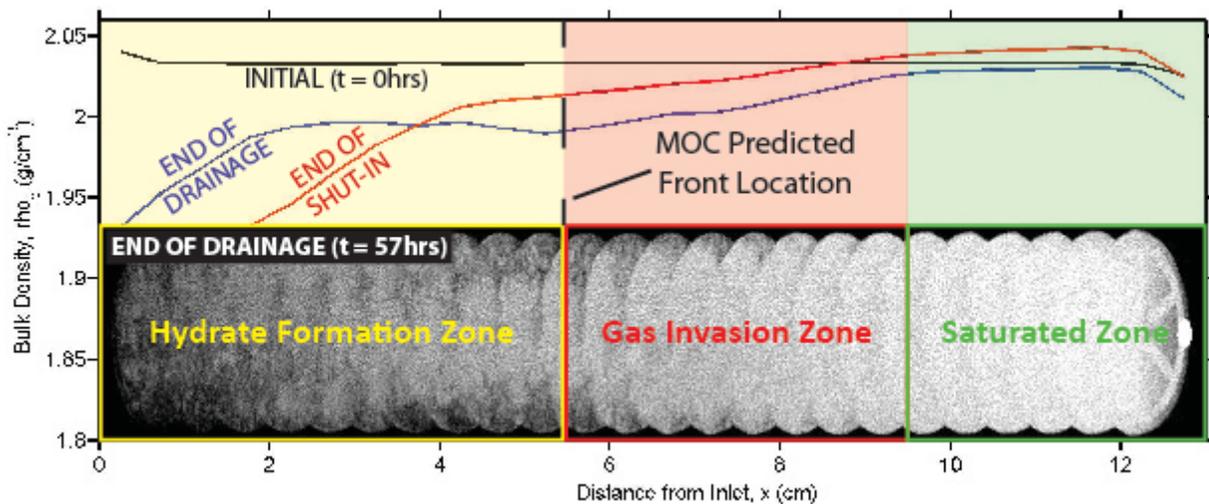

Figure 41: CT mass attenuation results for HVT0005 at the end of the drainage phase (57 hours). Slices were taken at 0.5cm spacing with a 1cm thickness. Lighter colors indicate high density. Darker colors indicate lower density. The hydrate formation, gas invasion, and brine-saturated zones were determined using the MOC model, bulk density profiles, and the CT scans.
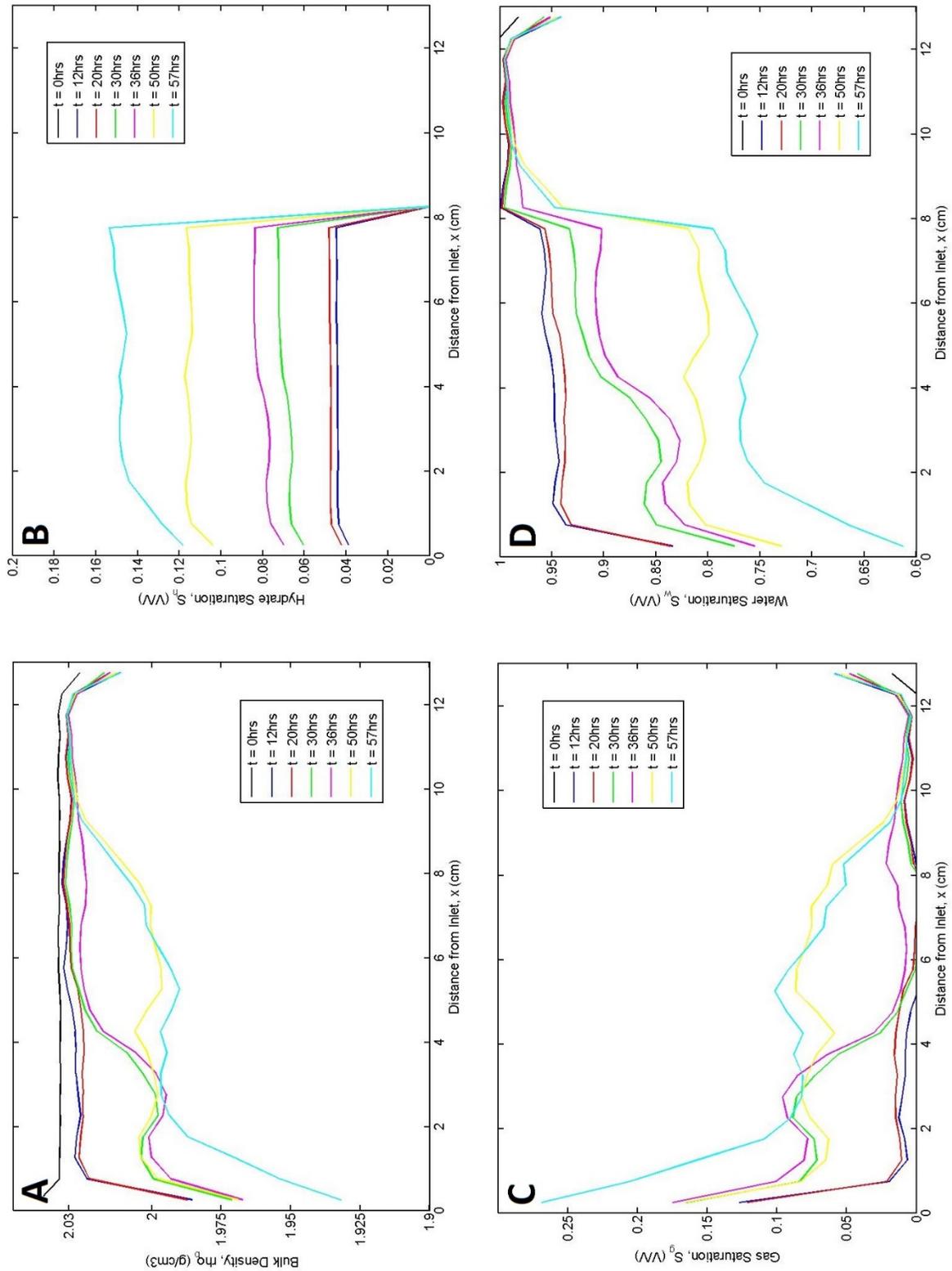
Figure 42: CT-derived A) bulk density, B) hydrate saturation, C) gas saturation, and D) water saturation profiles during the brine withdrawal period (0 – 57 hours) of HVT0005.
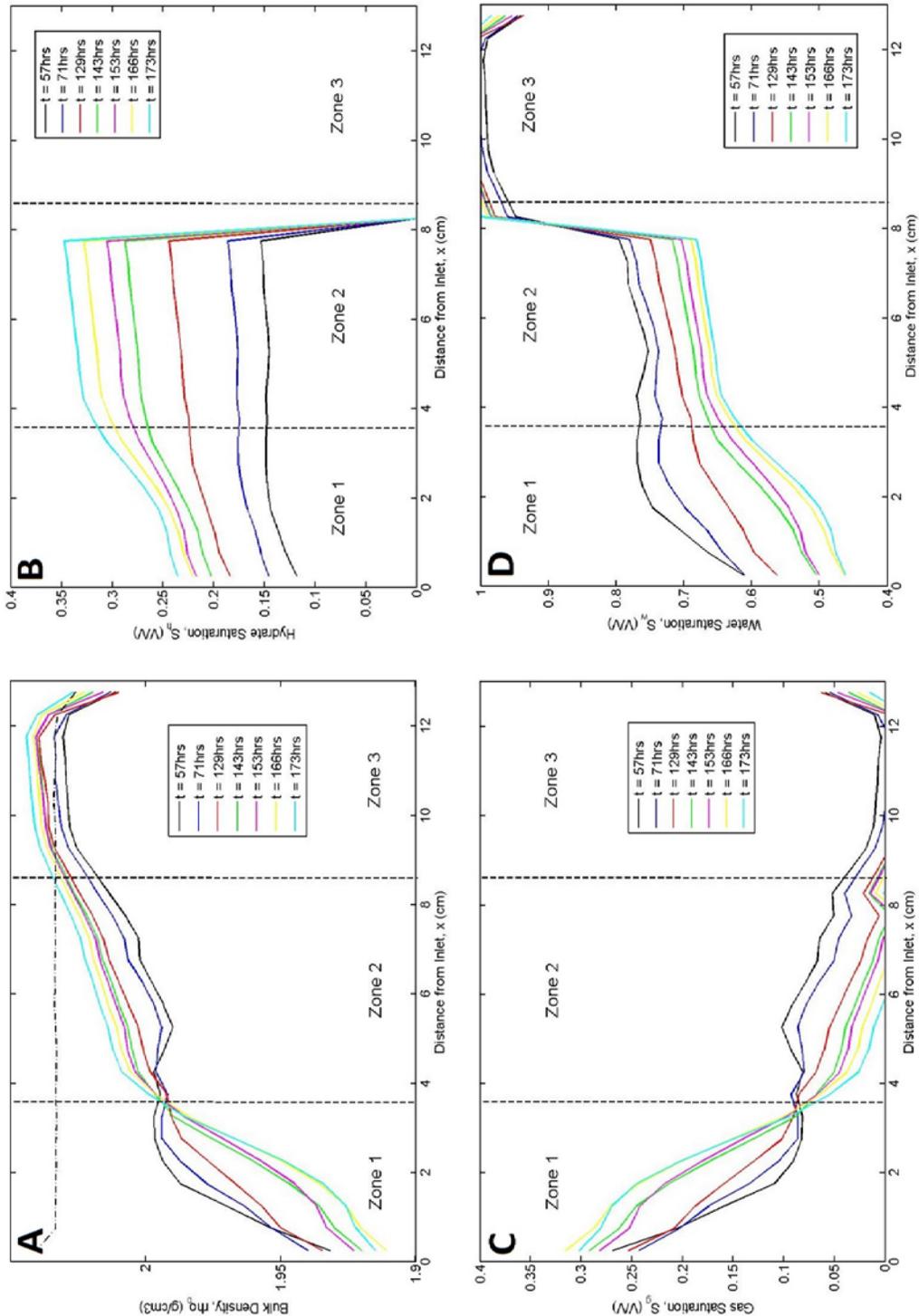
Figure 43: CT-derived A) bulk density, B) hydrate saturation, C) gas saturation, and D) water saturation profiles for HVT0005 after the brine pump was shut off and the outlet valve was closed (57 – 172 hours). Zones 1 – 3 were identified from bulk density trends after the brine was shut in. Zone shows continued density decrease, Zone 2 shows a density rebound to near initial values, and Zone 3 shows a density increase to greater than initial values.
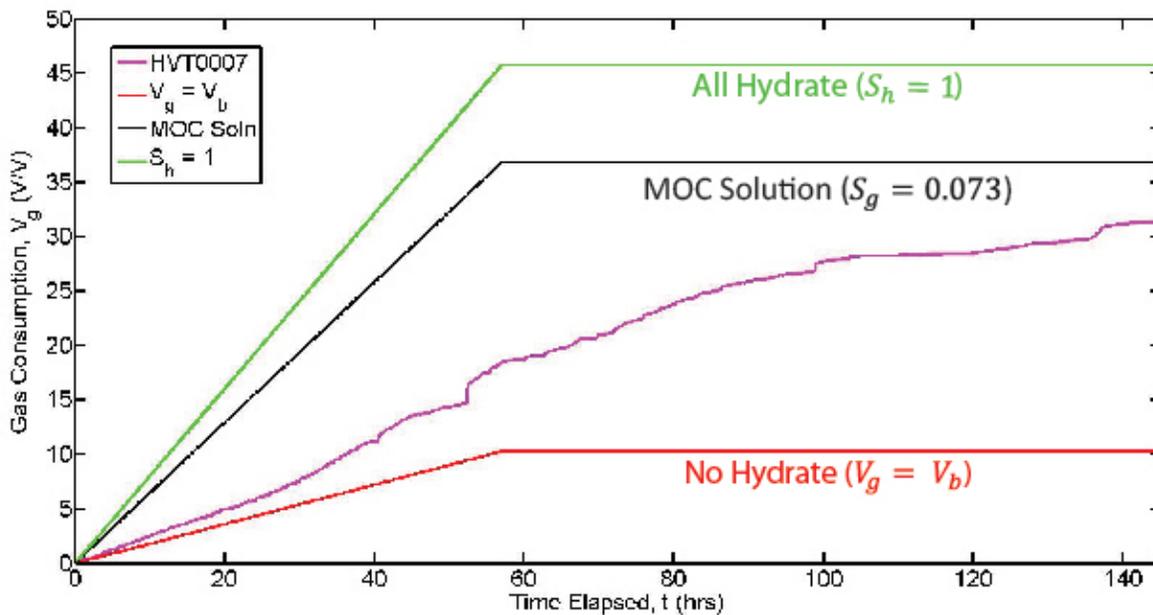
Figure 44: Comparison of gas consumption data for hydrate formation front experiment HVT0007 (pink line). Red line indicates the MOC solution for a gas flooding experiment and indicates the minimum gas consumption needed to maintain volume balance. Black line indicates the gas consumption predicted from the MOC solution for these experiments calculated at the experimental temperature and pressure conditions. Green line indicates the maximum potential gas consumption assuming that all the space made available through water withdrawal is occupied by hydrate.
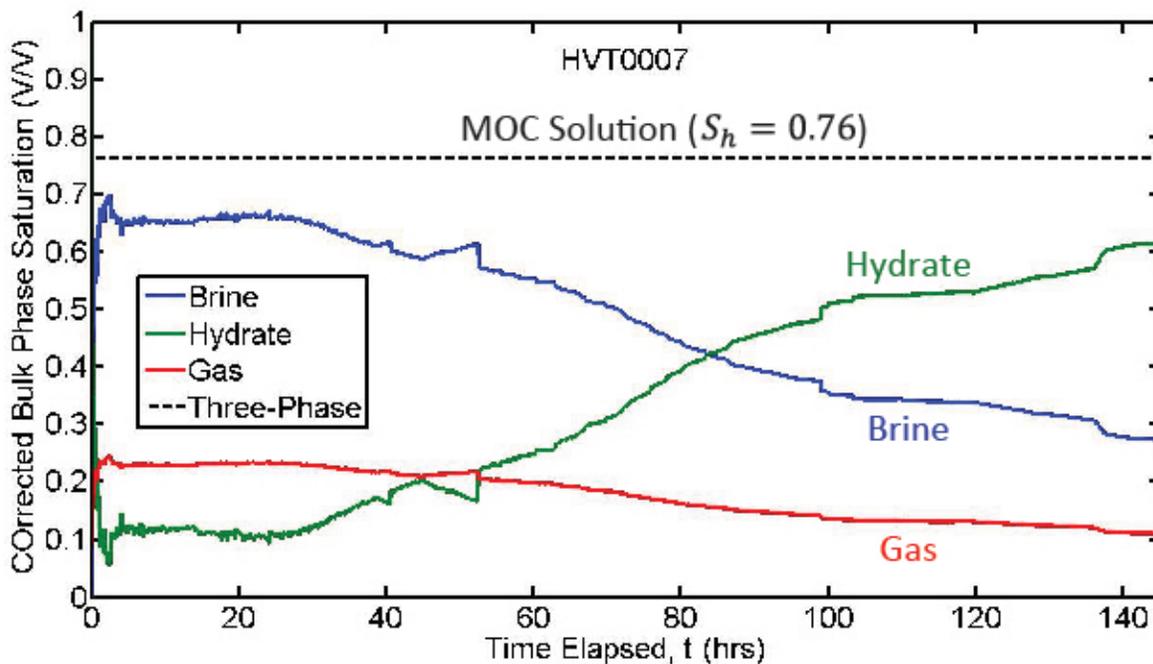

Figure 45: Brine (blue line), hydrate (green line), and gas (red line) bulk phase saturations from mass balance behind the hydrate formation front for experiment HVT0007. Black dashed line shows the predicted hydrate saturation required to elevate the in-situ salinity to three-phase equilibrium conditions.
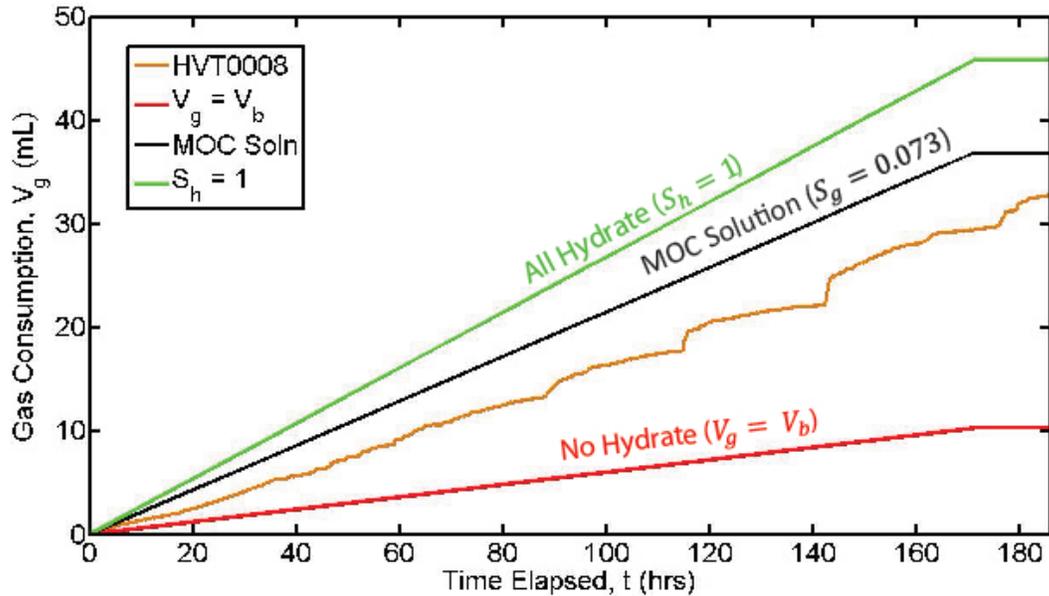
Figure 46: Comparison of gas consumption data for hydrate formation front experiment HVT0008 (orange line) Red line indicates the MOC solution for a gas flooding experiment and indicates the minimum gas consumption needed to maintain volume balance. Black line indicates the gas consumption predicted from the MOC solution for these experiments calculated at the experimental temperature and pressure conditions. Green line indicates the maximum potential gas consumption assuming that all the space made available through water withdrawal is occupied by hydrate.
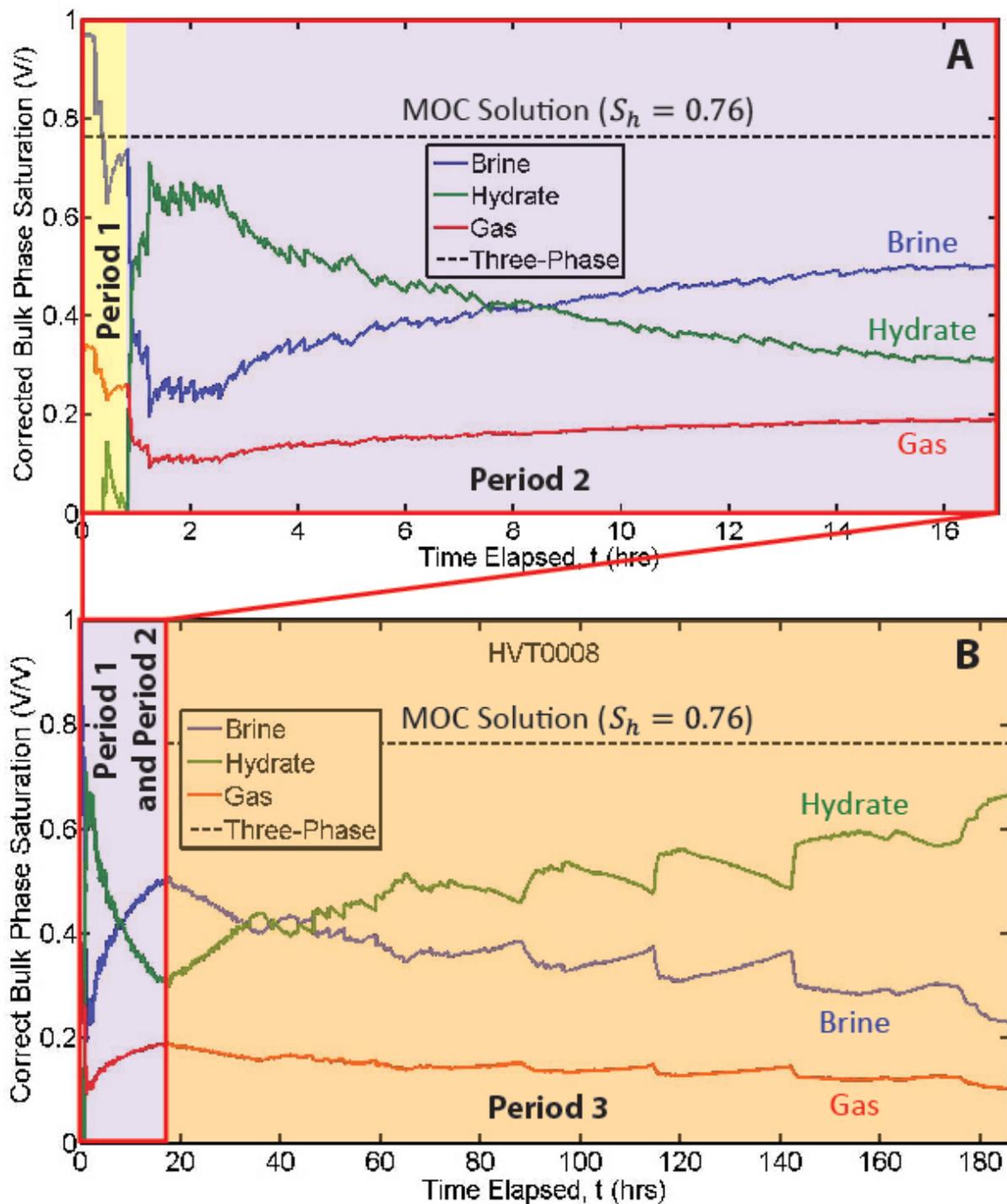
Figure 47: Brine (blue line), hydrate (green line), and gas (red line) bulk phase saturations from mass balance behind the hydrate formation front for the low flow rate experiment, HVT0008, from A) 0 – 17 hours and B) 0 – 186 hours. Black dashed line shows the predicted hydrate saturation required to elevate the in-situ salinity to three-phase equilibrium conditions.
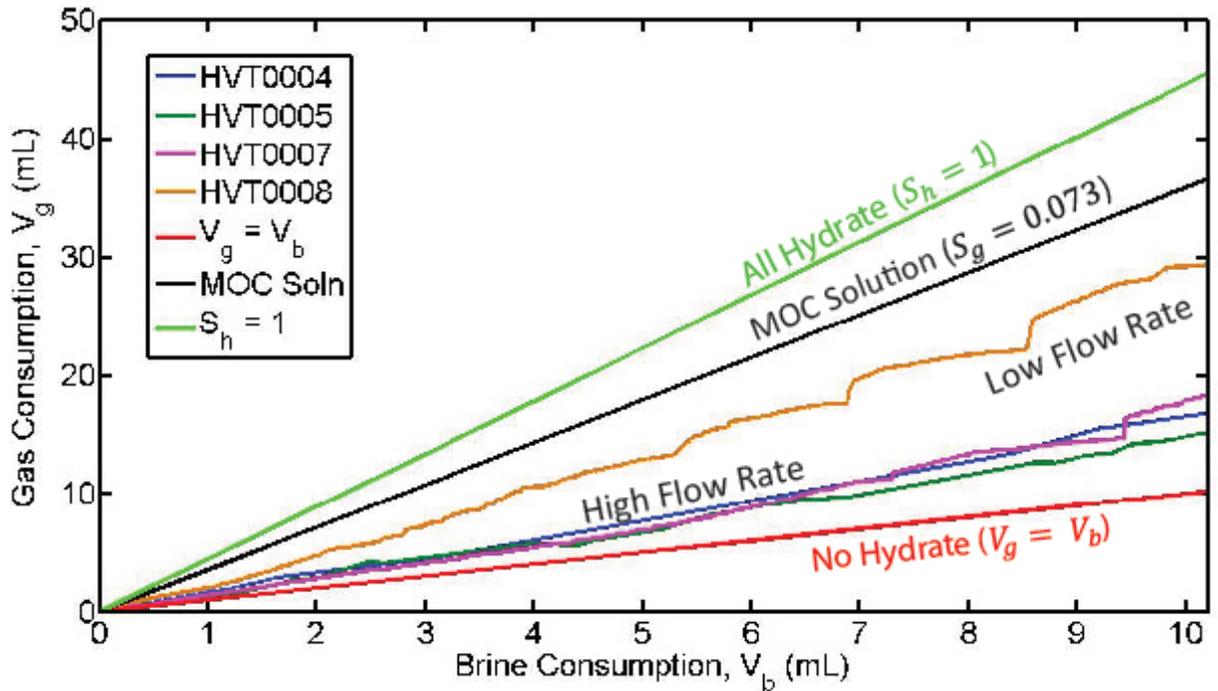
Figure 48: Comparison of gas consumptions from the high and low flow rate experiments during the drainage phase. Red line indicates the MOC solution for a gas flooding experiment and indicates the minimum gas consumption needed to maintain volume balance. Black line indicates the gas consumption predicted from the MOC solution for these experiments calculated at the experimental temperature and pressure conditions. Green line indicates the maximum potential gas consumption assuming that all the space made available through water withdrawal is occupied by hydrate.
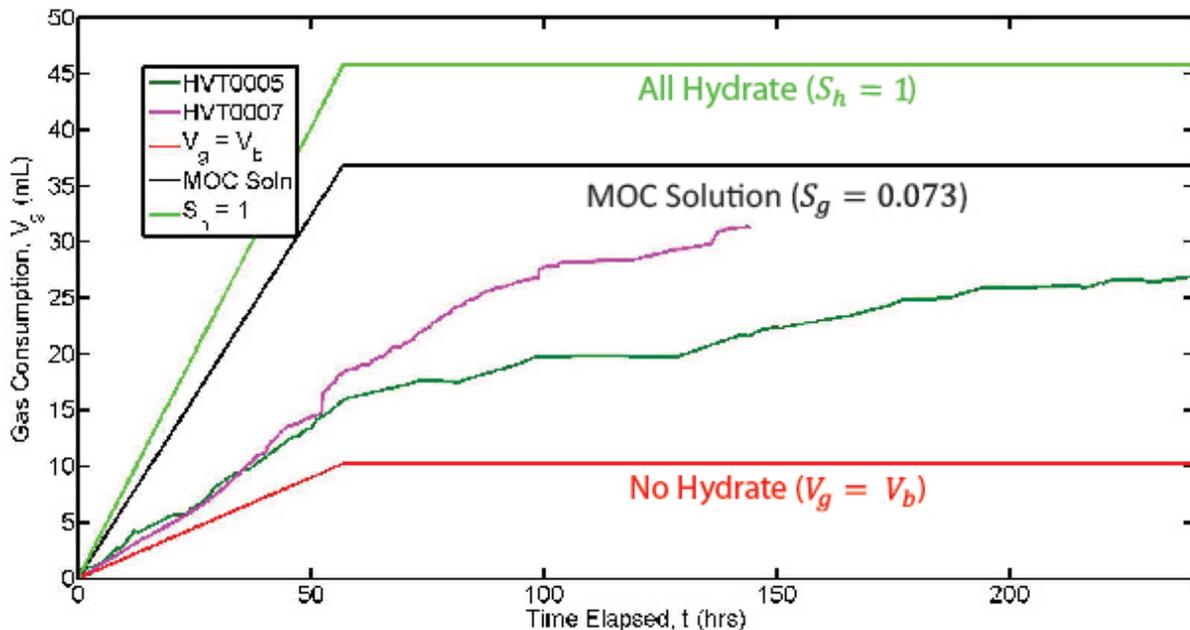
Figure 49: Comparison of gas consumption data for hydrate formation front experiments HVT0005 (dark green line) and HVT0007 (purple line). Red line indicates the MOC solution for a gas flooding experiment and indicates the minimum gas consumption needed to maintain volume balance. Black line indicates the gas consumption predicted from the MOC solution for these experiments calculated at the experimental temperature and pressure conditions. Green line indicates the maximum potential gas consumption assuming that all the space made available through water withdrawal is occupied by hydrate.

B2. Subtask 6.2 - Gas invasion from melting hydrate into water saturated HSZ

B2.1. Goal:

The Recipient shall perform an experiment analogous to Subtask 6.1 except that the gas source is not external, but rather from dissociated hydrate. The hydrate is established in the upper third of the column using methods of Task 4. Then the lower two thirds of the column are held within the hydrate stability zone while the upper third is warmed to dissociate the hydrate. Valves at the top of the column are closed so that gas from the dissociated hydrate moves downward into the hydrate stability zone. This shall enable observation of the feedback between pressure buildup and dissipation as hydrate dissociates in the top of the column and re-forms in the bottom of the column, and of the possibility that the all the hydrate re-forms lower in the column. As in Task 6.1, this geometry is inverted compared to natural systems but results in a better-controlled gas front. As time allows, the natural geometry may be attempted upon consideration of mineral grain size, capillary, dissociation rate, and gravitational forces to investigate differences.

B2.2. Activities Phase 2:

We performed dissociation experiments at the end of experiments HVT0007 and HVT0008 by depressurizing the experimental vessel containing methane hydrate. The goal of these experiments was to quantify the amount of methane in the sample, as well as characterize the dissociation behavior and

thermodynamic state of the methane hydrate. These experiments were performed by a stepwise depressurization of synthesized methane hydrate and releasing small volumes into an inverted graduated cylinder (Figure 50). A ball valve at the outlet of the experimental vessel was opened at each step to release gas to a needle valve, and then the ball valve was closed. The needle valve was then opened to release methane into the inverted cylinder. During the early stages of depressurization (high pressure) of HVT0007 some liquid was also produced in addition to gas. Before HVT0008 a secondary ball valve was added 7 cm above the outlet valve to allow for a smaller volume of gas to be produced (Figure 50). The modified setup in HVT0008 stopped the release of liquid and decreased the volume of gas in the first high pressure steps from over 200 mL to 20 mL. Once the pressure had decreased to less than 500 psi, the secondary ball valve was left open and gas was released from the experimental vessel to the needle valve, producing around 50 mL of gas with no liquid release.

The two dissociation experiments were performed over a period of 1-2 weeks with the temperature held constant at 1 deg C as in the hydration formation experiments. The cumulative methane recovery and pressure drop were recorded (Figure 51). Moles of methane recovered were calculated using the density and molecular weight of methane.

In plotting the cumulative gas recovery (in mL or mol) versus pressure (Fig. 51), we identified three regimes of methane release from the experimental vessel: (1) a high pressure release of free gas (2) dissociation of methane hydrate and (3) residual free gas after dissociation. Within the free gas regime there is a steady drop in pressure with each release of methane. In both HVT0007 and HVT0008 additional drops in pressure occurred overnight when the outlet valve was closed, suggesting possible formation of hydrate. During dissociation there is a recovery in pressure after each time the outlet valve is opened and methane released, indicating a continued dissociation and buildup of gas in the vessel.

Hydrate dissociation occurs between 3.3 and 2.8 Mpa, which corresponds to the 6 wt.% NaBr three-phase boundary and freshwater boundary. Because the starting brine is 7 wt.% NaBr, we interpret this dissociation path as due to possible localized freshening around dissociating hydrate.

There is good agreement when comparing the total moles of gas recovered during depressurization to the total moles consumed during hydrate formation (Fig. 52). When comparing the relative number of moles of methane as free gas or hydrate, the depressurization experiments underestimate the amount of hydrate and overestimate free gas relative to the synthesis experiment. These results suggest that this method of depressurization is accurate for determining the total amount of methane within a pressure core.
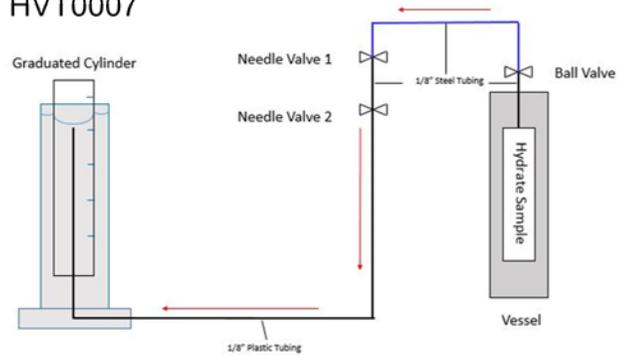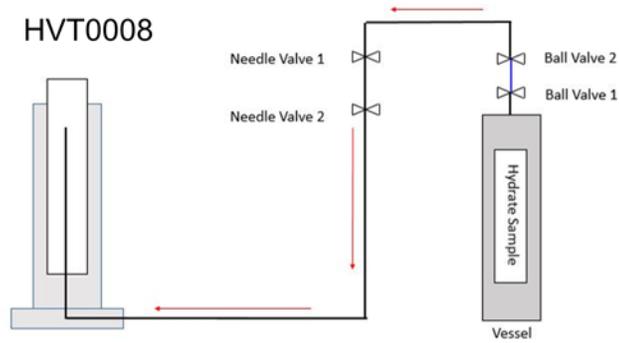
Figure 50: Experimental setup used during depressurization of HVT0007 (top) and HVT0008 (bottom).
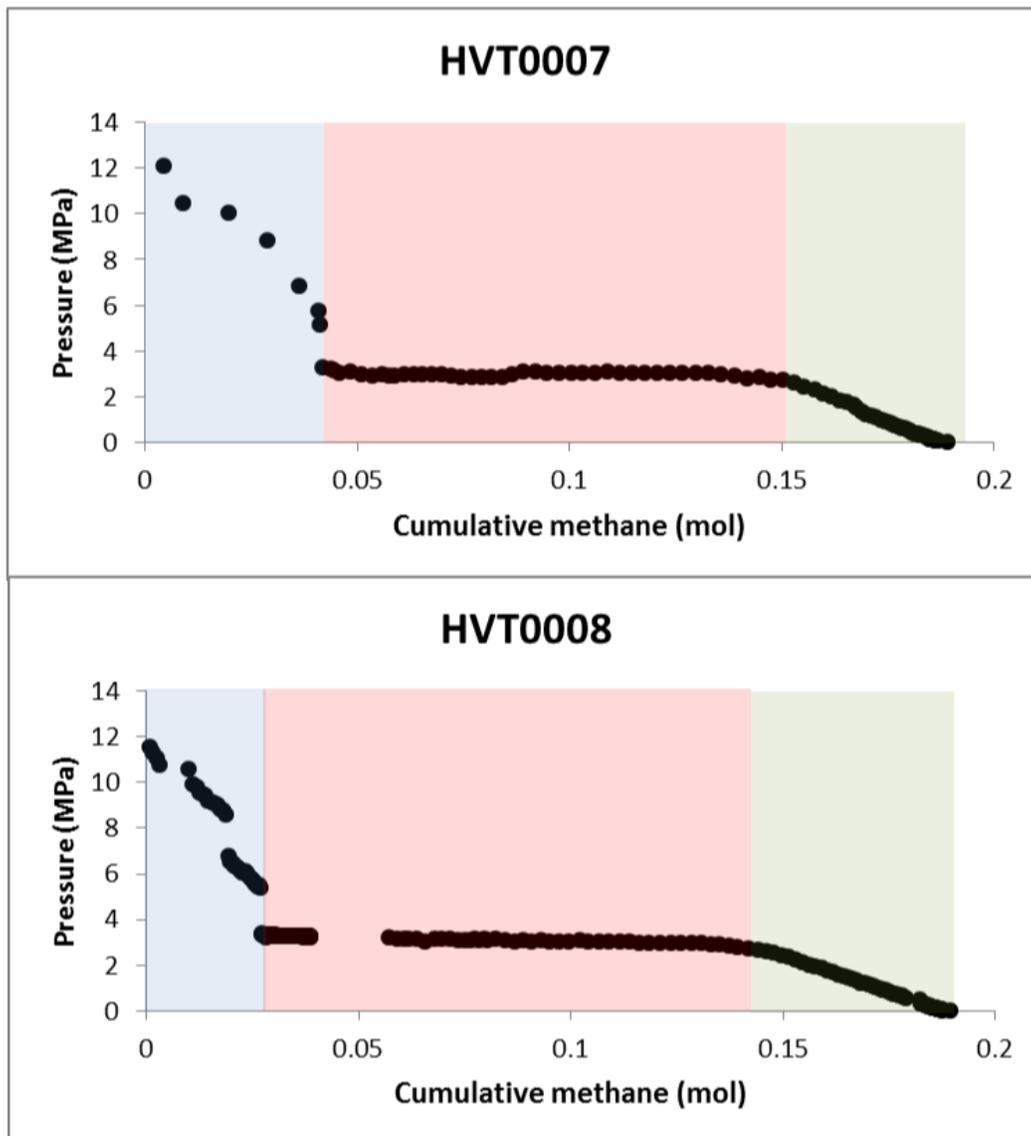
Figure 51: Outlet pressure versus cumulative volume and moles of methane released during depressurization of HVT0007 (top) and HVT0008 (bottom). Blue shaded area: high pressure free gas, red shaded area: hydrate dissociation, green shaded area: residual free gas.
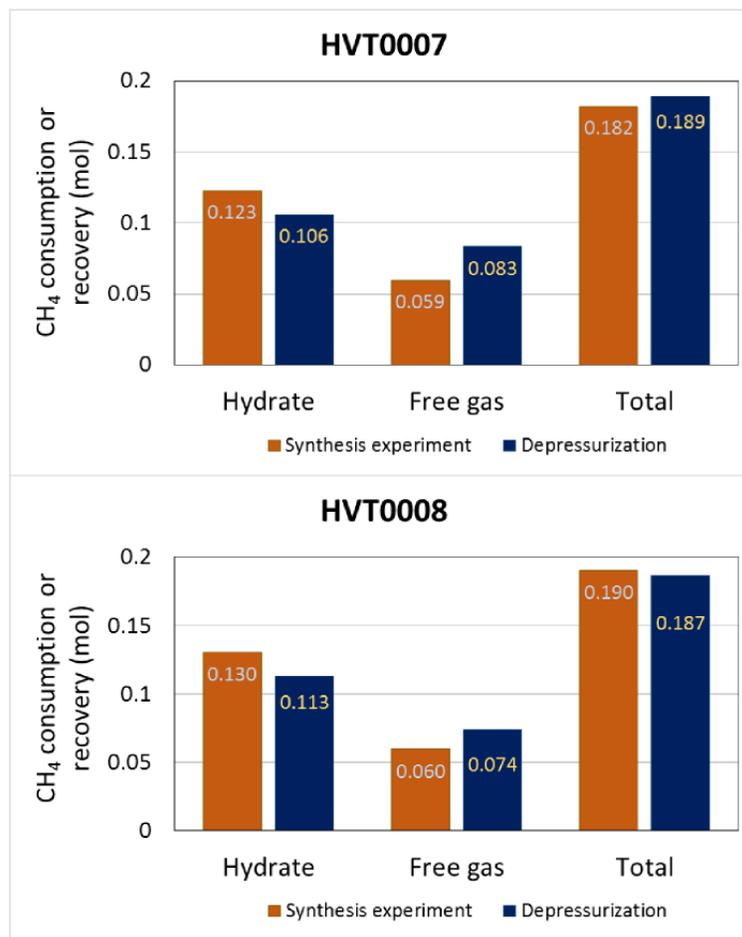
Figure 52: Comparison of total methane, hydrate and free gas between depressurization and synthesis experiments for HVT0007 (top) and HVT0008 (bottom).

2.4. Task 7: 2D model

Milestone 2.D Demonstrate a 2D simulation of hydrate dissociation and gas expulsion.

A. Goal:

The Recipient shall extend the models developed in Tasks 2 and 5 to account for structure, primarily the effect of dip of the hydrate-bearing sediment layer and of the geometry of the hydrate accumulation. In addition the Recipient shall consider the effect of two-dimensional geometry on the local perturbation of the hydrate stability zone (e.g. the effects of lateral flow of salt and heat). The Recipient shall include the effect of heat of formation and fracture permeability.

B. Activities Phase 2:

We extended our 1D hydrate dissociation model to 2D, which takes into account both the lateral and vertical heat flow and mass transport. We set the lateral boundaries to be no flow. We introduced high permeability layers interbedded in low permeability matrix. These high permeability layers could be permeable sand layers or fractures. Hydrate preferentially forms in high permeability layers. In order to simulate the sloping seafloor and the corresponding sloping base of the hydrate stability zone, we introduced coordination transformation into the numerical model. We rotated the x axis clockwise from the horizontal direction to be parallel with the sloping seafloor, and the y axis from the vertical direction to be perpendicular with the sloping seafloor. Example simulations are given below.

C. Subtask 7.1 - Hydrate dissociation in 2D systems

C1. Goal:

The Recipient shall extend the 1D dissociation model to allow for phase transport laterally as well as vertically. The boundary conditions shall be general. A constant heat flux shall be applied from below and initial distribution of hydrate gas saturation shall be assumed. A temperature perturbation shall be applied to the upper boundary.

C2. Activities Phase 2:

We have extended the 1D dissociation model to allow for phase transport both laterally and vertically, and both temperature and pressure perturbation can be applied to the upper boundary (See Subtask 7.3).

D. Subtask 7.2 - Gas expulsion in 2D systems

D1. Goal:

The Recipient shall develop 2‐dimensional models of gas venting through the gas hydrate stability zone. A localized gas flux shall be applied from below. Gas shall propagate upwards forming a three‐phase stability zone. Heat and salt shall be generated as hydrate solidifies. These shall dissipate both laterally and vertically. The Recipient shall vary both gas and water flux and determine under what conditions the gas will solidify and not breakthrough the seafloor vs. under what conditions it will propagate to the seafloor.

D2. Activities Phase 2:

In this section, we present a two-dimensional numerical simulation of gas invasion and hydrate formation in a dipping layer with high-permeability interbedded with low-permeability matrix (Figure 53). This high-permeability layer could be either sand layer or fracture zone. This setting is typical in Northern Gulf of Mexico hydrate regions, where gas migration is regionally heterogeneous and focuses into discrete high-flux pathways (Boswell et al., 2012). The dip angle of the sand layer is 14°. We set the

permeability in the low permeability layer to be 1×10^{-18} m^2, and that in the high permeability layer to be 1×10^{-13} m^2.

We use the field parameters at Walker Ridge 313 to describe this system. The water depth is 2000 m (McConnell and Kendall, 2002). The initial pressure increases linearly downward from sea floor with hydrostatic pressure gradient (10 KPa/m) (Figure 54a). Temperature at seafloor is 4 ^{o}C, and increases downward with a geothermal gradient of 18 ^{o}C/km (Figure 54b) (McConnell and Kendall, 2002). There is 100% brine with salinity of 3 wt.% initially in the domain (Figure 54c, 54d). This makes the base of the hydrate stability zone to be between 900 and 950 mbsf (meter below seafloor) (McConnell and Kendall, 2002). We investigate the domain from 550 to 1000 mbsf, with a lateral distance of 900 m. We fix the pressure to be 25.77 MPa, temperature 13.9 °C, and salinity 3 wt.% at the top boundary (550 mbsf). We apply a fixed geothermal flux of 20.71 mW/m^2 at the bottom boundary (1000 mbsf). We supply methane gas from the bottom of the sand layer (Figure 53) with a high rate of 0.5 kg/(m^2 yr) (Liu and Flemings, 2007). We set the other boundaries to be no flow (Figure 53).

Hydrate forms from the base of the hydrate stability zone when gas enters there (Figure 55a). It increases the local salinity and bring the local system to three-phase equilibrium (Figure 55b, 55c), at which point no more hydrate can form. Hydrate formation releases heat and increases the local and surrounding temperature by heat conduction and advection (Figure 55d). This temperature increase melts the hydrate formed at the base of the hydrate stability zone (Figure 56), and moves the base of the hydrate stability zone to a shallower depth (Figure 57). Gas front and hydrate solidification front move together along the sand layer, horizontally from left to right and vertically toward seafloor (Figures 56, 57 and 58). At 100.122 k.y., the entire sand layer within the hydrate stability zone is at three-phase equilibrium, and hydrate coexists with methane gas and liquid brine with elevated salinities (Figure 58).

Hydrate saturation increases vertically toward seafloor (Figure 58). That is because as we move toward seafloor, the system initial thermal condition moves father away from the phase boundaries, and more hydrate is required to form to reach three-phase equilibrium. Hydrate saturation decreases horizontally from left to right (Figure 58). That is because salt advection and diffusion from hydrate solidification front increases the salinity on the right, and moves the local thermal condition toward phase boundaries. As time goes on, salt diffuses away from the sand layer, more hydrate is required to form to maintain three-phase equilibrium salinity, and hydrate saturation increases with time at a fixed spatial position (Figures 55, 56, 57 and 58). In a same horizontal sand layer, gas saturation is highest on the right (Figure 58). That is because hydrate saturation increases vertically toward seafloor, which decreases the intrinsic permeability and increases the capillary entry pressure.

Water flows horizontally from right to left and vertically downward in the sand layer (Figure 59a). Hydrate formation leads to volume expansion, increases the local pressure, and drives water to flow away from the hydrate solidification front (Figure 59a). Gas intrusion and hydrate formation in the sand layer drives water to flow away from the sand layer (Figure 59a). Water velocity above the sand layer is greater than that below the sand layer. This can be explained by two reasons: first, pressure increase in the sand layer increases the pressure gradient above the sand layer while decreases the pressure gradient below the sand layer; second, we have an open boundary at the top and a closed boundary at the bottom. This leads to greater increase of salinity above the sand layer than that below the sand layer (Figure 57c and 58c). Gas flows horizontally from left to right and vertically toward seafloor (Figure 59b). Gas flow velocity is zero in the clay layer (Figure 59b).
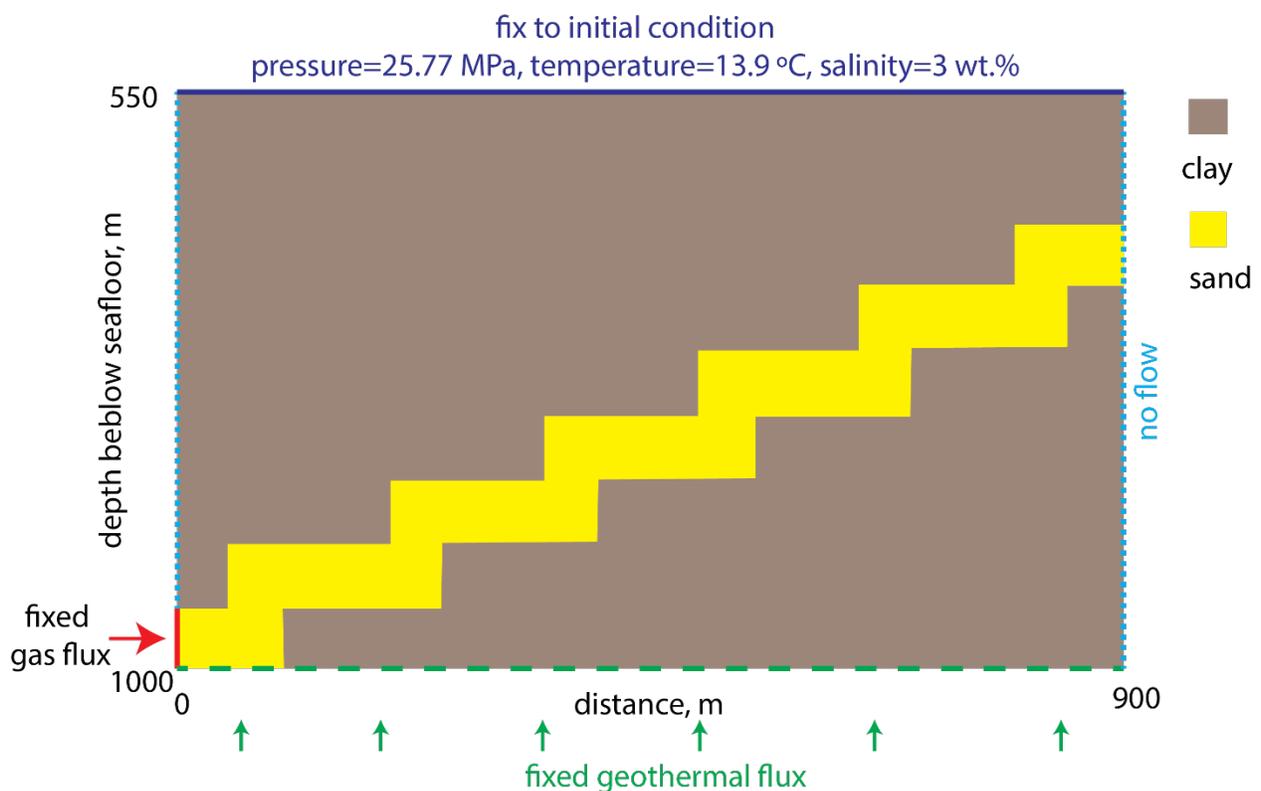
Figure 53: Schematic diagram of the simulated domain. A dipping sand layer (permeability of 1×10⁻¹³ m²) is interbedded within a low permeability clay layer (permeability of 1×10⁻¹⁸ m²). The dip angle of the sand layer is 14º. Hydrate stability zone extends from seafloor to between 900 and 950 meter below seafloor. Methane gas flows into the domain from the base of the sand layer with a fixed rate.
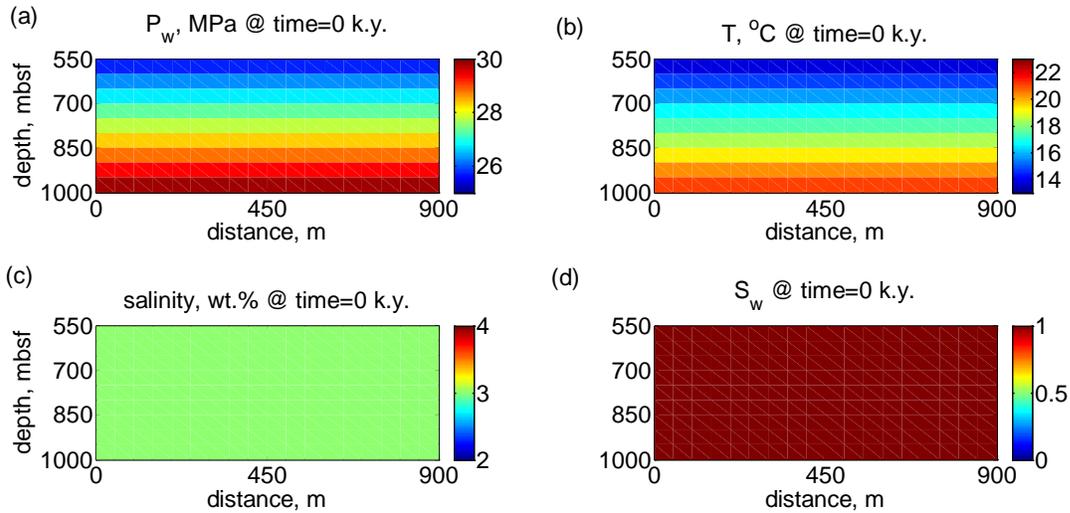
Figure 54: The initial (a) pressure, (b) temperature, (c) salinity and (d) water saturation in the domain.
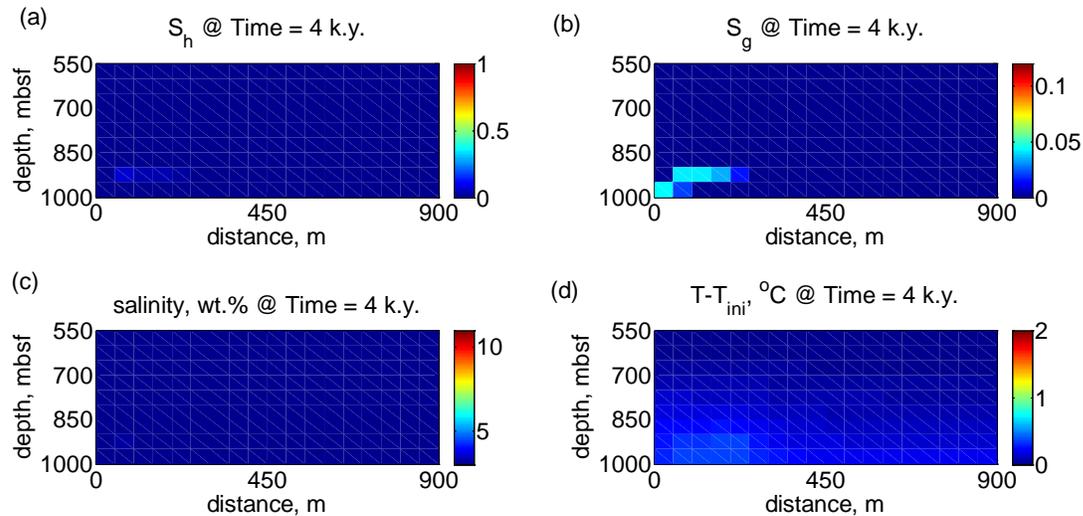
Figure 55: (a) hydrate saturation, (b) gas saturation, (c) salinity, and (d) temperature change from initial at 4 k.y..
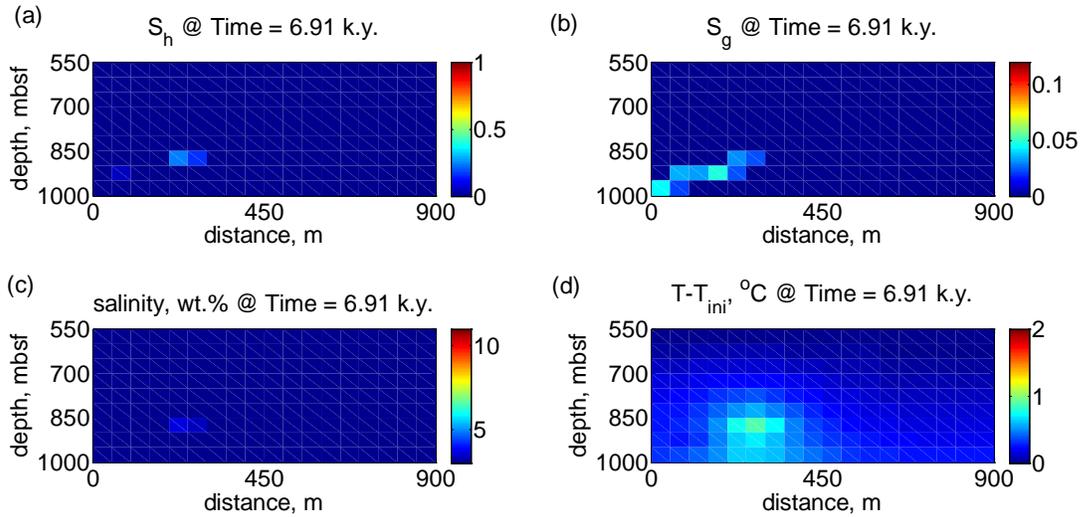
Figure 56: (a) hydrate saturation, (b) gas saturation, (c) salinity, and (d) temperature change from initial at 6.91 k.y..
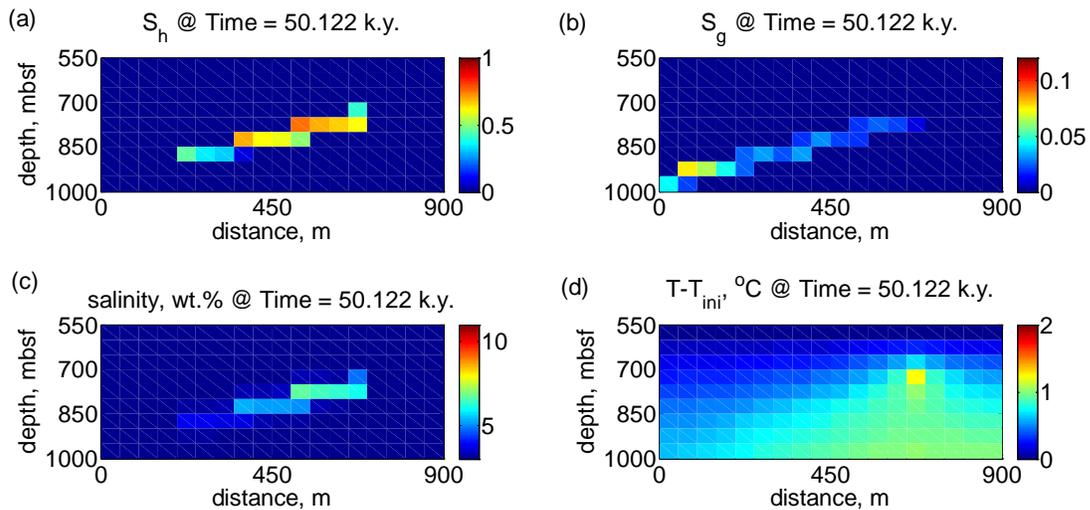
Figure 57: (a) hydrate saturation, (b) gas saturation, (c) salinity, and (d) temperature change from initial at 50.122 k.y..
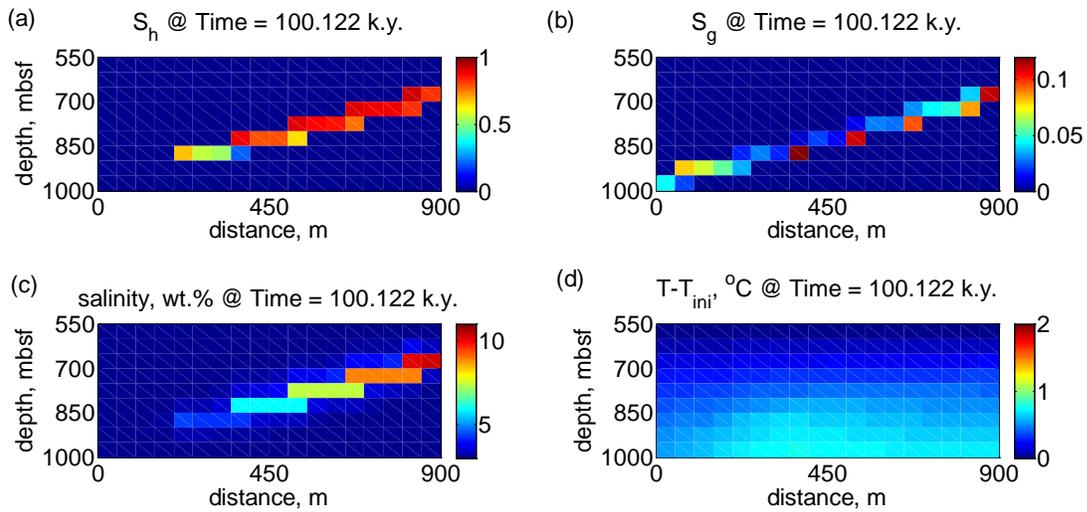
Figure 58: (a) hydrate saturation, (b) gas saturation, (c) salinity, and (d) temperature change from initial at 100.122 k.y..
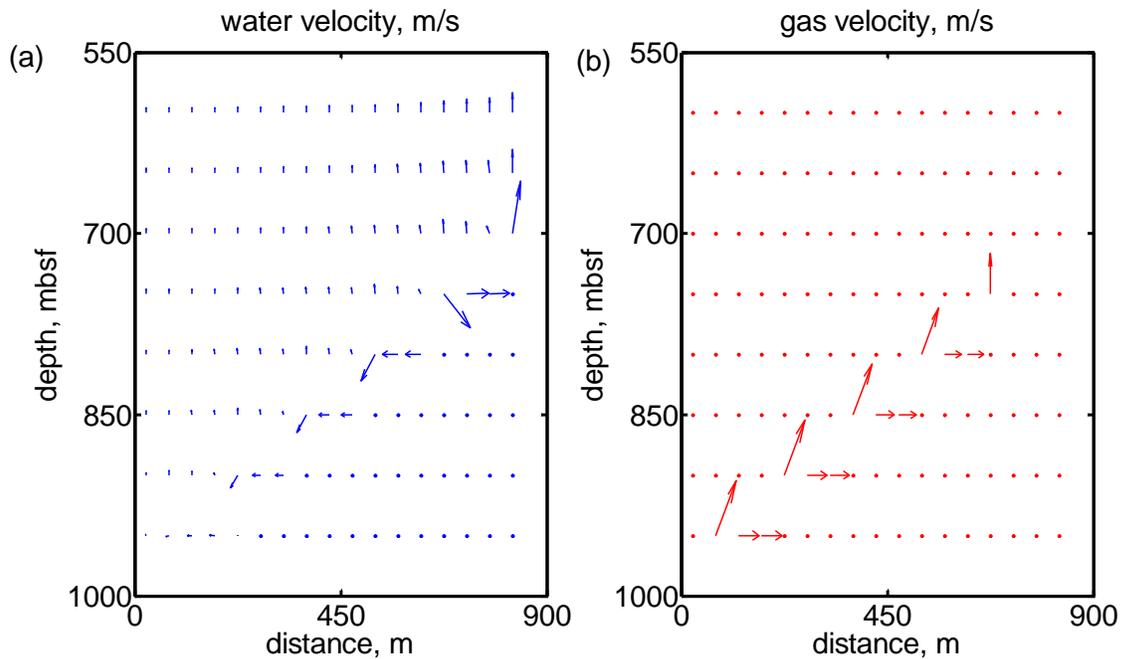
Figure 59: (a) water velocity, and (b) gas velocity field at 50.122 k.y..

E. Subtask 7.3 - Apply 2D, gas expulsion model to natural examples

F. Subtask 7.3.1 Pleistocene to Holocene Sea level rise

F1. Goal:

The Recipient shall simulate the impact of sea‐level rise during the Holocene sea level rise (e.g. 20,000 years ago). In this scenario 4 degree centigrade seawater abruptly floods a previously sub‐aerially exposed continental margin. The Recipient shall consider reservoirs both within the three phase stability zone and those that are within the two phase (L+H) region. The thermal and pressure effect of this response over the Holocene shall be simulated. A key question to be addressed is under what conditions will gas migrate through the hydrate stability zone vs. when will it just migrate laterally to be vented at the seaward limit of the stability zone.

F2. Activities Phase 2:

Arctic Ocean continental shelf (AOCS) are undergoing the most dramatic warming associated with the transgression of sea level since the end of the last ice age (Paull et al., 2011). The degradation of subsea permafrost and the consequent destabilization of methane hydrate can significantly increase the flux of methane to the atmosphere and accelerates global warming (Rachold et al., 2007).

We investigated how the carbon budget at the water depth of 110-120 m of North America Beaufort shelf responds to the dramatic changes on the AOCS. At 12 k.y. before present, pressure increased with a hydrostatic pressure gradient (11.03 KPa/m) from ground surface (Collett et al., 2011) (Figure 60a). The entire area between water depths of 110 and120 m was exposed to -13 °C Arctic air (Frederick and Buffett, 2014) (Figure 60b). Permafrost with a uniform ice saturation of 90% developed from ground surface to about 400 m below surface with a temperature gradient of 31.9 °C/km (Collett et al., 2011) (Figure 60b, c). Below the base of permafrost, temperature increased linearly with a gradient of 45 °C/km (Collett et al., 2011) (Figure 60b). We set the salinity below the permafrost to be homogeneously 0.9 wt.% (Collett et al., 2011), which rendered a hydrate stability zone from 250 to 600 m below ground surface (Figure 60d). We set two hydrate layers initially below the base of permafrost with a saturation of 80%: 450-500 m and 550-600 m, which were separated by a less permeable layer with an intrinsic permeability of 10-16 m2 (Figure 60c). The hydrate system at the lower layer (550-600 m) was very close to the hydrate phase boundary (Figure 60d).

At 12 k.y. before present, we imposed a sea level rise at the water depth of 120 m with a rate of 0.01 m/year (Frederick and Buffett, 2014). Sea water with bottom temperature of 0 °C would cover the entire simulated area, water depth of 110-120 m, within 1 k.y.. The ground surface temperature was immediately increased from -13 to 0 °C, and the ground surface salinity was immediately decreased to 3 wt.% when it was flooded by sea water. The pressure at ground surface increased linearly with sea level rising. We fixed the geothermal flux at the bottom of the domain (700 m) to be 55.9 mW/m2.

Temperature increases from ground surface, and from deeper to shallower water depth (Figure 61a). This induced ice melting from ground surface and from 120 m water depth (Figure 61c). The endothermic nature of ice thawing greatly buffered heat transfer to depth. Therefore, there was no temperature increase below the base of the permafrost until 9.6 k.y. before present (Figure 61a). At the same time, sea level rise increased the water pressure rapidly in the entire depth, with a greater magnitude at the depth below the base of permafrost (Figure 61b). This made the hydrate system more stable with time before 9.6 k.y. before present. Continuing warming from the top and geothermal flux from the bottom melted the ice from both the ground surface and the base of permafrost (Figure 61c). Temperature in the hydrate layers started to increase after 9.6 k.y. before present (Figure 61a). However, the rising sea level continuously increased the pressure in the hydrate layers (Figure 61b). Therefore, the distances of the hydrate layers toward the phase boundaries remained unchanged, and no methane gas was released until 1.1 k.y. before present. However, the volume of the ice has decreased by 73% (Figure 61c).
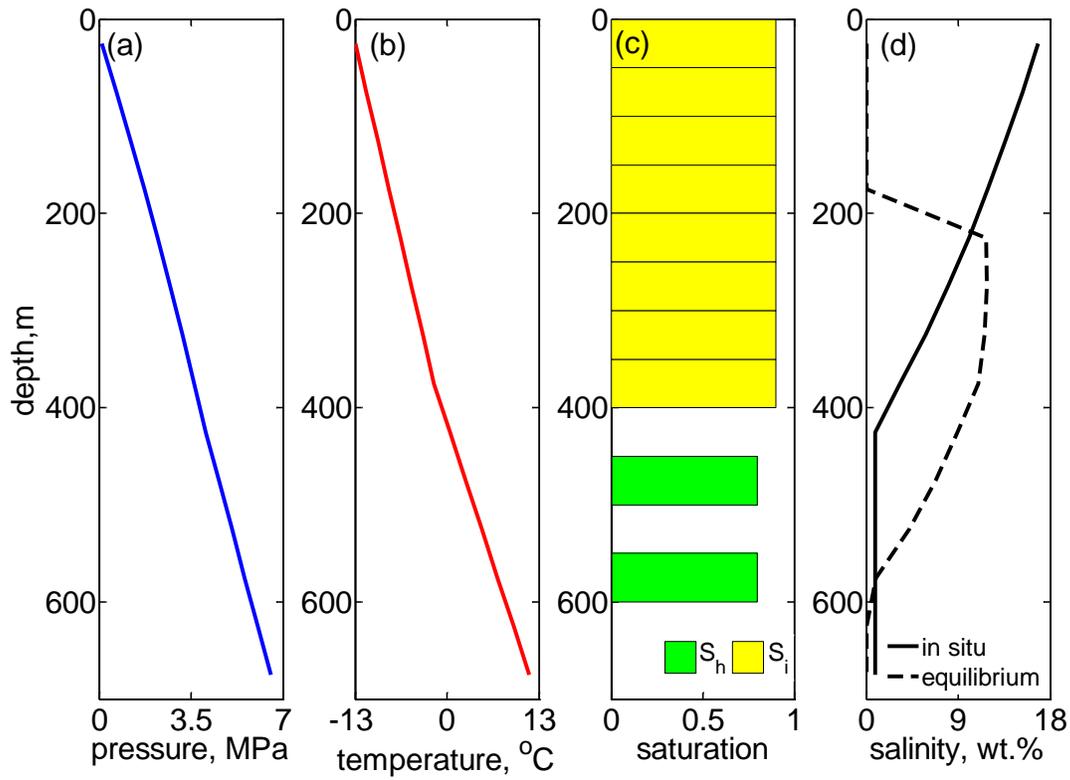
Figure 60: The (a) pressure, (b) temperature, (c) ice (yellow) and hydrate (green) saturations, and (d) in situ (solid line) and three-phase equilibrium (dashed line) salinity distribution at the water depth of 110-120 m on North America Beaufort shelf at 12 k.y. before present (Collett et al., 2011; Frederick and Buffett, 2014). We assumed lateral homogeneous condition.
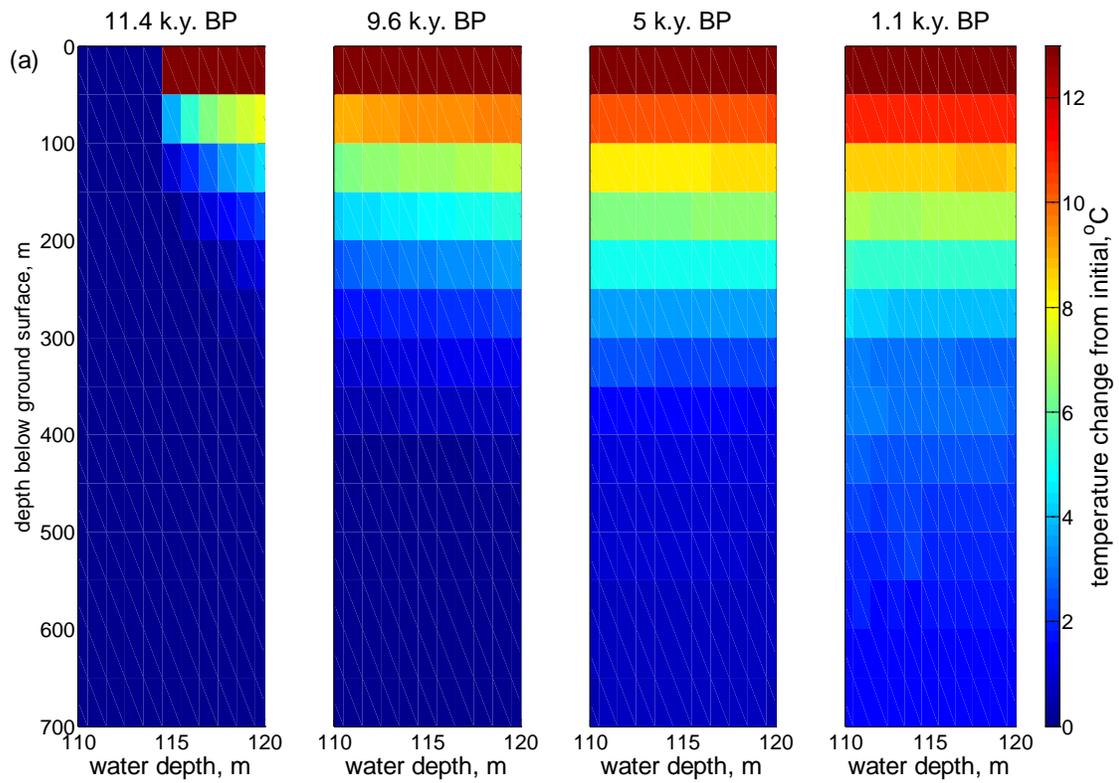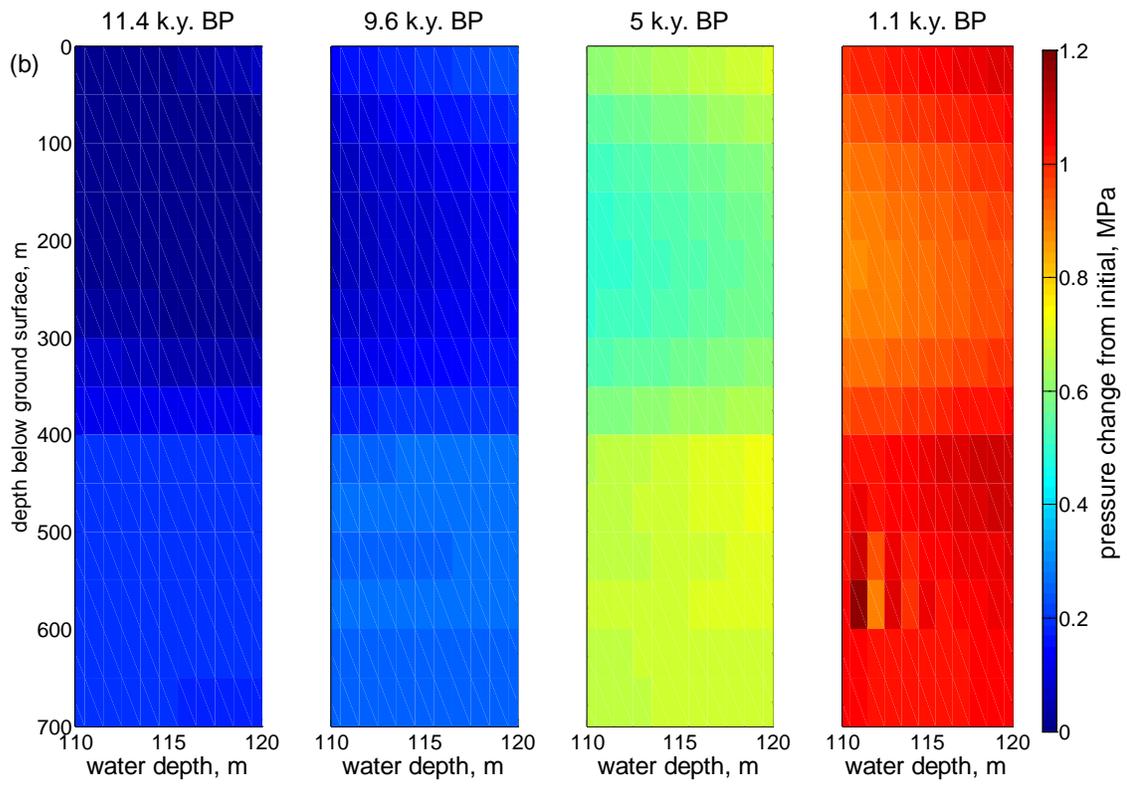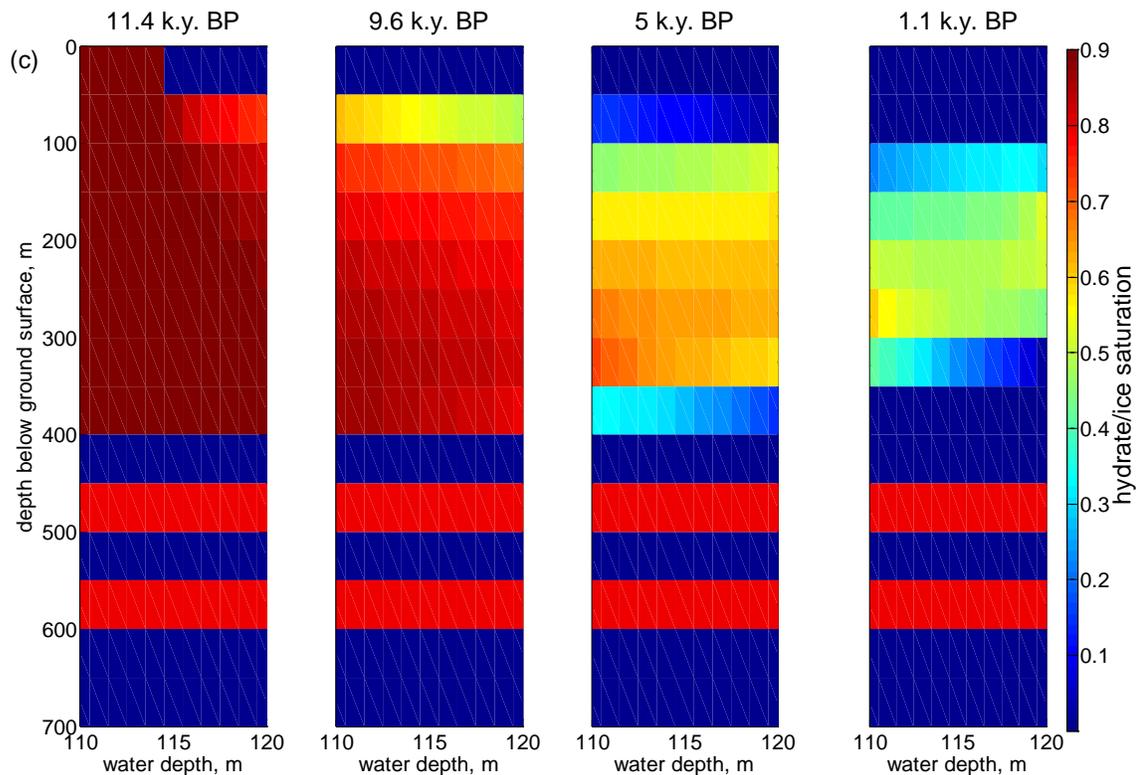
Figure 61: (a) Temperature change from initial, (b) pressure change from initial, and (c) ice (0-400 m) and hydrate (450-500 m, and 550-600 m) saturation at 11.4, 9.6, 5 and 1.1 k.y. before present.

G. Subtask 7.3.2 - Recent warming

G1. Goal:

The Recipient shall simulate the impact of increasing bottom water temperature over the 100 year time scale. The effects of 1 degree per year and 3 degree per year shall be considered. The Recipient shall simulate the continental margin at the up-dip limit of the stability zone and shall consider reservoirs both within the three phase stability zone and those that are within the two phase (L+H) region.

G2. Activities Phase 2:

Under current climate conditions and a 1%/yr increase in atmospheric CO_2, the temperature at the seafloor would rise by 1 °C over the next 100 yr, and possibly by another 3 °C in the following century (Reagan and Moridis, 2009). We investigate the hydrate melting and gas expulsion during seafloor warming in an Arctic Ocean which extends from seafloor to 260 mbsf (meters below seafloor), and

laterally from the water depth of 270 to 360 m (Reagan and Moridis, 2009). The seafloor has a slope of 30 degree. The upper boundary (seafloor) is an open boundary. The pressure at the upper boundary is variable with the water depth, but fixed with time. We fix the geothermal flux at the lower boundary to be 28.3 W/m^2. The initial salinity is uniformly 3 wt.% (Reagan and Moridis, 2009). The initial pressure in the sediment increases with depth with a hydrostatic pressure gradient. The initial temperature increases with depth with a geothermal gradient of 0.03 ^{o}C/m and seafloor temperature of 0 ^{o}C (Frederick and Buffett, 2014). These yield a hydrate stability zone in the sediment between the water depth of 290 and 360 m. Initially, there is a 10% hydrate saturation from the base of the hydrate stability zone (BHSZ) to 104 m above the BHSZ (Figure 62a).

We investigated the hydrate melting and gas expulsion in two scenarios of seafloor warming. In Case-1, we increase the seafloor temperature from 0 to 1 ^{o}C at time zero, and then keep this 1 ^{o}C seafloor temperature for the remaining time. Hydrate starts to melt from both the top and bottom of the hydrate deposits from the shallowest water depth with hydrate (Figure 62b). The gas released from the top of the hydrate deposit migrates both vertically upward toward the seafloor and laterally up the slope, and vents at the seafloor both directly above the melting hydrate and up the slope (Figure 63b). The gas released from the bottom of the hydrate deposits preferentially migrates up the slope where the sediment permeability is larger than that in the hydrate deposits and where the hydrate is unstable (Figure 63b). Secondary hydrate forms vertically above the base of the hydrate deposits, but with a less amount compared with the 1D model. That is because most of the gas released from the base of the hydrate deposits escaped up the slope, and vents at the seafloor. The gas venting area extends to the deeper water depth at the seafloor, as the hydrate there starts to melt from the base (Figures 62 and 63). Hydrate disappears from both the shallow water depth and the base of the entire deposits (Figure 62). At steady-state temperature (20 k. y.), the hydrate stability zone retreats to the water depth of 320 m (Fig. 62d). There are still a 17 to 50 m thick hydrate deposit at the base of the hydrate stability zone, which thins toward the shallower water depth (Figure 62d). Residual gas is present below the BHSZ and at water depth shallower than 320 m (Figure 63d).

In Case-2, we increase the seafloor temperature from 0 to 3 ^{o}C linearly in 300 years, and then keep this 3 ^{o}C seafloor temperature for the remaining time. The system behaves similarly as in Case-1, except that the hydrate melts and gas vents at much greater rates (Figure 64). The system reaches steady-state temperature at 12 k.y.., when the hydrate stability zone retreats to the water depth greater than 360 m, and the entire hydrate deposit disappears.
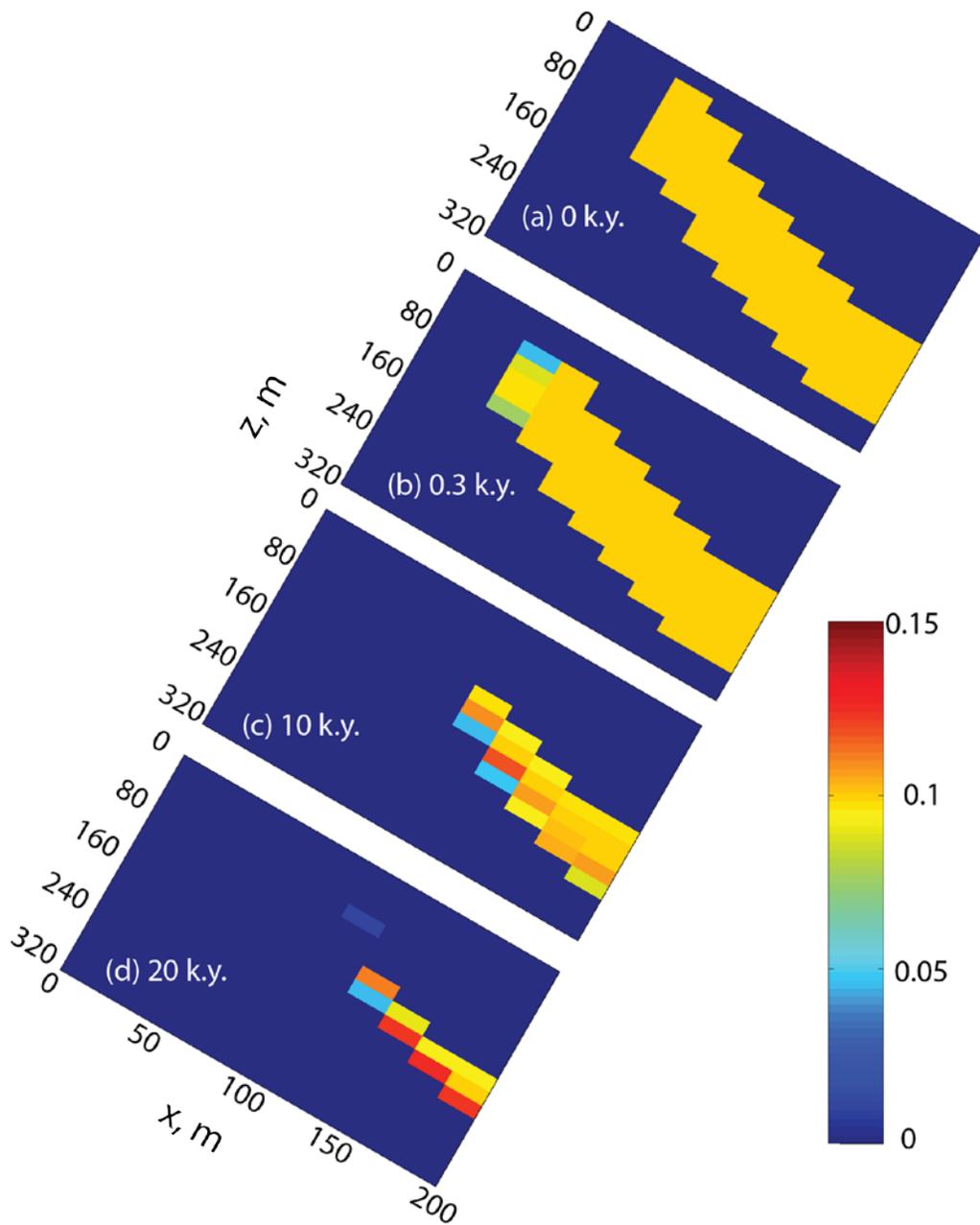
Figure 62: Case-1: hydrate saturation distribution at 0, 0.3, 10 and 20 k.y., respectively.
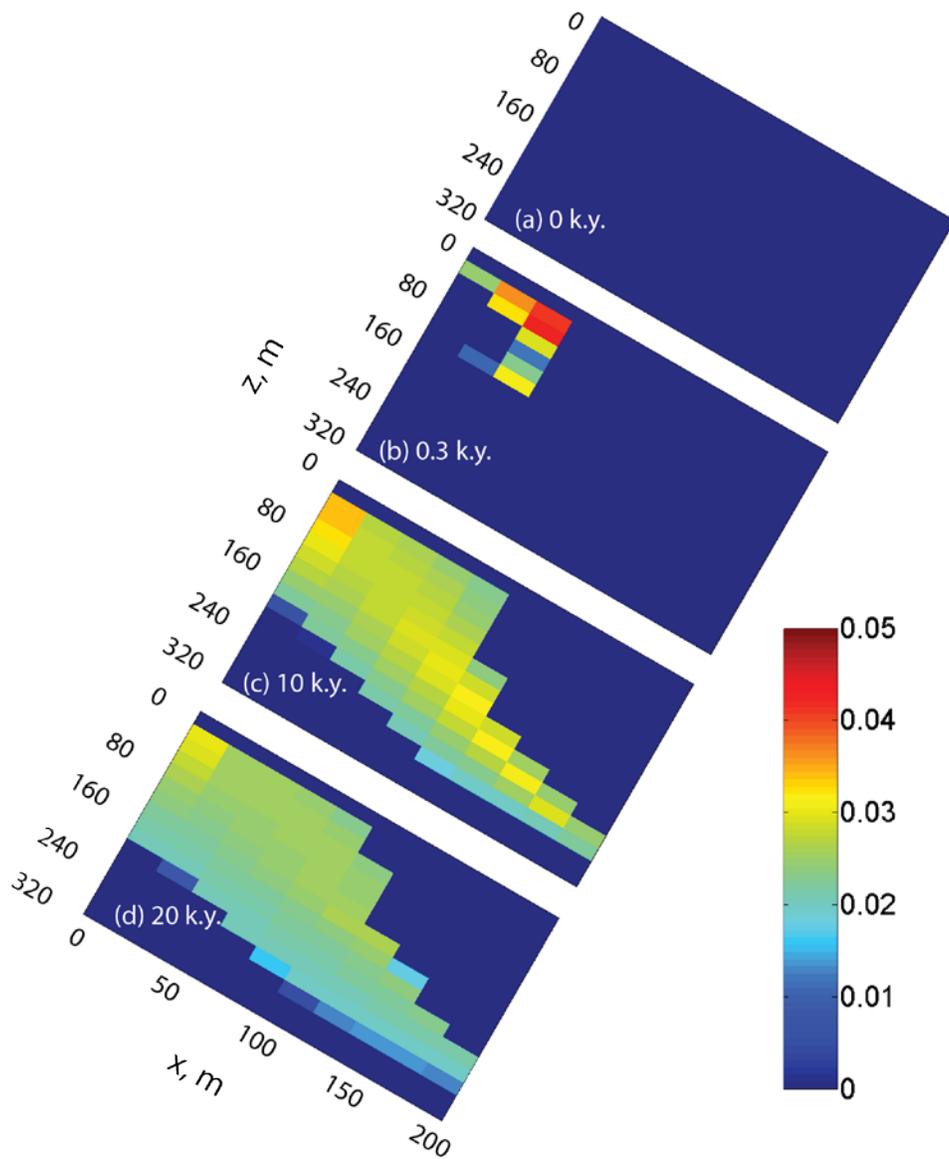
Figure 63: Case-1: gas saturation distribution at 0, 0.3, 10 and 20 k.y., respectively.
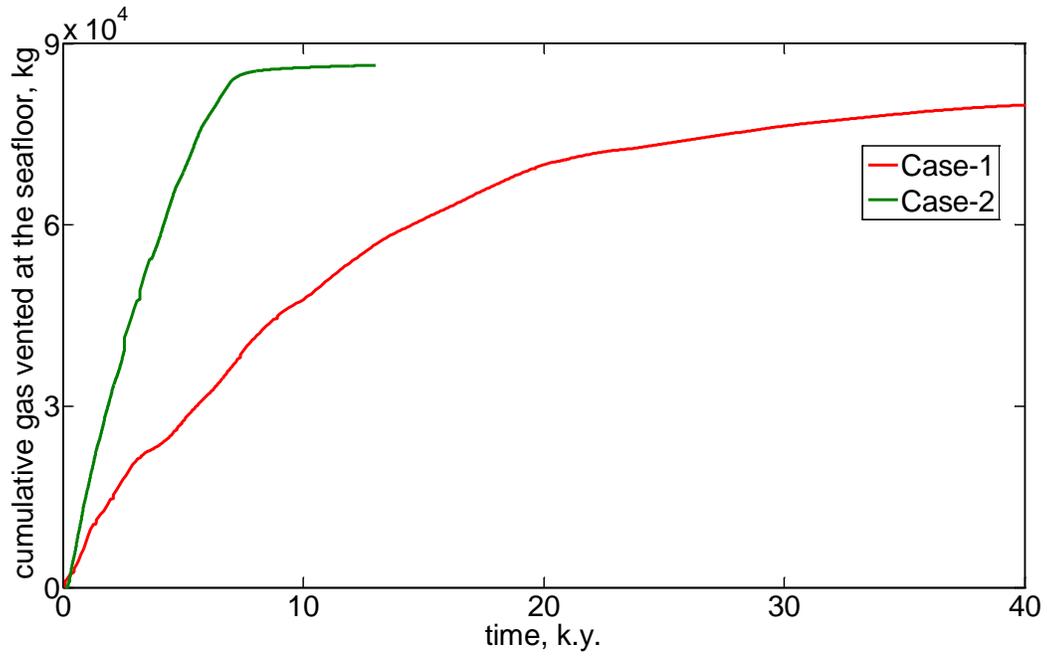
Figure 64: change of cumulative gas vented at the seafloor with time for Case-1 (red line) and Case-2 (green line), respectively.

3. Nomenclature Table

G	Free gas phase
H	Hydrate phase
L	Liquid phase
u	Pore pressure (MPa)
ρ_{sw}	Seawater Density (g/cm^3)
ρ_{pw}	Pore water density (g/cm^3)
ρ_f	Fluid density (g/cm^3)
ρ_b	Bulk density (g/cm^3)
ρ_m	Grain density (g/cm^3)
Z_{wd}	Water depth (m)
ΔZ	Depth within the GHSZ (m)
Z	GHSZ thickness (m)
g	Gravitational acceleration (m/s^2)
T_f	Formation temperature (ºC)
T_b	Seafloor temperature (ºC)
G_g	Geothermal gradient (ºC/km)
S_h	Hydrate saturation (dimensionless)
S_w	Water saturation (dimensionless)
$C_{in\text{-}situ}$	In-situ salinity (dimensionless)
C_0	Core-derived salinity (dimensionless)
C	Salinity (dimensionless)
N	Saturation exponent (dimensionless)
a	Tortuosity coefficient (dimensionless)
m	Cementation exponent (dimensionless)
n	Porosity (dimensionless)
ρ_w	Fluid resistivity (Ωm)
ρ_t	Formation resistivity (Ωm)
F	Formation factor (dimensionless)
M_g	gas molecular mass (g/mol)
M_h	hydrate molecular mass (g/mol)
M_w	water molecular mass (g/mol)

ΔS_g	change in gas saturation (V/V)
ΔS_h	change in hydrate saturation (V/V)
ΔS_w	change in water saturation (V/V)
ΔW	change in water mass (g)
ΔM	change in methane mass (g)
L	sample length (cm)
L_f	length of hydrate formation zone (cm)
V_{TOT}	total sample volume (mL)

MOC model

<u>Superscript</u>

a	downstream side of the leading shock
b	upstream side of the leading shock
c	downstream side of the trailing shock
d	upstream side of the leading shock
e	a position between the downstream side of the trailing shock and upstream side of leading shock

<u>Subscript</u>

B	the component of brine
M	the component of methane
W	the component of pure water
g	gas phase
h	hydrate phase
l	liquid water phase
β	phase index
κ	component index

<u>Variables</u>

cl_0	initial salinity (wt.%)

cl_e salinity at three phase equilibrium (wt.%)

D_s effective molecular diffusion coefficient of salt in sediment (m^2 s^{-1})

D_{s0} molecular diffusion coefficient of salt in free water (m^2 s^{-1})

f_g fractional flow of gas phase (dimensionless)

f_l fractional flow of liquid water phase (dimensionless)

g acceleration due to gravity (m sec^{-2})

G_β overall dimensionless concentration of component β

H_β overall dimensionless flux of component β

k sediment intrinsic permeability (m^2)

k_0 sediment intrinsic permeability in absence of ice and hydrate (m^2)

$k_{r\beta}$ relative permeability of β phase (dimensionless)

L characteristic length (m)

L_s distance from the hydrate solidification front where salt diffusion changes the salinity (m)

P_c capillary pressure (Pa)

P_0 pressure (Pa)

q_{gi} gas injection rate (m sec^{-1})

S_β^* effective saturation of β phase (dimensionless)

S_β saturation of β phase (dimensionless)

S_{gr} residual gas phase saturation (dimensionless)

S_{wr} residual water phase saturation (dimensionless)

t time (sec)

T_0 temperature (^{o}C)

v total flux of the mobile phase (m sec^{-1})

v_D dimensionless total flux

$X_{\kappa,\beta}$ mass fraction of component κ in phase β (dimensionless)

θ dip angle of the system (rad)

ϕ porosity (dimensionless)

ρ_{lD} dimensionless density of liquid water phase

ρ_{gD} dimensionless density of gas phase

ρ_{hD} dimensionless density of hydrate phase

ρ_{β} density of β phase (kg m^{-3})

ρ_{gi} density of the injected gas (kg m^{-3})

μ_{β} dynamic viscosity of β phase (kg m^{-1} s^{-1})

λ_{β} mobility of phase β (W m^{-1} $^{\circ}$C^{-1})

τ dimensionless time

ε dimensionless distance from gas inlet

ε_0 initial dimensionless position of the composition G_{β}

Λ_{β}^{ab} dimensionless leading shock velocity calculated by the component β

Λ^{e} dimensionless composition wave velocity for gas saturation of S_g^e

Numerical model

β phase

e energy component

g gas phase

h hydrate phase

κ component

l liquid phase

m methane component

s	salt component
v	vapor phase
w	water component
C_R	heat capacity of the solid grain (J kg^{-1} oC^{-1})
D_{l0}^{κ}	molecular diffusion coefficient of component k in free water (m^2 s^{-1})
ϕ	porosity of the sediment (dimensionless)
ϕ_0	porosity in the absence of hydrate (dimensionless)
g	acceleration due to gravity (m s^{-2})
h_{β}	specific enthalpy of phase β (J kg^{-1})
k	intrinsic permeability (m^2)
k_0	permeability in the absence of hydrate (m^2)
$k_{r\beta}$	relative permeability of phase β (dimensionless)
λ	overall thermal conductivity of porous media (W m^{-1} ^{o}C^{-1})
λ_{β}	thermal conductivity of phase β (W m^{-1} ^{o}C^{-1})
λ_R	thermal conductivity of grain (W m^{-1} ^{o}C^{-1})
μ_{β}	viscosity of phase β (Pa s)
P_c	capillary pressure (Pa)
P_{c0}	capillary pressure in the absence of hydrate (Pa)
P_{β}	β phase pressure (Pa)
q^e	generation rate of energy (J m^{-3} s^{-1})
q^{κ}	generation rate of component κ (kg m^{-3} s^{-1})
ρ_{β}	density of phase β (kg m^{-3})
S_{β}	saturation of phase β (dimensionless)
T	temperature (^{o}C)
t	time (s)
u_{β}	specific internal energy of phase β (J kg^{-1})
X_{β}^{k}	mass fraction of component κ in phase β (dimensionless)

4. References

Archer, D., 2015, A model of the methane cycle, permafrost, and hydrology of the Siberian continental margin: Biogeosciences, v. 12, no. 10, p. 2953-2974.

Bader, S., and Kooi, H., 2005, Modelling of solute and water transport in semi-permeable clay membranes: comparison with experiments: Advances in Water Resources, v. 28, no. 3, p. 203-214.

Bangs, N. L. B., Hornbach, M. J., and Berndt, C., 2011, The mechanics of intermittent methane venting at South Hydrate Ridge inferred from 4D seismic surveying: Earth and Planetary Science Letters, v. 310, no. 1-2, p. 105-112.

Barbour, S. L., and Fredlund, D. G., 1989, Mechanisms of osmotic flow and volume change in clay soils: Canadian Geotechnical Journal, v. 26, no. 4, p. 551-562.

Boswell, R., Collett, T. S., Frye, M., Shedd, W., McConnell, D. R., and Shelander, D., 2012, Subsurface gas hydrates in the northern Gulf of Mexico: Marine and Petroleum Geology, v. 34, no. 1, p. 4-30.

Clennell, M. B., Hovland, M., Booth, J. S., Henry, P., and Winters, W. J., 1999, Formation of natural gas hydrates in marine sediments 1. Conceptual model of gas hydrate growth conditioned by host sediment properties: Journal of Geophysical Research, v. 104, no. B10, p. 22985-23003.

Collett, T. S., Lee, M. W., Agena, W. F., Miller, J. J., Lewis, K. A., Zyrianova, M. V., Boswell, R., and Inks, T. L., 2011, Permafrost-associated natural gas hydrate occurrences on the Alaska North Slope: Marine and Petroleum Geology, v. 28, no. 2, p. 279-294.

Daigle, H., Bangs, N. L., and Dugan, B., 2011, Transient hydraulic fracturing and gas release in methane hydrate settings: A case study from southern Hydrate Ridge: Geochemistry Geophysics Geosystems, v. 12, no. 12.

Daigle, H., and Dugan, B., 2011, Capillary controls on methane hydrate distribution and fracturing in advective systems: Geochemistry, Geophysics, Geosystems, v. 12, no. 1, p. n/a-n/a.

Dallimore, S. R., and Collett, T. S., 2005, Summary and implications of the Mallik 2002 Gas Hydrate Production Research Well Program, Scientific Results from the Mallik 2002 Gas Hydrate Production Research Well Program, Mackenzie Delta, Northwest Territories, Canada, Geological Survey of Canada, Bulletin no. 585, 2005.

Darnell, K. N., and Flemings, P. B., 2015, Transient seafloor venting on continental slopes from warming-induced methane hydrate dissociation: Geophysical Research Letters, p. n/a-n/a.

DiCarlo, D. A., Mirzaei, M., Aminzadeh, B., and Dehghanpour, H., 2012, Fractional Flow Approach to Saturation Overshoot: Transport in Porous Media, v. 91, no. 3, p. 955-971.

England, W. A., Mackenzie, A. S., Mann, D. M., and Quigley, T. M., 1987, The movement and entrapment of petroleum fluids in the subsurface: Journal of the Geological Society of London, v. 144, no. 2, p. 327-347.

Flemings, P. B., 2014a, October Quarterly Research Performance Progress Report (Period ending 9/30/2014), Controls on Methane Expulsion During Melting of Natural Melting of Natural Gas Hydrate Systems: Topic Area 2, DOE Award No.: DE-FE0010406.

-, 2014b, Phase 1 Progress Report (Period ending 3/31/2014), Controls on Methane Expulsion During Melting of Natural Melting of Natural Gas Hydrate Systems: Topic Area 2, DOE Award No.: DE-FE0010406.

-, 2015, January Quarterly Research Performance Progress Report (Period ending 12/31/2014), Controls on Methane Expulsion During Melting of Natural Melting of Natural Gas Hydrate Systems: Topic Area 2, DOE Award No.: DE-FE0010406.

Frederick, J. M., and Buffett, B. A., 2014, Taliks in relict submarine permafrost and methane hydrate deposits: Pathways for gas escape under present and future conditions: Journal of Geophysical Research: Earth Surface, v. 119, no. 2, p. 106-122.

Ginsburg, G. D., and Soloviev, V. A., 1997, Methane migration within the submarine gas-hydrate stability zone under deep-water conditions: Marine Geology, v. 137, p. 49-57.

Haacke, R. R., Hyndman, R. D., Park, K.-P., Yoo, D.-G., Stoian, I., and Schmidt, U., 2009, Migration and venting of deep gases into the ocean through hydrate-choked chimneys offshore Korea: Geology, v. 37, no. 6, p. 531-534.

Haberer, R. M., Mangelsdorf, K., Dieckmann, V., Fuhrmann, A., Wilkes, H., and Horsfield, B., 2005, Characterization of the organic matter in lignite layers of the Kugmallit Sequence (Oligocene) at the JAPEX/JNOC/GSC et al. Mallike 5L-38 gas hydrate production research well, *in* Dallimore, S. R., and Collett, T. S., ed., Scientific Results from the Mallik 2002 Gas Hydrate Production Research Well Program, Mackenzie Delta, Northwest Territories, Canada, Volume Bulletin 585, Geological Survey of Canada, p. 14.

Haeckel, M., Suess, E., Wallmann, K., and Rickert, D., 2004, Rising methane gas bubbles form massive hydrate layers at the seafloor: Geochimica et Cosmochimica Acta, v. 68, no. 21, p. 4335-4345.

Henninges, J., Schrotter, J., Erbas, K., and Huenges, E., 2005, Temperature field of the Mallik gas hydrate occurrence - implication on phase changes and thermal properties, *in* Dallimore, S. R., and Collett, T. S., eds., Scientific Results from the Mallik 2002 Gas Hydrate Production Research Well Program, Mackenzie Delta, Northwest Territories, Canada, Volume Bulletin 585, Geological Survey of Canada, p. 11.

Hubbert, M. K., 1953, Entrapment of Petroleum under Hydrodynamic Conditions: Bulletin of the American Association of Petroleum Geologists, v. 38, no. 8, p. 1954-2026.

Lake, L. W., 1989, Enhanced oil recovery, Prentice Hall.

Levitus, S., Boyer, T. P., Conkright, M. E., Brien, T. O., Antonov, J., Stephens, C., Stathoplos, L., Johnson, D., and Gelfeld, R., 1998, NOAA Atlas NESDIS 18,World Ocean Database 1998: VOLUME 1: INTRODUCTION: Wash., D.C., U.S. Gov. Printing Office, p. 346pp.

Lide, D. R., 2004, CRC Handbook of Chemistry and Physics, 85th Edition, Taylor & Francis.

Liu, X., 2006, Dynamics of Shallow Marine Gas Hydrate and Free Gas Systems [Doctor of Philosophy: The Pennsylvania State University, 135 p.

Liu, X., and Flemings, P. B., 2007, Dynamic multiphase flow model of hydrate formation in marine sediments: Journal of Geophysical Research, v. 112, no. B3.

Majorowicz, J., Safanda, J., and Osadetz, K., 2012, Inferred gas hydrate and permafrost stability history models linked to climate change in the Beaufort-Mackenzie Basin, Arctic Canada: Clim. Past, v. 8, no. 2, p. 667-682.

Malusis, M. A., Shackelford, C. D., and Olsen, H. W., 2003, Flow and transport through clay membrane barriers: Engineering Geology, v. 70, no. 3–4, p. 235-248.

Mazumdar, A., Dewangan, P., Joäo, H. M., Peketi, A., Khosla, V. R., Kocherla, M., Badesab, F. K., Joshi, R. K., Roxanne, P., Ramamurty, P. B., Karisiddaiah, S. M., Patil, D. J., Dayal, A. M., Ramprasad, T., Hawkesworth, C. J., and Avanzinelli, R., 2009, Evidence of paleo–cold seep activity from the Bay of Bengal, offshore India: Geochemistry, Geophysics, Geosystems, v. 10, no. 6, p. n/a-n/a.

McConnell, D. R., and Kendall, B. A., Images of the base of gas hydrate stability, Northwest Walker Ridge, Gulf of Mexico, *in* Proceedings Offshore Technology Conference, Houston, Texas, 6-9 May 2002 2002.

Meyer, D. W., and Flemings, P. B., 2014, Thermodynamic State of Gas Hydrate in the Krishna-Godavari Basin Inferred From Well Log Analysis, Offshore Technology Conference.

Milkov, A. V., Y.-J. Lee, Borowski, W. S., Torres, M. E., Xu, W., Tomaru, H., Trehu, A. M., Schultheiss, P., Dickens, G. R., and Claypool, G. E., 2004, Co-existence of gas hydrate, free gas, and brine within the regional gas hydrate stability zone at Hydrate Ridge (Oregon margin): Evidence

from prolonged degassing of a pressurized core: Earth and Planetary Science Letters, v. 222, p. 829-843.

Moridis, G. J., 2008, TOUGH+Hydrate v1.0 User's Manual: A Code for the Simulation of System Behavior in Hydrate-Bearing Geologic Media.

NGHP Expedition 01 Scientists, 2007, Sites NGHP-01-10, 12, and 13, *in* Collett, T. S., Reidel, M., Cochran, J., Boswell, R., Presley, J., Kumar, P., Sathe, A., Sethi, A., Lall, M., and the NGHP Expedition 01 Scientists, eds., National Gas Hydrate Program Expedition 01 Initial Reports, Directorate General of Hydrocarbon, Ministry of Petroleum and Natural Gas (India), p. 150.

Orr, F. M., 2007, Theory of gas injection processes, Tie-Line Publications.

Paull, C. K., Dallimore, S., Hughes-Clarke, J., Blasco, S., Lundsten, E., III, W. U., Graves, D., Sherman, A., Conway, K., Melling, H., Vagle, S., and Collett, T., 2011, Tracking the Decomposition of Submarine Permafrost and Gas Hydrate Under the Shelf and Slope of the Beaufort Sea, 7th International Conference on Gas Hydrate, p. 12.

Phrampus, B. J., and Hornbach, M. J., 2012, Recent changes to the Gulf Stream causing widespread gas hydrate destabilization: Nature, v. 490, no. 7421, p. 527-530.

Rachold, V., Bolshiyanov, D. Y., Grigoriev, M. N., Hubberten, H.-W., Junker, R., Kunitsky, V. V., Merker, F., Overduin, P., and Schneider, W., 2007, Nearshore arctic subsea permafrost in transition: Eos, Transactions American Geophysical Union, v. 88, no. 13, p. 149-150.

Reagan, M. T., and Moridis, G. J., 2009, Large-scale simulation of methane hydrate dissociation along the West Spitsbergen Margin: Geophysical Research Letters, v. 36, no. 23, p. L23612.

Rees, E. V. L., Priest, J. A., and Clayton, C. R. I., 2011, The structure of methane gas hydrate bearing sediments from the Krishna–Godavari Basin as seen from Micro-CT scanning: Marine and Petroleum Geology, v. 28, no. 7, p. 1283-1293.

Rehder, G., Brewer, P. W., Peltzer, E. T., and Friederich, G., 2002, Enhanced lifetime of methane bubble streams within the deep ocean: Geophysical Research Letters, v. 29, no. 15, p. 21-21-21-24.

Riedel, M., Collett, T. S., Kumar, P., Sathe, A. V., and Cook, A., 2010, Seismic imaging of a fractured gas hydrate system in the Krishna–Godavari Basin offshore India: Marine and Petroleum Geology, v. 27, no. 7, p. 1476-1493.

Ryu, B.-J., Collett, T. S., Riedel, M., Kim, G. Y., Chun, J.-H., Bahk, J.-J., Lee, J. Y., Kim, J.-H., and Yoo, D.-G., 2013, Scientific results of the Second Gas Hydrate Drilling Expedition in the Ulleung Basin (UBGH2): Marine and Petroleum Geology, v. 47, no. 0, p. 1-20.

Schneider, J., 2011, Compression and Permeability Behavior of Natural Mudstones [Doctor of Philosophy Doctor of Philosophy]: The University of Texas, 321 p.

Skarke, A., Ruppel, C., Kodis, M., Brothers, D., and Lobecker, E., 2014, Widespread methane leakage from the sea floor on the northern US Atlantic margin: Nature Geosci, v. advance online publication.

Sloan, E. D., and Koh, C., 2007, Clathrate Hydrates of Natural Gases, Third Edition, CRC Press.

Smith, A. J., Flemings, P. B., and Fulton, P. M., 2014, Hydrocarbon flux from natural deepwater Gulf of Mexico vents: Earth and Planetary Science Letters, v. 395, no. 0, p. 241-253.

Sun, X., and Mohanty, K. K., 2006, Kinetic simulation of methane hydrate formation and dissociation in porous media: Chemical Engineering Science, v. 61, no. 11, p. 3476-3495.

Taylor, A. E., Dallimore, S. R., Hyndman, R. D., and Wright, F., 2005, Comparing the sensitivity of permafrost and marine gas hydrate to climate warming, Scientific Results from the Mallik 2002 Gas Hydrate Production Research Well Program, Mackenzie Delta, Northwest Territories, Canada, Geological Survey of Canada, Bulletin no. 585, 2005.

Torres, M. E., Kim, J. H., Choi, J. Y., Ryu, B. J., Bahk, J. J., Riedel, M., Collett, T. S., Hong, W. L., and Kastner, M., Occurrence of high salinity fluids associated with massive near-seafloor gas

hydrate deposits, *in* Proceedings 7th International Conference on Gas Hydrates (ICGH 2011), Edinburgh; GB, July 17-21, 2011 2011, p. 1-19.

Torres, M. E., Wallmann, K., Tréhu, A. M., Bohrmann, G., Borowski, W. S., and Tomaru, H., 2004, Gas hydrate growth, methane transport, and chloride enrichment at the southern summit of Hydrate Ridge, Cascadia margin off Oregon: Earth and Planetary Science Letters, v. 226, no. 1–2, p. 225-241.

You, K., Kneafsey, T. J., Flemings, P. B., Polito, P., and Bryant, S. L., 2015, Salinity-buffered methane hydrate formation and dissociation in gas-rich systems: Journal of Geophysical Research: Solid Earth, v. 120, no. 2, p. 643-661.

You, Y., Flemings, P., Mohrig, D., and Germaine, J., 2014, How heterogeneity in the shear dilation of a deposit controls the mechanics of breaching slope failure: Journal of Geophysical Research: Earth Surface, p. n/a-n/a.

Zatsepina, O. Y., and Buffett, B. A., 2003, Nucleation of gas hydrate in marine environments: Geophysical Research Letters, v. 30, no. 9, p. 1451.

5. Appendices

<u>Appendix A: Mass Balance Equation Derivation</u>

This derivation makes the following critical assumptions: A) constant brine density, B) gas and hydrate only exist within the MOC-defined hydrate formation zone (HFZ), and C) gas and hydrate phases are homogenously distributed within the HFZ. We begin with the following set of mass balance equations:

$$\Delta W = \Delta M_W^B + \Delta M_W^H = V_{TOT}\phi\rho_W \cdot \Delta S_W + \frac{V_{TOT}\phi\rho_H N M_W}{M_H} \cdot \Delta S_H \qquad \text{Eq 55}$$

$$\Delta M = M_M^G + M_M^H = V_{TOT}\phi\rho_G \cdot \Delta S_G + \frac{V_{TOT}\phi\rho_H M_G}{M_H} \cdot \Delta S_H \qquad \text{Eq 56}$$

$$0 = \Delta S_G + \Delta S_H + \Delta S_W \qquad \text{Eq 57}$$

Where ΔM_W^B, ΔM_W^H, ΔM_M^G, and ΔM_M^H are the mass of water in the brine and hydrate phase and mass of methane in the gas and hydrate phase, respectively. These terms are expanded to show their relation to the phase saturations, such that we can solve for those instead of the masses. For simplicity, we reduce Eq.55 and 56 into Eq.58 and 59:

$$\Delta W = A \cdot \Delta S_W + B \cdot \Delta S_H \qquad \text{Eq 58}$$

$$\Delta M = C \cdot \Delta S_G + D \cdot \Delta S_H \qquad \text{Eq 59}$$

Where,

$$A = V_{TOT}\phi\rho_w$$

$$B = \frac{V_{TOT}\phi\rho_H N M_W}{M_H}$$

$$C = V_{TOT}\phi\rho_G$$

$$D = \frac{V_{TOT}\phi\rho_H M_G}{M_H}$$

Eliminate ΔS_H from Eq.55 and Eq.56 by multiplying Eq.58 by D and Eq.59 by B and then subtracting the two:

$$AD\Delta S_W - BC\Delta S_G = D\Delta W - B\Delta M \qquad \text{Eq 60}$$

Eliminate ΔS_H from Eq.59 and Eq.57 by multiplying Eq.57 by D and then subtracting the two:

$$(C - D)\Delta S_G - D\Delta S_W = \Delta M \qquad \text{Eq 61}$$

Eliminate ΔS_W from Eq.60 and Eq.61 by multiplying Eq. 61 by A and then subtracting the two:

$$[A(C - D) - BC]\Delta S_G = D\Delta W + (A - B)\Delta M \qquad \text{Eq 62}$$

Solve for ΔS_G:

$$\Delta S_G = \frac{D\Delta W + (A-B)\Delta M}{[A(C-D)-BC]} = E \qquad \text{Eq 63}$$

Substitute Eq.63 back into Eq.64 and solve for ΔS_W:

$$\Delta S_W = \frac{(C-D)E + \Delta M}{D} = F \qquad \text{Eq 64}$$

Substitute Eq.63 and Eq. 64 back into Eq.3 and solve for ΔS_H:

$$\Delta S_W = -(E + F) \qquad \text{Eq 65}$$

Expand Eqs.63 – 65 by substituting, A – F back into them:

$$\Delta S_G = \frac{\left[\left(\frac{V_{TOT}\phi\rho_H M_G}{M_H}\cdot\Delta W\right)+\left(\left(V_{TOT}\phi\rho_W - \frac{V_{TOT}\phi\rho_H N M_W}{M_H}\right)\cdot\Delta M\right)\right]}{\left[\left(V_{TOT}\phi\rho_W\cdot\left(V_{TOT}\phi\rho_G - \frac{V_{TOT}\phi\rho_H M_G}{M_H}\right)\right)-\left(\frac{V_{TOT}\phi\rho_H N M_W}{M_H}\cdot V_{TOT}\phi\rho_G\right)\right]} \qquad \text{Eq 66}$$

$$\Delta S_W = \frac{\left[\left(\Delta S_G\cdot\left(V_{TOT}\phi\rho_G - \frac{V_{TOT}\phi\rho_H M_G}{M_H}\right)\right)-\Delta M\right]}{\frac{V_{TOT}\phi\rho_H M_G}{M_H}} \qquad \text{Eq 67}$$

$$\Delta S_H = -(\Delta S_G + \Delta S_W) \qquad \text{Eq 68}$$

Appendix B: Single Energy CT Saturation Equation Derivation

This derivation makes the following critical assumptions: A) the brine density does not change, B) gas density is negligible, C) the solid grains in the sample do not move, and D) hydrate only forms within the hydrate formation zone (HFZ) determined from the CT scan images. With these assumptions we begin with the following set of equations:

$$\rho_b^{dry} = \left((1-\phi)\cdot\rho_s\right)+(\phi\cdot\rho_G) \qquad \text{Eq 69}$$

$$\rho_b^{wet} = \left((1-\phi)\cdot\rho_s\right)+(\phi\cdot\rho_W) \qquad \text{Eq 70}$$

$$\rho_b^{exp} = \left((1-\phi)\cdot\rho_s\right)+(S_W\cdot\phi\cdot\rho_W)+(S_G\cdot\phi\cdot\rho_G)+(S_H\cdot\phi\cdot\rho_H) \qquad \text{Eq 71}$$

$$S_W + S_H + S_G = 1 \qquad \text{Eq 72}$$

Equations 69 – 71 define the bulk densities of the dry and saturated samples and during the experiment as a function of the saturations and densities of each individual phase present and the sample porosity. Where ρ_b^{dry}, ρ_b^{wet}, and ρ_b^{exp} are the dry, wet, and experimental bulk densities, respectively, ϕ is the porosity, S_W, S_G, and S_H and ρ_W, ρ_G, and ρ_H are the saturations and densities of water, gas, and hydrate, respectively. Equation 4 defines the fractional saturation of each phase in the sample.

Since the dry and saturated bulk density are considered the density endpoints of the system, the total saturation can be defined as the fractional change of the density between the endpoints (Eq. 73):

$$S_T = \left(\frac{\rho_b^{exp}-\rho_b^{dry}}{\rho_b^{wet}-\rho_b^{dry}}\right) \qquad \text{Eq 73}$$

This total saturation is equivalent to the water saturation if the system consisted of only two phases, gas and water. We incorporate the effect of hydrate as a third phase on the density and total saturation by substituting equations 69 – 71 into Equation 73:

$$S_T = \left(\frac{\left((1-\phi)\cdot\rho_s\right)+(S_W\cdot\phi\cdot\rho_W)+(S_G\cdot\phi\cdot\rho_G)+(S_H\cdot\phi\cdot\rho_H)-\left((1-\phi)\cdot\rho_s\right)-(\phi\cdot\rho_G)}{\left((1-\phi)\cdot\rho_s\right)+(\phi\cdot\rho_W)-\left((1-\phi)\cdot\rho_s\right)-(\phi\cdot\rho_G)}\right) \qquad \text{Eq 74}$$

As a result of the critical assumptions listed above, Equation 74 is further simplified (Eq. 75):

$$S_T = \left(\frac{(S_W \cdot \phi \cdot \rho_W) + (S_H \cdot \phi \cdot \rho_H)}{(\phi \cdot \rho_W)} \right) = \frac{M_W + M_H}{M_{Wi}} \qquad \text{Eq 75}$$

Where M_W, M_H, and M_{Wi} are the masses of water, hydrate, and initial water, respectively. Eq.75 can be rearranged in the following ways (Eqs. 76 and 77):

$$S_T = \frac{M_W}{M_{Wi}} \cdot \left(1 + \frac{M_H}{M_W} \right) \qquad \text{Eq 76}$$

$$S_T = \frac{M_H}{M_{Wi}} \cdot \left(1 + \frac{M_W}{M_H} \right) \qquad \text{Eq 77}$$

From here, we need to determine the mass of water and hydrate in the system at any particular time. To do this we look to the following mass balance of water and hydrate in the sample:

$$M_W = M_{Wi} - X M_{Wi} - Y M_{Wi} = (1 - X - Y) M_{Wi} \qquad \text{Eq 78}$$

$$M_H = X f M_{Wi} \qquad \text{Eq 79}$$

Equation 78 defines the mass of water remaining in the sample as a function of the initial water mass minus the fraction of initial water converted to hydrate (X) and the fraction of water removed from the sample (Y). Equation 79 defines the mass of hydrate in the sample as a function of initial water in the sample, the fraction of water converted into hydrate, and the mass ratio of hydrate to water in hydrate (f), equal to 1.15. Where X and Y are calculated with equations 80 and 81:

$$X = (\Delta V_m - \Delta V_w) \cdot \frac{M_w \cdot N \cdot \rho_H}{V_{pore} \cdot \rho_w \cdot (1 - C) \cdot M_H} \cdot \frac{L_{HFZ}}{L} \qquad \text{Eq 80}$$

$$Y = \frac{\Delta V_w \cdot \rho_w}{V_{pore} \cdot \rho_w} \cdot \frac{L_{HFZ}}{L} \qquad \text{Eq 81}$$

Where ΔV_m and ΔV_w are the changes in volume in the methane and brine pumps, respectively, V_{pore} is the pore volume ($V_{pore} = V_{TOT} \cdot \phi$), C is the initial salinity in weight percent, L is the total sample length, and L_{HFZ} is the length of the HFZ. X and Y are corrected for the location of the hydrate formation front using the ratio between L and L_{HFZ}. When processing CT slices beyond the HFZ, X and Y are both set equal to zero. Dividing Equation 78 by Equation 79 and Equation 79 by Equation 78 yields:

$$\frac{M_W}{M_H} = \frac{(1 - X - Y)}{X f} \qquad \text{Eq 82}$$

$$\frac{M_H}{M_W} = \frac{X f}{(1 - X - Y)} \qquad \text{Eq 83}$$

We define the saturations of water and hydrate as function of the volume of water and hydrate divided by the total volume, respectively:

$$S_W = \frac{V_W}{V_{TOT}} = \frac{M_W / \rho_W}{M_{Wi} / \rho_W} = \frac{M_W}{M_{Wi}} \cdot \frac{\rho_W}{\rho_W} \qquad \text{Eq 84}$$

$$S_H = \frac{V_H}{V_{TOT}} = \frac{M_H / \rho_H}{M_{Wi} / \rho_W} = \frac{M_H}{M_{Wi}} \cdot \frac{\rho_W}{\rho_H} \qquad \text{Eq 85}$$

Equations 84 and 85 can be simplified and rearranged into equations 86 and 87:

$$\frac{M_W}{M_{Wi}} \cdot \frac{\rho_W}{\rho_W} = S_W \qquad \text{Eq 86}$$

$$\frac{M_H}{M_{Wi}} = S_H \cdot \frac{\rho_H}{\rho_W} \qquad \text{Eq 87}$$

Substituting equations 82 and 86 in Equation 76 and equations 84 and 87 into Equation 77 yields equations 88 and 89:

$$S_T = S_W \cdot \left(1 + \frac{Xf}{(1-X-Y)} \right) \qquad \text{Eq 88}$$

$$S_T = S_H \cdot \left(1 + \frac{(1-X-Y)}{Xf} \right) \cdot \frac{\rho_W}{\rho_H} \qquad \text{Eq 89}$$

From here, we solve equations 58, 88 and 89 for the gas, water, and hydrate saturations, respectively, to produce equations 90 – 92:

$$S_w = \frac{S_T}{\left(1 + \frac{Xf}{(1-X-Y)} \right)} \qquad \text{Eq 90}$$

$$S_H = \left[\frac{S_T}{\left(1 + \frac{(1-X-Y)}{Xf} \right)} \right] \cdot \left[\frac{\rho_w}{\rho_h} \right] \qquad \text{Eq 91}$$

$$S_G = 1 - S_w - S_H \qquad \text{Eq 92}$$

National Energy Technology Laboratory

626 Cochrans Mill Road
P.O. Box 10940
Pittsburgh, PA 15236-0940

3610 Collins Ferry Road
P.O. Box 880
Morgantown, WV 26507-0880

13131 Dairy Ashford Road, Suite 225
Sugar Land, TX 77478

1450 Queen Avenue SW
Albany, OR 97321-2198

Arctic Energy Office
420 L Street, Suite 305
Anchorage, AK 99501

Visit the NETL website at:
www.netl.doe.gov

Customer Service Line:
1-800-553-7681